FE-2248-19
Distribution Categories UC-90g and 93

DEVELOPMENT, TESTING AND EVALUATION OF MHD MATERIALS AND COMPONENT DESIGNS

Quarterly Report for the Period

January - March 31, 1978

John W. Sadler
Jeff Bein
David L. Black
Raymond Calvo
Laurence H. Cadoff*
James A. Dilmore*
Gary E. Driesen
Alfred G. Eggers
Edsel W. Frantti
Edgar L. Kochka
Jack A. Kuszyk
Joseph Lempert*
Barry R. Rossing*
Stephen J. Schneider*
Abner B. Turner

* Westinghouse Research & Development Center

WESTINGHOUSE ELECTRIC CORPORATION
Advanced Energy Systems Division
P. O. Box 10864
Pittsburgh, PA 15236

MAY 1978

PREPARED FOR THE
UNITED STATES DEPARTMENT OF ENERGY

Under Contract No. EX-76-C-01-2248

APPROVED:

J. W. Sadler, Project Manager
Advanced Energy Systems Division

TABLE OF CONTENTS

TABLE OF CONTENTS (Continued)

LIST OF FIGURES

LIST OF FIGURES (Continued)

LIST OF FIGURES (Continued)

LIST OF FIGURES (Continued)

LIST OF TABLES

I. ABSTRACT

Efforts during the January through March 1978 quarter were directed towards the evaluation of MHD electrodes for both clean and coal fired environments.

Electrochemical screening tests in simulated liquid slags have continued, and provide additional information on the chemistry, mechanisms, and kinetics of electrode/slag reactions.

U-02 Proof Test 3 (WESTF Test 40) was completed in early January. A post-test evaluation was made and the results compared with those of the previous 2 proof tests. Post-test materials characterization, including efforts at National Bureau of Standards (NBS) and Battelle Pacific Northwest Laboratories (BNW), was completed and provided the basis for the selection of $LaCrO_3$ - based electrode materials with compliant Ni-mesh attachments for the U-02 Phase III electrode walls. Materials development and detail design activities in support of the U-02 Phase III module continued, and U-02 Phase III electrode sub-assemblies were prepared.

II. OBJECTIVE AND SCOPE OF WORK

In continuation of the program to develop MHD power generation to commercial feasibility, Westinghouse is conducting a 36-month program to test and evaluate materials and component designs in both laboratory scale apparatus and in an integrated MHD system facility. While primary emphasis has been given to "hot generator wall" concepts under slagging conditions, the program includes efforts on cold wall designs. The program provides a link between the basic and supportive materials development and testing and the applied testing in a facility that offers an adverse MHD environment for extended periods of time. The program carries forth the engineering development of selected MHD component(s), e.g., electrode and insulating wall systems, through design, materials fabrication, initial screening tests, construction and finally to an MHD system test. The entire sequence is reiterative; i.e., each stage will involve an optimization of both design and materials.

These objectives are being pursued in accordance with a statement of work which is consistent with the National Plan for MHD development formulated by DOE.

The major elements of the program are presented in a Work Breakdown Structure which is presented in Table 1. The Level I effort is the MHD generator Electrode System Development Contract and Level II consists of the following six major tasks:

WBS 1.1 ELECTRODE SYSTEM ENGINEERING
WBS 1.2 TEST ASSEMBLY FABRICATION
WBS 1.3 WESTINGHOUSE ELECTRODE SYSTEM TEST FACILITY (WESTF)
WBS 1.4 WESTINGHOUSE MHD TEST FACILITY (WMTF)
WBS 1.5 COOPERATIVE US/USSR MHD PROGRAM
WBS 1.6 PROJECT MANAGEMENT AND DOCUMENTATION

WBS 1.1 - ELECTRODE SYSTEM ENGINEERING

The objective of this task is to provide centralized engineering for the MHD electrode development effort. This comprehensive effort incorporates all aspects

TABLE 1. WORK BREAKDOWN STRUCTURE

WBS 1.0 - MHD GENERATOR ELECTRODE SYSTEM DEVELOPMENT PROGRAM

- WBS 1.1 - ELECTRODE SYSTEM ENGINEERING
  - WBS 1.1.1 - Design and Analysis
    - WBS 1.1.1.1 - Development Requirements
    - WBS 1.1.1.2 - Electrode and Experiment Design
    - WBS 1.1.1.3 - Experiment Analysis
  - WBS 1.1.2 - Materials Evaluation
    - WBS 1.1.2.1 - Electrode and Insulator Materials
    - WBS 1.1.2.2 - Electrode/Insulator Systems
    - WBS 1.1.2.3 - MHD Materials Data Log
- WBS 1.2 - TEST ASSEMBLY FABRICATION
  - WBS 1.2.1 - WESTF Test Assemblies
    - WBS 1.2.1.1 - Material Procurement
    - WBS 1.2.1.2 - Fabrication and Assembly
  - WBS 1.2.2 - WMTF Test Assemblies
    - WBS 1.2.2.1 - Material Procurement
    - WBS 1.2.2.2 - Fabrication and Assembly
- WBS 1.3 - WESTINGHOUSE ELECTRODE SYSTEMS TEST FACILITY (WESTF)
  - WBS 1.3.1 - Facility Design and Modification
    - WBS 1.3.1.1 - Diagnostic Systems
    - WBS 1.3.1.2 - Support Systems
  - WBS 1.3.2 - Test Operations
    - WBS 1.3.2.1 - Pre-test Activities
    - WBS 1.3.2.2 - Test Operations
  - WBS 1.3.3 - Facility Deactivation
- WBS 1.4 - WESTINGHOUSE MHD TEST FACILITY (WMTF)
  - WBS 1.4.1 - Facility Design
    - WBS 1.4.1.1 - Combustor/Mixer
    - WBS 1.4.1.2 - Discharge Piping and Preheater
    - WBS 1.4.1.3 - High Pressure Air System
    - WBS 1.4.1.4 - Control Room & DAS
    - WBS 1.4.1.5 - Support Systems
  - WBS 1.4.2- Facility Modification
    - WBS 1.4.2.1 - Combustor/Mixer
    - WBS 1.4.2.2 - Discharge Piping and Preheater
    - WBS 1.4.2.3 - High Pressure Air System
    - WBS 1.4.2.4 - Control Room and DAS
    - WBS 1.4.2.5 - Support Systems
  - WBS 1.4.3 - Test Operations
    - WBS 1.4.3.1 - Facility Checkout
    - WBS 1.4.3.2 - Pre-Test Activities
    - WBS 1.4.3.3 - Test Operations
  - WBS 1.4.4 - Facility Deactivation
- WBS 1.5 - COOPERATIVE US/USSR MHD PROGRAM
  - WBS 1.5.1 - US/USSR Liaison
  - WBS 1.5.2 - U-02 Phase III Module
  - WBS 1.5.3 - USSR Testing
- WBS 1.6 - PROJECT MANAGEMENT AND DOCUMENTATION

of engineering development including: materials evaluation, design studies (including detailed analytical efforts), and experiment design and analysis.

Specifically, this task will:

- Identify and evaluate electrode systems engineering requirements and designs.
- Identify development needs to support design activities, specify test conditions and requirements, and integrate the results of engineering tests into the design activities.
- Provide for the coordinated engineering of Test Assemblies.

This task relates to Task 1.5 (Cooperative US/USSR MHD Program) in a manner to assure that the results of the US/USSR program are factored into coal firing electrode system design and development, and to the maximum extent possible will influence that effort to supplement or compliment development on this project.

Electrode system engineering effort is directed towards quantitative determination of specific design and material influence on electrode system performance and durability. There exists a close inter-relationship between thermal, electrical and geometric design considerations and material requirements and capabilities. This task provides the close engineering design and test discipline necessary to effect successful electrode system development.

WBS 1.2 - TEST ASSEMBLY FABRICATION

This task provides for fabrication of Test Assemblies for WESTF and WMTF. The Test Assembly consists of the following:

- Outer Casings (including water cooled plates)
- Electrode/Insulator Systems (including current leadout)
- Insulating Walls
- Instrumentation and Miscellaneous Hardware

Material procurement, processing, fabrication and assembly, when appropriate, are included.

WBS 1.3 - WESTINGHOUSE ELECTRODE SYSTEMS TEST FACILITY (WESTF)

Dynamic testing of electrode and insulator materials and electrode systems will be accomplished in WESTF. The facility will simulate the "reference" combustion products associated with development of MHD generators and currently provides the capability for testing under simulated MHD stress conditions in an automated mode for extended durations. Operating parameters are summarized in Table 2, which reflect those conditions necessary to support generator development activities. The facility is flexible in that it can be operated under each of the generator operating modes - cold to hot wall, clean or slagging.

This task provides for: facility design, procurement, installation and checkout of facility hardware, and WESTF test operations.

WBS 1.4 - WESTINGHOUSE MHD TEST FACILITY (WMTF)

The Westinghouse MHD Test Facility (WMTF) is located at the Westinghouse Energy Systems Operation Site, Waltz Mill, Pennsylvania. The primary objective of the WMTF is to support through test the engineering development of open cycle MHD generators, including electrode and insulating wall designs and materials, under full MHD operating conditions (see Table 2).

WMTF operations were suspended at the end of CY'76 at which time a number of facility modifications had been initiated to extend facility capability. At the request of DOE this HOLD has been maintained.

WBS 1.5 - COOPERATIVE US/USSR MHD PROGRAM

This task provides technical support to the activities of the cooperative US-USSR program.

Specifically this involves 1) USSR Testing in Westinghouse Facilities, 2) U-25 Module Testing in Westinghouse Facilities and 3) Materials Testing in U-02, Phase I and Phase II. Each of these activities are defined by DOE appointed committees.

TABLE 2

MHD FACILITY CHARACTERISTICS

CHARACTERISTIC	WESTINGHOUSE MHD TEST FACILITY (WMFT)	WESTINGHOUSE ELECTRODE SYSTEMS TEST FACILITY (WESTF)
Mass Flow	3 lb/sec design	0.5 lb/sec
Combustion Temperature	To 2850^{o}K	To 2850^{o}K
Combustor Pressure	2.6 - 3.0 atmospheres normal 6 atm peak	2-3 atmospheres normal 5 atm peak
Channel Velocity	Subsonic or Supersonic (Future)	Subsonic, 500 to 800 m/sec
Seeding	K_2CO_3 or K_2SO_4 dry with ash or char additions	K_2CO_3 or K_2SO_4 wet with ash or char additions
B Field	3 Tesla flat over one meter	None (Future)
Magnet Opening	13.5 x 25.4 x 111.76 cm	N.A.
Fuel	Toluene	Toluene
Oxidant Oxygen	Oxygen enriched preheated air	Oxygen enriched preheated air
Data Collection	240 channels	60 channels
Test Duration	Up to 100 hours or greater	Up to 100 hours
Test Frequency	1 per month	2 per month
Channel Configuration	16 to 48 electrode pairs	12 electrode pairs 1" x 2" flow cross section
Startup Ramp, Minimum	~10^{o}K/min	~25^{o}K/min
Load Bank	Lamps	N.A.

This effort includes general liaison relative to the joint US/USSR committees active in the areas of materials and generators and monitoring USSR testing programs in US facilities, non-Westinghouse. This does not include provisions for any development or hardware effort.

Complete the design, fabrication, assembly, and delivery of a U-02 Phase III test module to the U-02 facility in Moscow. Participate as directed by the DOE Program Manager in test operations and post-test analyses (to be performed by the National Bureau of Standards). Conduct a total of three tests of up to 20 hours on candidate electrode designs as approved by the DOE Project Manager as proof testing prior to final module selection. (Note: The U-02 program agreements are set forth in Meeting Record 08.0208.03, dated February 8, 1977, of the Joint US-USSR MHD Materials Working Group.)

WBS 1.6 - PROJECT MANAGEMENT AND DOCUMENTATION

This centralized management task has been established to provide the focal point for directing the activities which comprise the full project effort. The coordination of the preparation of required contact documentation will also be completed. This documentation includes:

- Periodic Status Report
- Quarterly Technical Progress Reports
- Topical Reports
- Final Report

Preparation of revisions to this Project Management Summary Baseline Report, as may be required by program accomplishments or subsequent contract redirections, will be completed.

III. SUMMARY OF PROGRESS TO DATE

Figure 1 summarizes the overall program schedule and status. During the January to March 1978 quarter primary emphasis was directed toward the UO-2 Phase III Electrode Walls, including completion and evaluation of the U-02 proof testing activities and the design, fabrication, and characterization of U-02 electrode wall materials. These activities are all reported under WBS 1.5 - Cooperative US/USSR MHD Program. Complete detailed results of the U-02 proof test series will be reported in a Topical Report. Another Topical Report will be issued to cover the detailed design, fabrication, and testing of the US electrode walls in the USSR U-02 facility.

1.0 WBS 1.1 - ELECTRODE SYSTEM ENGINEERING

Laboratory electrochemical corrosion tests have continued in liquid synthetic slags. Recent tests have revealed a strong relationship between the iron content of the slag and electrode corrosion mechanisms.

A new program has been initiated to develop improved anodes for cold channel MHD application. The initial emphasis is on understanding the electrochemical/thermal phenomena associated with arc-related anode erosion. Work is underway to determine the feasibility of using simple laboratory test set-ups to rate the erosion resistance of metal electrodes in the same way as determined from previous arc erosion MHD channel tests. Subsequent and more sophisticated testing will provide engineering data necessary to support the design of cold wall anodes for testing in CDIF.

2.0 WBS 1.2 - TEST ASSEMBLY FABRICATION

No significant activity this quarter except as reported under WBS 1.5.

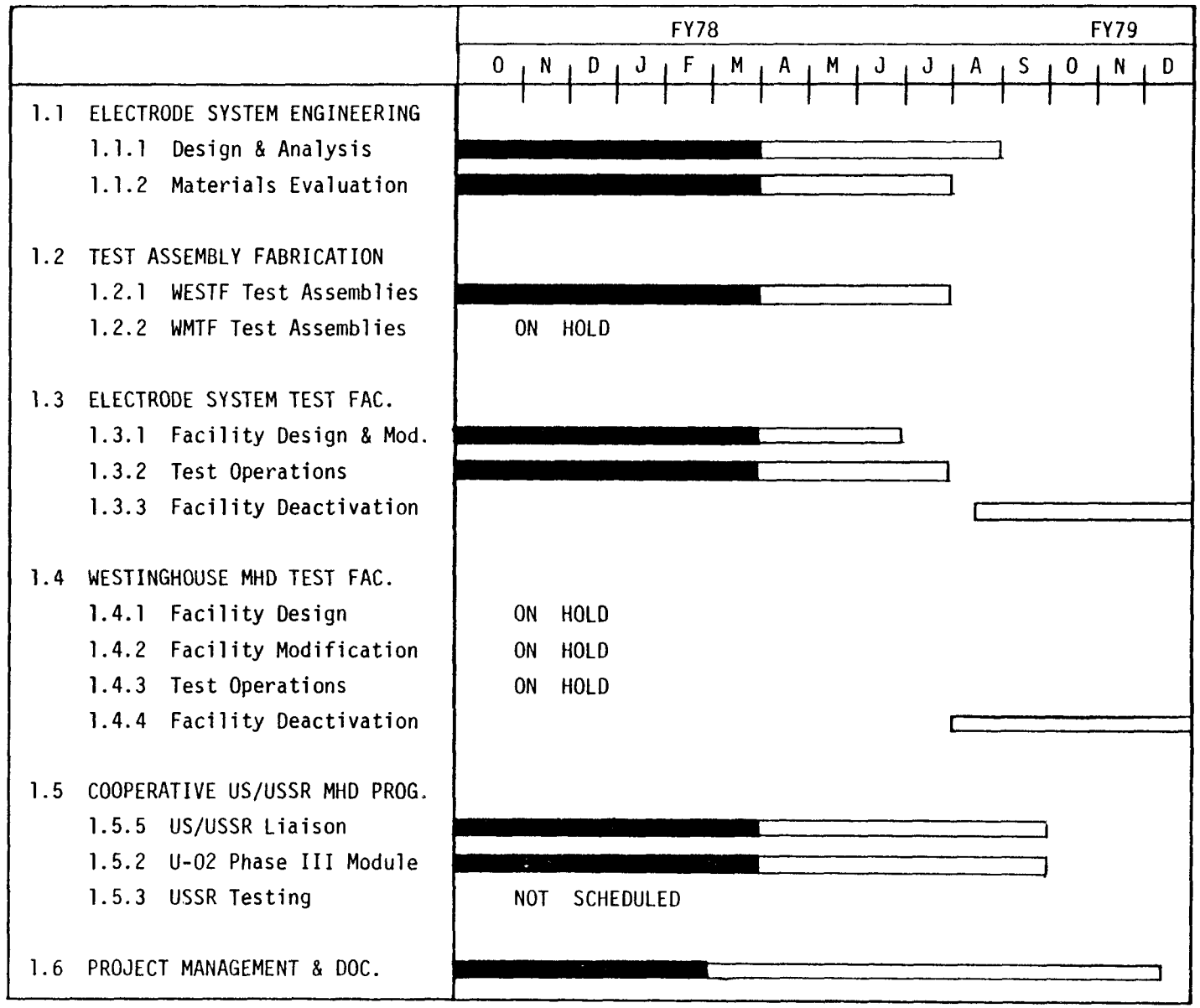

Figure 1. Program Schedule and Status

3.0 WBS 1.3 - WESTINGHOUSE ELECTRODE SYSTEM TEST FACILITY (WESTF)

During this quarter the last of three U-02 Phase III Proof Tests (WESTF Test 39) was run, and the facility was made ready for operation in the slagging mode. Test system components were rebricked, a new nozzle designed, and a Venturi scrubber system installed.

Rearrangement and expansion of the control room began, including installation of additional power supplies to increase the loading of the electrode system as well as provide a simulated axial Hall voltage. Mini-computer hardware was also installed, but operational "de-bugging" is deferred until US/USSR testing of the UO-2 Phase III Module is completed.

4.0 WBS 1.4 - WESTINGHOUSE MHD FACILITY (WMTF)

No effort undertaken this quarter; all activities maintained on HOLD.

5.0 WBS 1.5 - COOPERATIVE US/USSR MHD PROGRAM

In support of the U-02 Phase III Module, Proof Test 3 (WESTF Test 39), the third in a series of three tests, was completed on 1/5/78. This test included $LaCrO_3$ materials and a MAFF-31 electrode system and ran for 20+ hours with surface temperatures of 1600 to 1785^{o}C and current densities of 1.0 A/cm^{2}. A detailed evaluation of the results of all three proof tests provided the basis for the selection of materials and design of electrode systems for U-02 Phase III.

The U-02 Phase III module will consist of lanthanum chromite based electrodes brazed to a compliant nickel mesh and have magnesia and spinel interelectrode insulators. Detailed thermal design activities, electrode material and system development, and materials characterization were performed in support of the U-02 Phase III effort. Also, electrode and insulator materials were fabricated and electrode sub-assemblies completed for the final assembly of the U-02 Phase III module.

6.0 WBS 1.6 - PROJECT MANAGEMENT AND DOCUMENTATION

Required project documentation was issued including the following:

- Work Plan - Proof Test 3
- Express Report - Proof Test 3
- Test Plan - Preliminary U-02 Plan Submitted to USSR
- Monthly Project Management Summary Report - December, January, February
- Quarterly Report - July 1 - September 30, 1977, October 1 - December 31, 1977

IV. DETAILED DESCRIPTION OF TECHNICAL PROGRESS

1.0 WBS 1.1 - ELECTRODE SYSTEM ENGINEERING

With the exception of laboratory testing in the area of electrochemical corrosion, primary engineering activities were associated with the development, design, and component fabrication for the U-02 Phase III Module (Section 5.2).

1.1 WBS 1.1.1 - Design and Analysis

No significant activity was undertaken this quarter (see Section 5.2 for equivalent activity in support of the U-02 Phase III Module).

1.2 WBS 1.1.2 - Materials Evaluation

1.2.1 Electrochemical Corrosion

Laboratory scale electrochemical testing of potential electrode materials in simulated slags has revealed the importance of the iron content of the slags to corrosion mechanisms and operating characteristics of the MHD channel (References 1 and 2). The major electrochemical reaction involves the reduction of ferrous ions in the slag at the cathode to metallic iron, followed by, in many cases, the interaction of iron with the cathode material, (i.e., $LaCrO_3 + Fe \longrightarrow FeCr_2O_4$). To further explore the role of the iron content on corrosion, two electrochemical tests (discussed in Reference 1) were run with $LaCrO_3$ and $3MgAl_2O_4 \cdot 1Fe_3O_4$ electrodes, respectively, in a synthetic Western slag formulated to contain no iron at all and having the composition of 34 w/o SiO_2, 23 w/o Al_2O_3, 29 w/o CaO, 10 w/o MgO, 2 w/o TiO_2, 1.6 w/o Na_2O and 1.1 w/o K_2O.

The test conditions and results are summarized in Table 3. Several major differences were observed using the iron-free slag compared to earlier work with an Eastern Illinois #6 type slag (Reference 1). The new slag was considerably more electrically resistive, was more corrosive to anodes and

TABLE 3

SUMMARY OF ELECTROCHEMICAL CORROSION TESTS IN IRON-FREE WESTERN SLAG*

ELECTRODE MATERIAL	$LaCrO_3$	$3MgAl_2O_4 \cdot 1Fe_3O_4$
Test I.D.	113	111
Temperature, ^oC	1390	1400
Duration, Min.	31	45
Electrode Separation, cm	0.32	0.32
Current Density, Amp/cm^2	1.17	1.69
Voltage Drop Across Slag, Calculated		
Start	24	19
End	29	26
Corrosion, ΔW, Mg/Coulomb		
Cathode, ΔW_c	369	180
Anode, ΔW_a	190	74
$\Delta W_x/\Delta W_a$	1.9	2.4
Test Cell	D1	D1

*See Reference 1 for experimental details and materials characterization.

cathodes, and was more readily polarized than the eastern slag. Slag electrolysis was manifested by the evolution of O_2 gas at the anode and by cyclic voltage fluctuations amounting to about $\pm$ 10% of the voltage across the cell. No elemental cathodic phase resulting from slag electrolysis was found. However, the presence of fine bubbles in the slag near the cathode suggests that such a phase had formed but reoxidized between the time the current was shut off and the time the sample cooled to a temperature less than 1000°C (about 0.5 minutes). For example, if elemental calcium was discharged at the cathode during electrolysis, the partial pressure of oxygen at 1400°C would have had to be $<10^{-24}$ atom. Since such a highly reducing atmosphere would have been impossible to maintain once the flow of current was terminated, it is probable that the calcium would reoxidize.

A review of our findings on corrosion mechanisms for electrochemical tests #113 and #111 are summarized below:

$LaCrO_3$ (Test #113)

The dominant corrosion mechanism at the cathode involves decomposition of the perovskite phase into free Cr metal and the dissolution of lanthanum into the slag. Complex La (Ca, Al, Mg) silicates, LaCa aluminate phases, Cr depleted fluxed $LaCrO_3$ grains and free Cr metal are all dispersed in a glassy slag phase at the slag/cathode interface. Deeper into cathode ($\approx$0.25mm from the interface), free Cr metal and La_2O_3 phases are present at grain boundaries and pore surfaces indicating that P_{O2} at this location during the test was $\approx 10^{-15}$ atm. Figure 2(a) shows the microstructure of the $LaCrO_3$ cathode with the fluxed surface layer and the underlying decompsed $LaCrO_3$.

The anode corrodes by the preferential dissolution of La into the slag and the formation of complex Cr rich spinel phases (containing some Mg, Al and Ca) at the slag interface which in turn is readily erroded off by the action of O_2 gas bubbles. Figure 2(b) shows the microstructure of the $LaCrO_3$ anode.

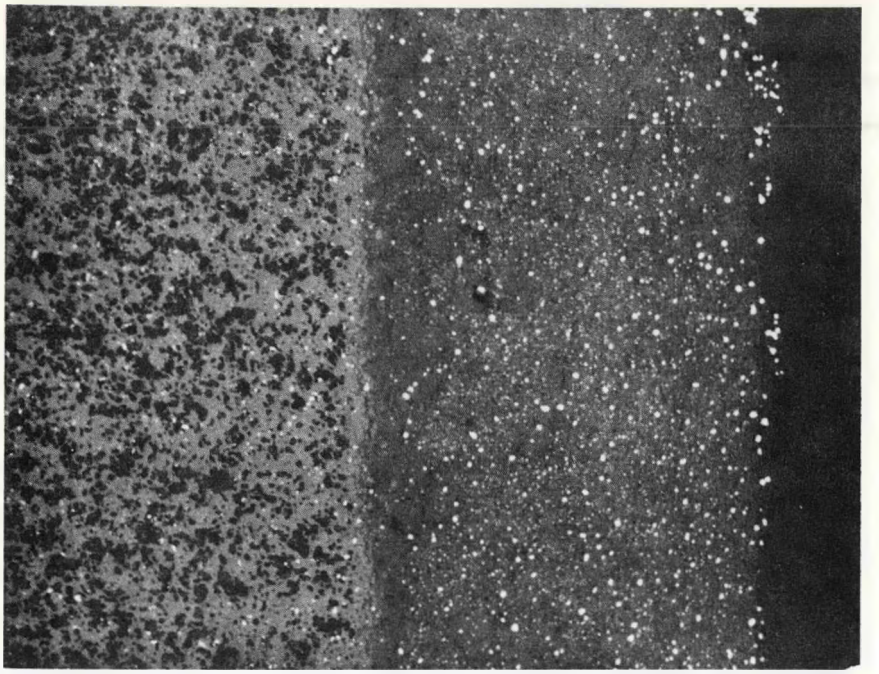

2 (a)

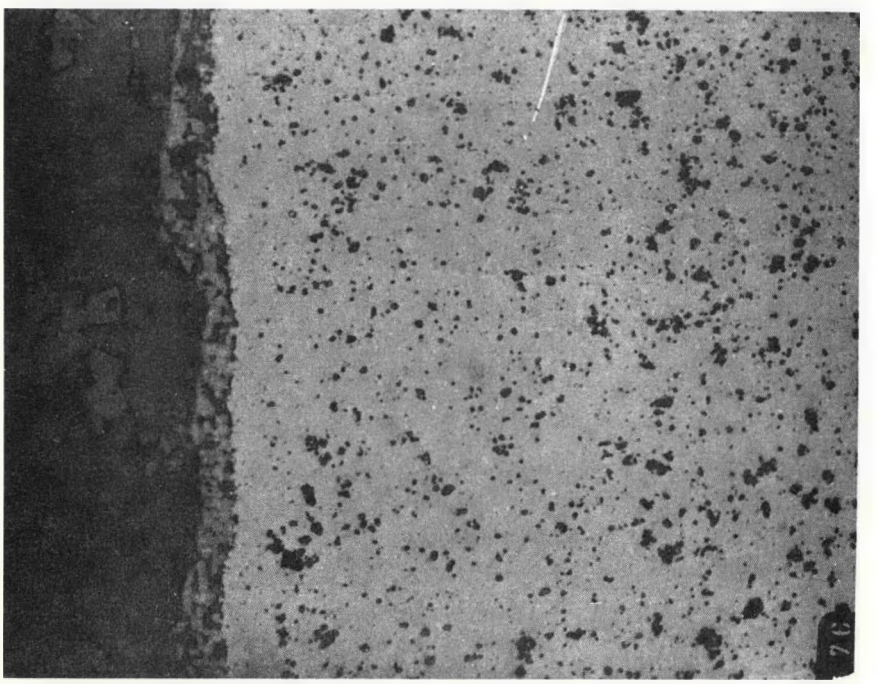

2 (b)

Figure 2 (a) Photomicrograph of slag (far right)/$LaCrO_3$ Cathode Interface-Test 113. Note complex slag intruded surface reaction layer followed by decomposed $LaCrO_3$ matrix phase. White particles are Cr metal. (320X)
(b) Photomicrograph of slag (far left)/$LaCrO_3$ Anode Interface-Test 113. Surface scale is complex Cr rich spinel phase. (320X)

$3MgAl_2O_4 \cdot 1Fe_3O_4$ (Test #111)

At the slag interface and up to a depth of ≈1.2mm from the interface, the catho. is slag intruded and has decomposed to form free metallic iron and a $MgAl_2O_4$ phase containing a small amount of iron in solid solution. The slag that penetrates the grain boundaries and pores in this region is a very calcium rich silicate with small amounts of Al and Mg. From a depth of ≈1.2mm into the cathode to 2.0mm, the matrix has decomposed into FeO and iron depleted $3MgAl_2O_4 \cdot 1Fe_3O_4$. Figure 3 illustrates the morphologies of these regions of the cathode.

Surface erosion by oxygen gas is the dominant corrosion mechanism at the anode. This is accompanied by some dissolution of Fe from the matrix into the slag and the formation of an iron depleted $MgAl_2O_4$ spinel layer on the surface as shown in Figure 4.

1.2.2 Anode Arc Erosion

One of the major problem areas in the design of MHD channels relates to the nature of the electrical contact between the electrodes and the high temperature plasma. The anode electrodes in cold channels are particularly susceptible to the erosive damage caused by arcs.

With the objective of developing longer lived anode electrodes an experimental program has been formulated to permit obtaining a better understanding of the electrochemical/thermal phenomena associated with anode erosion, assessing the erosion rates connnected with different materials and electrode configurations, and analyzing in detail the formation of new alloys and the restructuring of materials under test.

The program recommended to achieve the above objective includes:

A) Simulating the MHD anode arc by drawing an arc under controlled conditions for extended periods of time against a series of experimental anodes in the presence of slag and seed, and evaluating the electrochemical thermal/reactions.

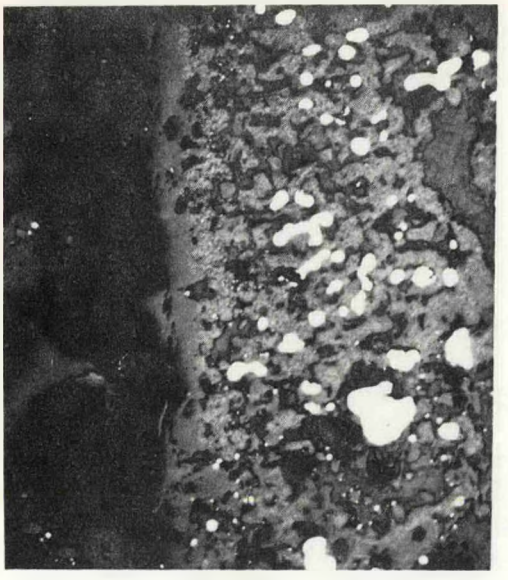

3 (a)

3 (b)

3 (c)

Figure 3. Photomicrograph illustrating progressive changes in microstructure of a $3MgAl_2O_4 \cdot 1Fe_3O_4$ cathode with increasing distance away from slag/cathode interface. (320X)

(a) Porous slag (far left)/cathode interface. Reaction layer is a complex mixture of slag, metallic Fe (white particles) and Fe depleted $MgAl_2O_4$.

(b) Region ≈ 0.7mm away from interface. Iron from matrix has precipitated as metallic Fe particles at grain boundaries and pore surfaces.

(c) Region ≈ 1.4mm away from interface, iron from matrix has precipitated as FeO particles (light grey phase). Note transition from metallic Fe particles (white phase) at left to FeO particles.

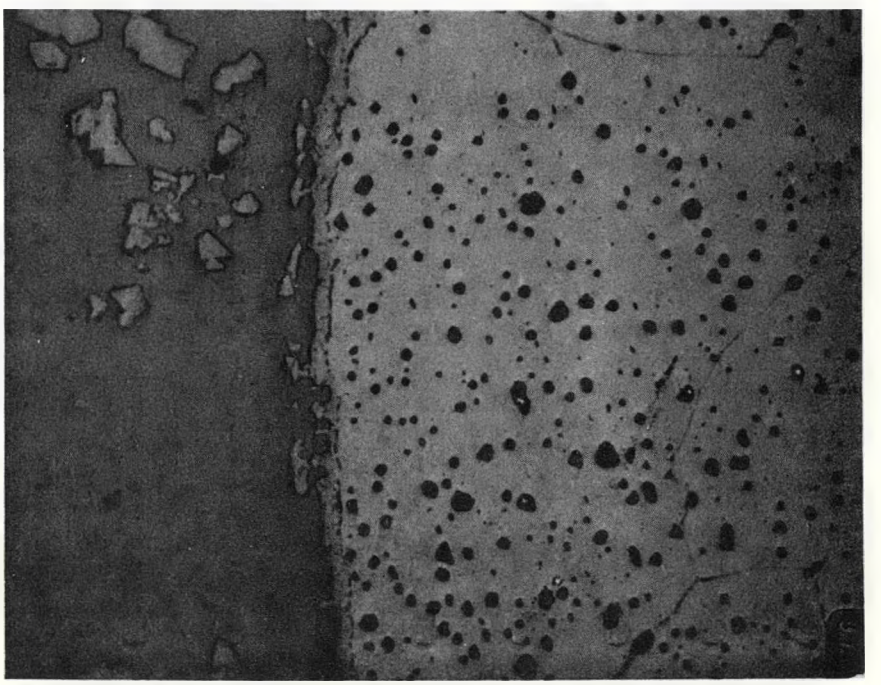

Figure 4. Photomicrograph of Slag (Left)/$3MgAl_2O_4 \cdot 1Fe_3O_4$ Anode Interface - Test 113. Note Iron Depleted $MgAl_2O_4$ Surface Reaction Scale. (320X)

B) Simulating the MHD anode arc by directing a seeded plasma flame from a high power oxyacetylene torch through a small experimental channel in the presence of flowing slag for extended periods of time and evaluating the electrochemical/ thermal reactions.

Although Approach B more closely simulates the MHD environment, Approach A is easier to implement promptly and is currently being pursued. It is also possible to use Approach A as a screening technique for evaluating different electrode materials and configurations.

Copper specimens were coated with 10-15 mils of plasma sprayed flyash and traversed by the arcs of several welders with different capabilities. These short term tests established the suitability of available equipment. Initial tests of longer duration with low intensity arcs that are closer to channel operating conditions are planned using a plasma needle arc welder and a turn-table. The welding torch is designed so that the arc is initiated within the torch and then transfers to the test sample which serves as the anode of the system. The magnitude of the current can be closely controlled to read the voltage drop across the arc. Using both meters it will be possible to monitor the power input into the anode. Initially, an uncooled rotating sample is mounted on the turntable and an arc directed against it. The arc track on the samples will have the shape of a circle. Copper and Inconel will be investigated first in order to determine if the laboratory tests rate the erosion resistance of these two materials in the same way as determined from previous arc erosion MHD channel tests. It is anticipated that a series of tests will be conducted on these materials in which the metals are: (a) uncooled, (b) coated with seed only, (c) with slag only and (d) with a combination of seed and slag. As indicated by the behavior of the slag layer in the short-term test, it will be necessary to provide a method of slag and seed replenishment to sustain a test of several hours duration.

2.0 WBS 1.2 - TEST ASSEMBLY FABRICATION

No significant activity was undertaken this quarter (see Section 5.2 for equivalent activity in support of the UO-2 Phase III Module).

3.0 WBS 1.3 - WESTINGHOUSE ELECTRODE SYSTEMS TEST FACILITY (WESTF)

3.1 Facility Design and Modification

After completing the series of three U-O2 Phase III proof tests, the test facility was made ready for a one hundred hour test in which the best materials selected from the U-O2 Phase III proof tests would be subjected to the conditions that they would see in the Soviet U-O2 facility. This test was to be run prior to the U-O2 Phase III test to provide additional information for the test. However, because preparations for this test would conflict with preparations for the scheduled test in the Soviet Union, it was recommended that the facility be converted to operate in the slagging mode. As soon as DOE concurred with this recommendation, the mixer and combustor (removed as a unit) were disassembled and rebricked to operate in the slagging mode (see Figure 5). The combustor, which is always free of seed or ash, was reconditioned and a new zirconia tube installed, and the mixer was rebricked with Norton magnesium aluminate (spinel) interlocking bricks. A copper water cooled nozzle was designed and is being machined.

The packed tower scrubber (Figure 6) was replaced by a Venturi scrubber to increase the particulate and potassium removal from the exhaust gas. By consulting with MIT personnel who had a similar problem, a Flex-Kleen Model OS-30 orifice scrubber was purchased and installed. Installation, including the associated plumbing and process modifications, was completed by March 1, 1978.

Facility operations and a test of the various sub-systems under slagging conditions will be made using a circular, refractory-lined dummy channel section. This test, number D-8, and subsequent tests (WESTF Test Nos. 40 through 43) are defined in Table 4.

For these tests, Montana Rosebud flyash will be injected into the mixer using the seed solution as a carrier. Several resins are being investigated to

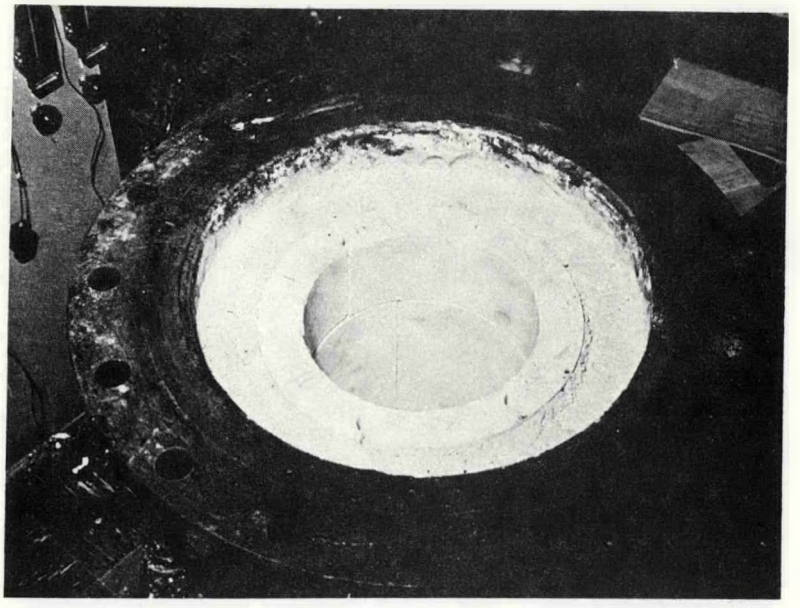

5(a)

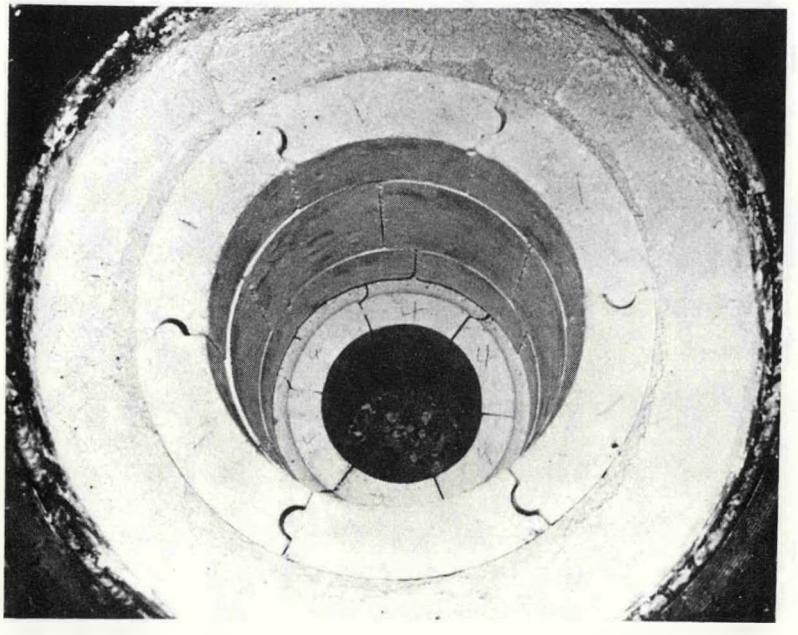

5(b)

Figure 5. Views of WESTF Rebricked Mixer Section

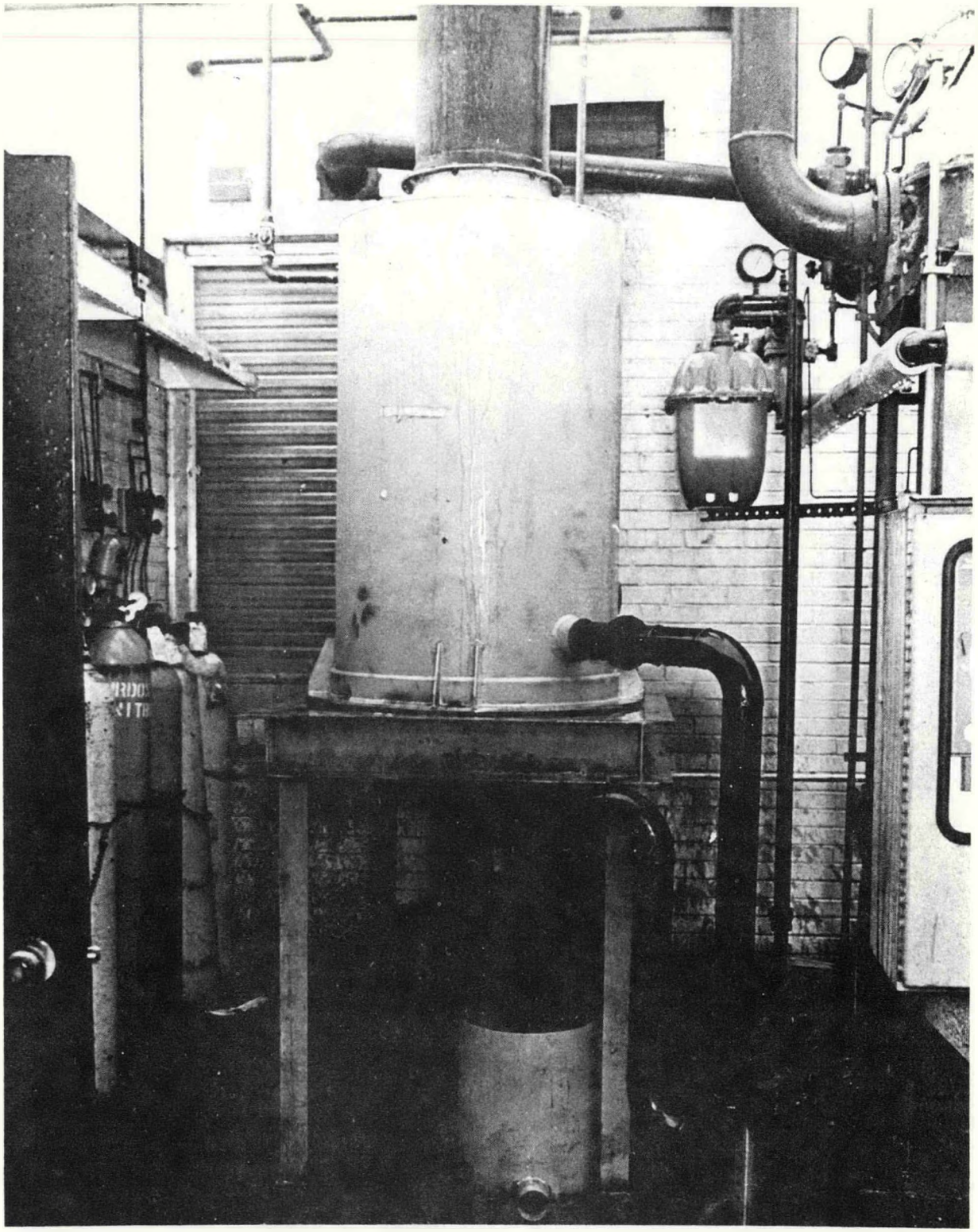

Figure 6. Venturi Scrubber Installed at WESTF

TABLE 4

WESTF TEST SUMMARY (DESIGN DATA)

Test Iden. No.	D-8	40	41	42	43
Electrode	Dummy	Cu (+) Cu (-)	Cu w Coat (+) Cu w Ni (-)	Fe (-) Pt (+)	$MgCr_2O_4$ Cr_2O_3
Surface Temp. - °C	Channel	~ 300	~ 300	1000-1300	1000-1400
Insulator		$MgAl_2O_4$	Al_2O_3 $MgAl_2O_4$ BN	$MgAl_2O_4$ Al_2O_3	$MgAl_2O_4$ Al_2O_3
Heat Flux, W/cm		100-150	100-150	~80	~75
Duration, Hrs	~5	10	10+	20	20
Fuel	Rosebud →				

suspend the flyash in solution without the need for continuous agitation. Also, oil is being considered as the carrier for seed and flyash to replace water injection and the associated drop in plasma temperature and plasma conductivity. An oil-seed-ash slurry injected into the mixer would be accompanied by a drop in primary fuel flowrate, and, in effect, make the mixer act as a secondary combustor.

Rearrangement and expansion of the control room has begun. Two additional control panels were installed to house eight additional power supplies, two Kaye Data Acquisition (DA) systems, and the "Facit" paper punches for the DA systems (see Figure 7). Eight Sorenson Model DCR300-18A power supplies were installed and can supply 18 amps at 400 volts DC each. They provide the capability to increase the loading of the electrode systems as well as provide an axial or simulated Hall voltage. They are in addition to the eight lower voltage power supplies that are already present in the electrical system.

The Data Acquisition systems will interface directly with the Data General Computer System and provide real time analysis and extended data storage. Difficulty was encountered in getting the Data General System on line because the fixed disk of the computer had to be loaded with the Fortran language programs by programming the removable disk and transferring this information to the fixed disk. This is not common practice and, as a result, much time was required by key Westinghouse personnel also involved in preparations for the UO-2 Phase III tests. Therefore, completion of this task had to be delayed until the Phase III module was delivered to the Soviet Union.

4.0 WBS 1.4 - WESTINGHOUSE MHD TEST FACILITY (WMTF)

No significant activity was undertaken this quarter. As requested by DOE, facility design and modification as well as test operations have been maintained on HOLD.

5.0 WBS 1.5 - COOPERATIVE US/USSR MHD PROGRAM

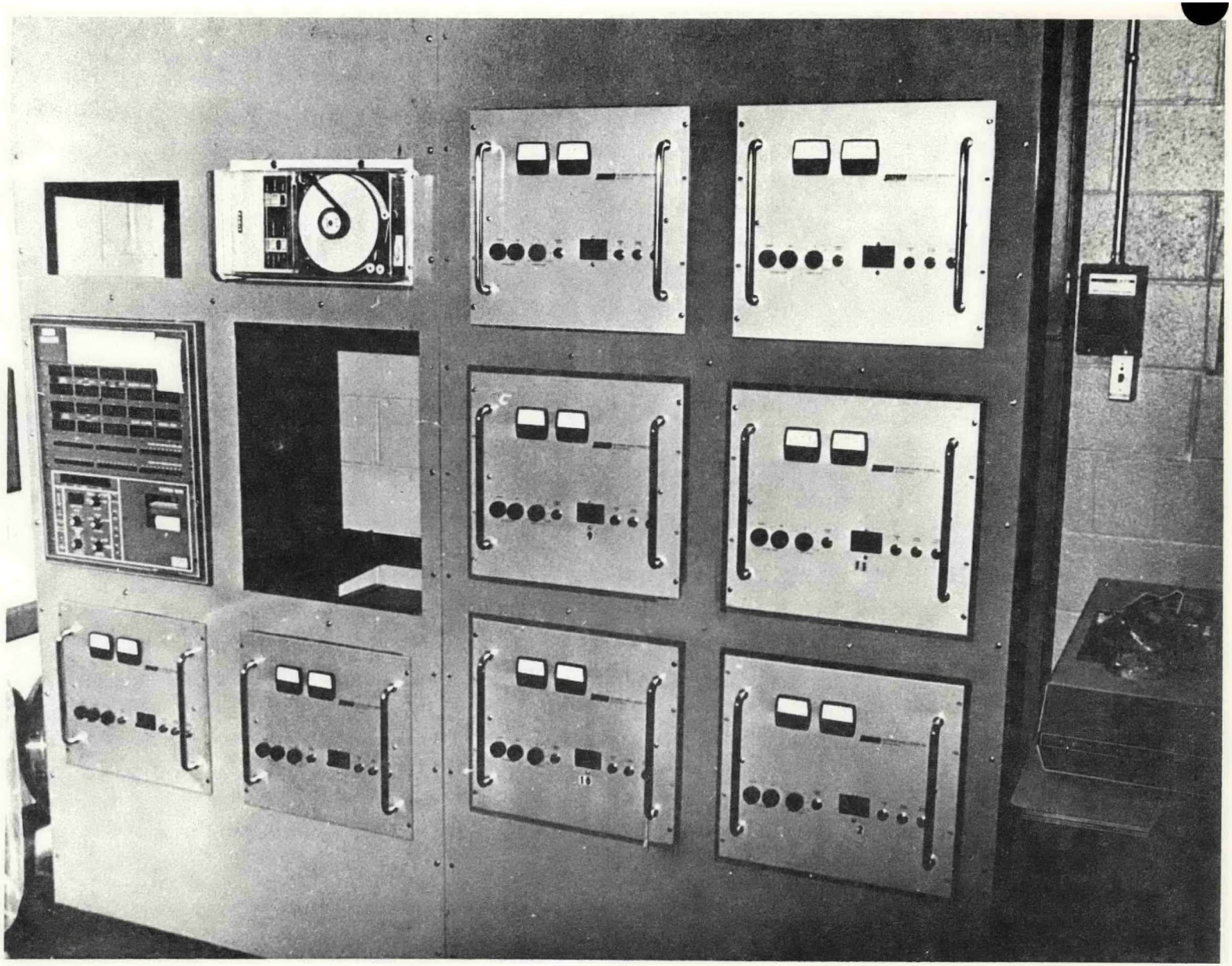

Figure 7. Additional WESTF Control Panels

5.1 WBS 1.5.1 - US/USSR Liaison

With the exception of that effort associated with the U-02 Phase III Module Test, no significant acitivity was completed during this quarter.

5.2 WBS 1.5.2 - U-02 Phase III Module

The objective of the U-02 Phase III Module Test, to be conducted in the U-02 Facility in May of 1978, is to evaluate the performance of refractory electrode systems during long term operation under MHD conditions with a clean fuel. For this module emphasis has been placed not only on electrode/insulator materials, but on current lead-out materials and attachments. Candidate electrode systems, summarized in Table 5, reflected a wide range of materials and fabrication techniques.

Desired operating conditions for the U-02 test are an electrode surface temperature of $\approx$1700°C and electrode heat fluxes of 16 to 20 w/cm^2. In contrast with the prior U-02 tests, the Phase III effort includes a series of three proof tests with the purpose of providing a basis for materials and design selection. The Proof Test Series were conducted in the Westinghouse Electrode System Test Facility (WESTF) from October 1977 through January 1978.

This reporting period saw the culmination of the Proof Test Series and the selection of materials and structures for the U-02 Phase III module. The design and development activity was directed towards the electrode systems for the U-02 module. Fabrication of module components, including the electrode sub-assemblies, were also completed during this period.

5.2.1 Material Development

Material development for the U-02 Phase III Module was conducted in the areas of electrodes, interelectrode insulations, and lead-out attachments.

5.2.1.1 Electrode Development

The overall philosophy for the Phase III tests was to include promising materials without significant development. In other words, development would be limited

TABLE 5

U-02 PHASE III MODULE CANDIDATE ELECTRODE SYSTEMS

Supplier	Attachment	Electrode	Fab.* Tech.	Insulator	Fab.* Tech.	Proof Test No.
GE	Flexbed	4 $MgAl_2O_4 \cdot 1Fe_3O_4$	S	$MgAl_2O_4$	S	1 (Oct. 77)
W/Technetics	Hoskins Mesh	3 $MgAl_2O_4 \cdot 1Fe_3O_4$	PS	$MgAl_2O_4$	S	1 (Oct. 77)
ANL	HfO_2 - Metal Composite		HP	$MgAl_2O_4$	PS	1 (Oct. 77)
W/EP	Ag Epoxy	$LaCrO_3/ZrO_2$ Cap[1]	HP	MgO	S	2 (Nov. 77)
W/APS	Cermet	$LaCrO_3/ZrO_2$ Cap[2]	PS	$MgAl_2O_4$	PS	2 (Nov. 77)
W	Ag Epoxy	$LaCrO_3$ - ZrO_2[3]	HP	$MgAl_2O_4$	S	2 (Nov. 77)
W/Technetics	Nickel Mesh	$La_{.95}Mg_{.05}CrO_3$	HP	$MgAl_2O_4$	S	2 (Nov. 77)
W	Ag Epoxy - Au	$LaCrO_3$- $LaAlO_3$[4]	HP	MgO	HP	3 (Jan. 78)
W	Ag Epoxy - Pt	.5 $LaCrO_3 \cdot 5$ $SrZrO_3$	HP	$MgAl_2O_4$	S	3 (Jan. 78)
GE	Flexbed	$LaCrO_3$	S	$MgAl_2O_4$	S	3 (Jan. 78)
W/APS	$FeAl_2O_4$	3 $MgAl_2O_4 \cdot 1Fe_3O_4$	PS	$MgAl_2O_4$	PS	3 (Jan. 78)

*PS - Plasma Spray
S - Sintered
HP - Hot Pressed

[1] $La_{.95}Mg_{.05}Cr_{.9}Al_{.1}O_3/.85ZrO_2$-$.12CeO_2$-$.03Y_2O_3$ Cap

[2] $La_{.95}Mg_{.05}CrO_3/.85ZrO_2$-$.12CeO_2$-$.03Y_2O_3$ Cap

[3] $La_{.95}Mg_{.05}CrO_3/.90ZrO_2$-$.10Y_2O_3$ Composite

[4] $La_{.95}Mg_{.05}Cr_{.85}Al_{.15}O_3$(cold) graded to $La_{.95}Mg_{.05}Cr_{.68}Al_{.32}O_3$ (hot)

to adapting materials and structures to U-02 designs. This meant the development of very thick electrode structures (due to the very low U-02 heat fluxes).

Fabrication Technique

The electrode materials and structures selected for the U-02 module on the basis of their performance in the U-02 Phase III proof tests (see Section 5.2.2) were developed and fabricated at the Westinghouse R&D Center. The fabrication efforts on the six selected electrode structures are summarized below.

The six (6) selected electrode groups consist of five different $LaCrO_3$ based compositions which were all hot-pressed to high densities. The compositions are as follows:

(1) $La_{.95}Mg_{.05}CrO_3$ with $88ZrO_2 - 12Y_2O_3$ dispersed in the matrix

(2) A layered structure of two compositions - $LaMg_{.02}Al_{.23}Cr_{.75}O_3$, $LaMg_{.02}Cr_{.85}Al_{.13}O_3$

(3) A layered structure of four compositions -

$La_{.95}Mg_{.05}CrO_3$ with 30 w/o $88ZrO_2 - 12Y_2O_3$

$La_{.95}Mg_{.05}CrO_3$ with 20 w/o $88ZrO_2 - 12Y_2O_3$

$La_{.95}Mg_{.05}CrO_3$ with 10 w/o $88ZrO_2 - 12Y_2O_3$

$La_{.95}Mg_{.05}CrO_3$ with 0 w/o $88ZrO_2 - 12Y_2O_3$

(4) $La_{.95}Mg_{.05}CrO_3$

(5) $La_{.95}Mg_{.05}CrO_3$ with $88ZrO_2 - 12Y_2O_3$ dispersed in the matrix (same as (1), but designed for a lower surface temperature).

(6) $LaMg_{.02}Cr_{.98}O_3$

The first and fifth structures consists of a mechanical mixture of $La_{.95}Mg_{.05}CrO_3$ powder (Transtech, Gaithersburg, MD., and 30 w/o coarse (-40 + 70 mesh) fused $88ZrO_2 - 12Y_2O_3$ grains (Norton Company, Worchester, Mass.) The addition of refractory ZrO_2 grains to $LaCrO_3$ increases its erosion resistance and decreases its volatilization rate. The material was hot-pressed at 4000 psi and 1650°C for 2-3 hours. The second structure consists of two compositional layers - the

top half of the electrode is comprised of $LaMg_{.02}Al_{.23}Cr_{.75}O_3$ and the bottom half of $LaMg_{.02}Cr_{.85}Al_{.13}O_3$. (Both powders obtained from A-T Research, Vichy, Missouri.) Substituting Al for Cr lowers the volatilization rate of the material while again increasing its refractory properties. The material was hot-pressed at 3000 psi and 1650°C for 2-3 hours. The third structure consists of four equal thicknesses of $La_{.95}Mg_{.05}CrO_3$ with 30, 20, 10, 0 w/o $88ZrO_2$ - $12Y_2O_3$ dispersed in the matrix. Grading to pure $La_{.95}Mg_{.05}CrO_3$ improves the electrical conductivity and reduces the potential for excessive joule heating at the backface of the electrode. The material was hot-pressed at 4000 psi and 1650°C for 2-3 hours. The fourth structure is comprised solely of $La_{.95}Mg_{.05}CrO_3$. (Transtech, Gaithersburg, Md.) The pressing conditions were the same as for group 2. The sixth structure consists of $LaMg_{.02}Cr_{.98}O_3$ (A-T Research, Vichy, Missouri). The substitution of Mg for Cr instead of La may deter the formation of more ractive second phases which would be readily leached away. The pressing conditions were again identical to those of group 2.

All six electrode structures were hot-pressed using a graphite die which yielded 3" by 5" billets. An R. F. generator was used to heat the powder and graphite components in a static nitrogen atmosphere. A 2" diameter hydraulic press applied the required pressure. After hot-pressing, the billets were sliced and ground to provide properly dimensioned electrodes. The electrodes were then oxidized at 1600°C to significantly improve their electrical conductivity. Figure 8 shows the significant decrease in electrical resistance of $LaCrO_3$ as the annealing time is increased from 2 hours to 8 hours. The effect of contact resistance was minimized by sputtering a gold film on the $LaCrO_3$ surface prior to taking these measurements. A minimum of 8 hours at temperatures of 1500-1600°C appears necessary for oxygen to diffuse into the electrodes to provide a conductivity adequate for the proposed UO-2 current passage. Lower temperatures (such as 1200°C) were found unacceptable in increasing the conductivity sufficiently through the bulk of the materials.

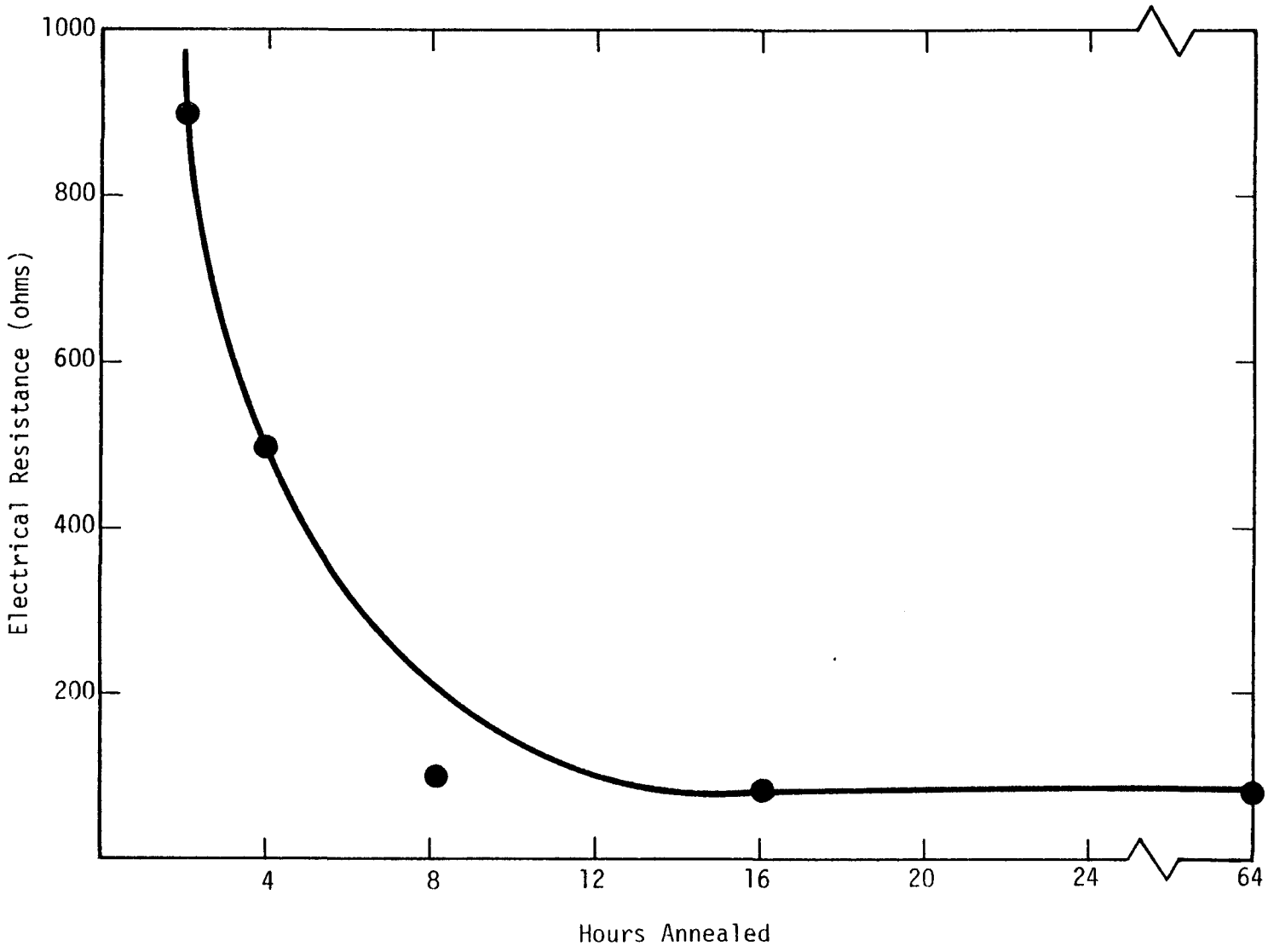

Figure 8. Electrical Resistance of $LaCrO_3$ MHD Electrodes vs. Number of Hours of Annealing at 1600°C.

Interelectrode Insulators

The interelectrode insulation selected for the U-02 module were both magnesia and spinel based on nearly equal performance in the proof tests. However, two grades differing in density were available for fabricating the insulation for the U-02 Phase III electrode walls. In order to differentiate quantitatively between these materials, diffusion couples of lanthanum chromite and magnesia or spinel were heated for 100 hours at 1650°C. The couples consisted of a slab of lanthanum chromite between slabs of magnesia or spinel. Magnesia of two different densities, 97% and 84%, and a spinel 97% dense were tested. Chromium profiles were obtained by ion microprobe analysis and are shown in Figure 9. Chromium penetrated the high density magnesia and the spinel to a depth of only 175 microns, but completely penetrated the low density magnesia sample. The high density magnesia and the spinel were comparable and compatible with lanthanum chromite electrodes; both will be used as ceramic interelectrode insulators for the U-02 Phase III electrode walls.

Alternate Design

An alternate electrode design concept using a platinum pin inserted into $LaCrO_3$ electrode material (to counteract electrochemical effects and accelerated seed diffusion in the cathode wall) was developed and tested. The following gives the rationale supporting this design and describes the tests conducted to justify incorporating this design into one set of cathodes in the U-02 module.

Post test analysis of $LaCrO_3$ based electrodes used in the U-02 proof tests, coupled with our understanding of electrochemical reactions from laboratory scale experiments, leads to the conclusion that $LaCrO_3$ undergoes two basic electrochemical reactions in clean gas fired MHD conditions.

The first major reaction involves the loss of oxygen ions from the cathode wall electrodes into the plasma and the gain of oxygen from the plasma into the anode wall; (i.e. $O^{-2} = 1/2\ O_2 + 2e^-$ at the cathode/plasma interface and $1/2\ O_2 + 2e^- = O^{-2}$ at the anode/plasma interface). Such reactions are manifested in $LaCrO_3$,

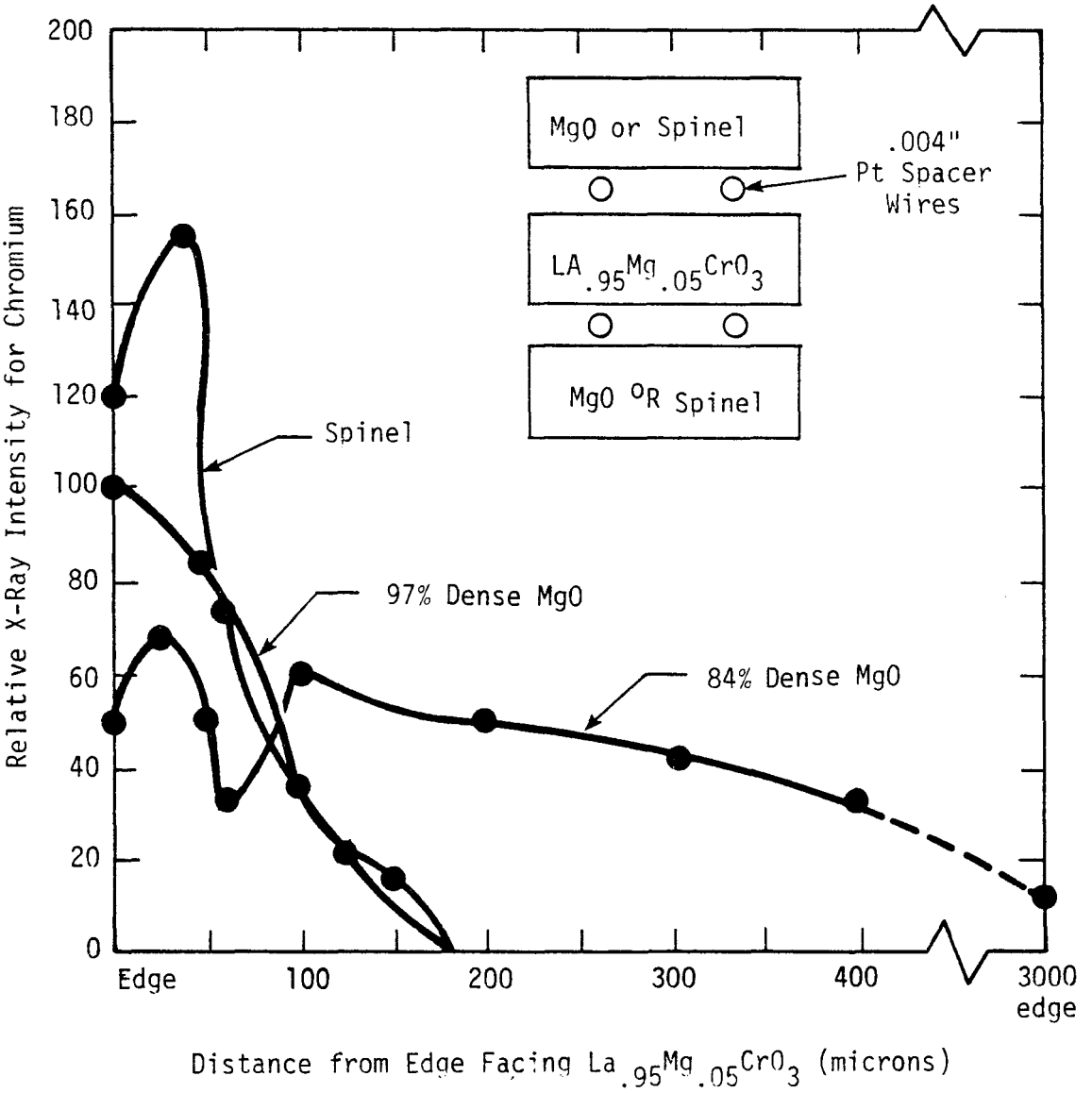

Figure 9. Chromium Diffusion in Interelectrode Insulating Material

whose color is very sensitive to Po_2, by a green coloration of the electrodes at the cathode wall and by a black hue at the anode wall. The underlying factor effecting the thermodynamics of these reactions is the voltage drop (E = IR) across the electrode. Since theoretically, only $\approx$1.7 volts are needed to decompose $LaCrO_3$* to its elements at 1400°C, it is advisable that the electrode thickness be selected such that the critical value of the voltage is not greatly exceeded. This is especially important at the cathode wall where reducing conditions predominate, a condition under which $LaCrO_3$ and, in fact, most oxides become unstable. At the anode wall, oxidizing conditions predominate and since oxides are stable in these atmospheres, the requirements on electrode thickness is of lesser importance.

The second basic electrochemical reaction, the transport of K^+ to and through the cathode wall is also voltage dependent. Potassium ions are preferentially attracted to the cathode wall due to the voltage gradient in the plasma. Now, hypothetically speaking, if there were no voltage drop in the cathode (i.e.; zero current or resistance), the K^+ would slowly diffuse from the plasma through the electrode matrix resulting in very little corrosion attack; i.e., K^+ flux would not be much greater than that in the anodes where degradation of the electrode due to K^+ attack has been experimentally determined in the U-02 proof tests to be minor. In reality, however, there is a large voltage gradient in the thick $LaCrO_3$ electrodes proposed for the U-02 tests, such that K is actually driven into the $LaCrO_3$ and is pumped down the voltage gradient at a very rapid rate. This is a likely contributing cause for the very severe "mid-band" corrosion region in the cathode, where potassium condenses out at pores and cracks as a liquid corrodent (i.e., between the 900°C and 1300°C isotherms).

To minimize both the electrochemical reduction process as well as the accelerated K^+ diffusion process in the cathode wall, it is necessary to reduce the voltage gradient across the cathode. This may be accomplished by using very thin and/or

*$E = \frac{\Delta G^o}{nF}$ where E = voltage across electrode, ΔG^o = free energy for decomposition reaction, n = No. of electrons transferred in reaction, F = Faraday constant.

very electrically conductive ceramic coatings on a conductive metallic lead-out. An alternate approach, which will be employed in one group of cathodes in the U-02 module, is to use low resistance Pt pins or rods which are inserted into the $LaCrO_3$ - ZrO_2 composite material. The pins are positioned sufficiently high up in the electrode so that the current can be drawn off at temperatures greater than 1300°C. This ensures that the voltage gradient is minimized in the critical temperature range of 900°C - 1300°C where potassium compounds can condense.

To investigate stability of Pt pins in contact with $LaCrO_3$, high temperature electrical tests are being performed. In one test, .040" O.D. x .028" I.D. Pt tubes were cemented (with Pt paste) into close tolerence holes drilled into opposing walls of ≈ 1 cm^2 rectangular cross-section $LaCrO_3$ specimens. The distance between tube tips in the $LaCrO_3$ was ≈ 1 cm. A constant 0.8 amp. direct current was passed across the sample (current density at tube tips ≈ 190 Amp/cm^2 for 90 hours at 1300°C. The voltage drop across the sample decreased less than 15% over the course of the test. Metallographic analysis of the sectioned sample revealed no evidence for chemical interaction nor cracking at the $LaCrO_3$/Pt interfaces. A similar test using a 30 w/o ZrO_2 - 70 w/o $LaCrO_3$ composite sample with solid .040" Pt pins carrying a constant 1.2 amp direct current (≈ 150 Amp/cm^2 at pin ends) for 80 hours at 1300°C also indicated good electrical stability (i.e., $\approx 15\%$ voltage decrease with time). This electrode structure was also in good condition at the end of the test.

5.2.1.2 Electrode/Insulator Characterization

Pre-test characterization of the electrodes/insulators being run in the U-02 Phase III Test is necessary to fully evaluate the materials' performance. These properties include: thermal and electrical conductivity, thermal expansion, elastic modulus, fracture strength, chemical composition, phase composition, microstructure and porosity.

Densities - Porosities

Table 6 lists the density and amount of open porosity for each of the six groups of electrodes to be run in the U-02 Phase III Test. All of the electrodes have a density of greater than 96% of theoretical. Dense electrodes are desired to reduce open porosity and decrease the amount of potassium seed penetration. Groups 1 and 5 ($La_{.95}Mg_{.05}CrO_3/88ZrO_2$-$12Y_2O_3$ composite) had the greatest amount of open porosity, most likely due to the concentration of pores at the $LaCrO_3$ matrix/ZrO_2 grain interface. The angularity of the ZrO_2 grains contributed to the concentration of pores at these junctures.

Thermal Conductivity

Thermal conductivity measurements were made on a number of electrode materials in the U-02 Phase III Test. These measurements were conducted at Battelle Pacific Northwest Laboratories using a laser pulse technique.

Figure 10 shows the thermal conductivity for three electrode materials, $LaMg_{.02}Cr_{.98}O_3$, $LaMg_{.02}Cr_{.85}Al_{.13}O_3$, and $LaMg_{.02}Cr_{.75}Al_{.23}O_3$. It is quite apparent that the substitution of Cr for Al will markedly increase the conductivity, although the relative slope of the curve does not change.

Electrical Conductivity

The electrical conductivity of electrode and insulator materials for the U-02 Phase III Test were determined by the National Bureau of Standards using a D.C. four probe technique. Data was measured at 10^{-3} O_2 in N_2 to simulate the partial pressure of oxygen in an actual MHD environment.

Figure 11 shows the electrical conductivity of $LaMg_{.02}Cr_{.98}O_3$ with different amounts of Al substituted for Cr. For all three compositions there is a substantial drop in conductivity below 400°C. The relative slope of each of the conductivity curves is practically identical throughout the temperature range. Figure 12 shows the electrical conductivity of $LaMg_{.02}Cr_{.98}O_3$ as a

TABLE 6. DENSITIES AND POROSITIES OF PHASE III U-O2 ELECTRODES

Group No.	Electrodes	% Theoretical Density	Total Porosity (%)	Open Porosity (%)
1	$La_{.95}Mg_{.05}CrO_3/88ZrO_2\text{-}12Y_2O_3$ composite	97.1	2.87	0.97
2	$La\ Mg_{.02}Cr_{.85}Al_{.13}O_3$ graded to $La\ Mg_{.02}Cr_{.75}Al_{.23}O_3$	96.6	3.37	0.56
3	Graded $La_{.95}Mg_{.05}CrO_3/88ZrO_2\text{-}12Y_2O_3$ composite	98.1	1.89	0.39
4	$La_{.95}Mg_{.05}CrO_3$	97.4	2.56	0.77
5	$La_{.95}Mg_{.05}CrO_3/88ZrO_2\text{-}12Y_2O_3$ composite	96.7	3.32	1.35
6	$LaMg_{.02}Cr_{.98}O_3$	96.1	3.94	0.29

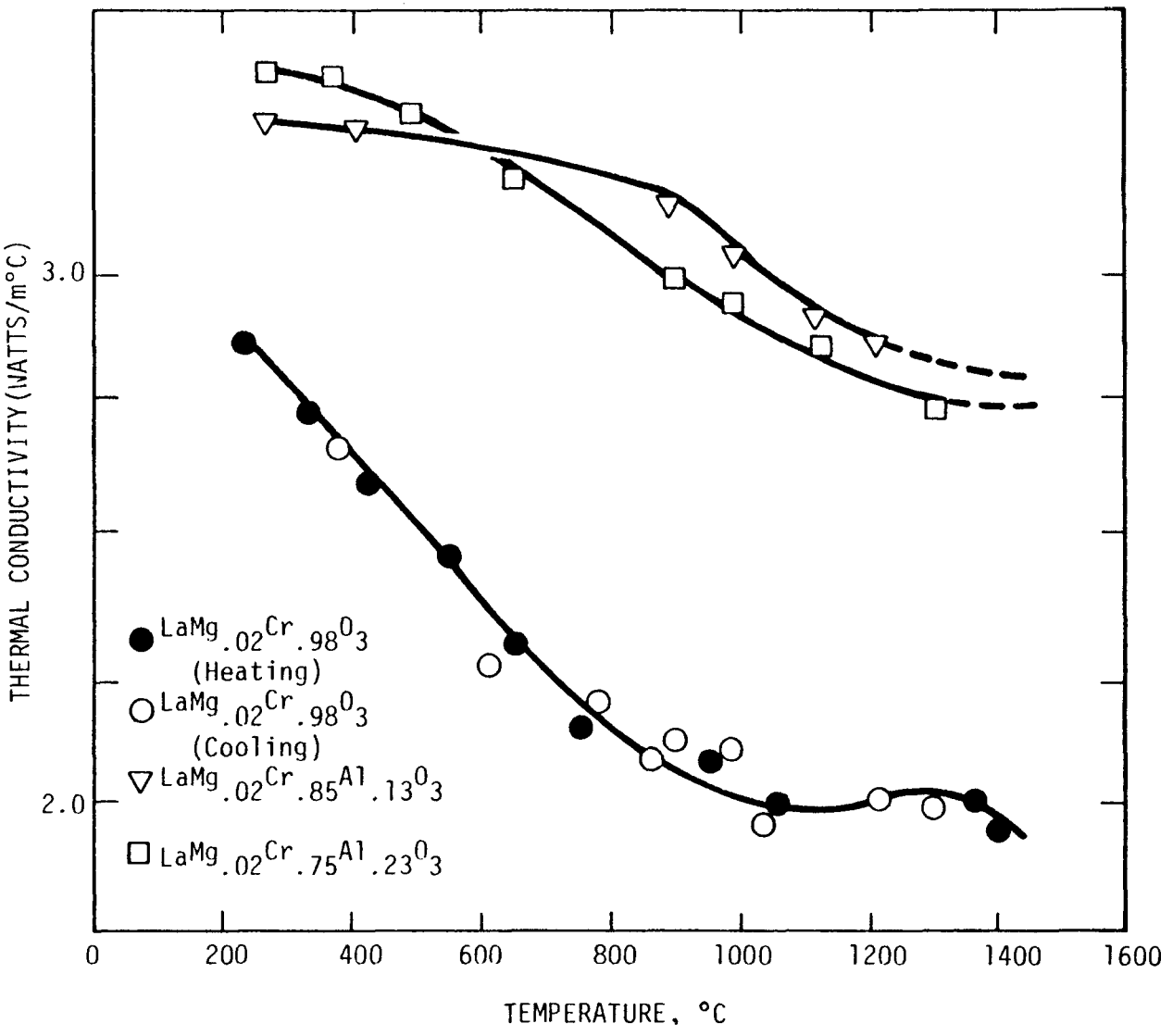

Figure 10. Thermal Conductivity of $LaMg_{.02}Cr_{.98}O_3$ with additions of alumina. Data taken at Battelle-Northwest

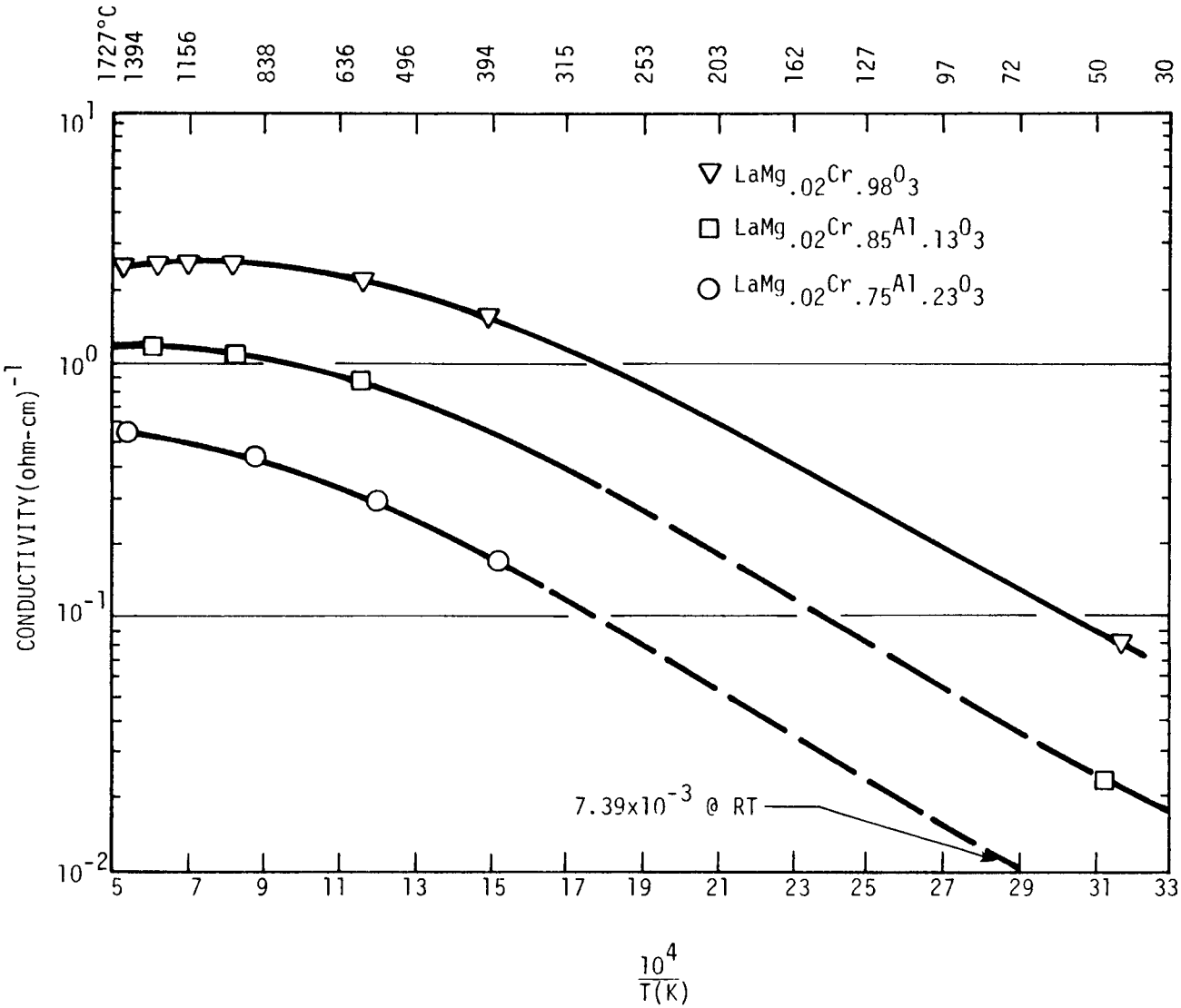

Figure 11. Electrical Conductivity of $LaMg_{.02}Cr_{.98}O_3$ with additions of alumina. Data taken at $10^{-3}O_2$ in N_2 by NBS. Material hot-pressed at 1650°C and 3000 psi.

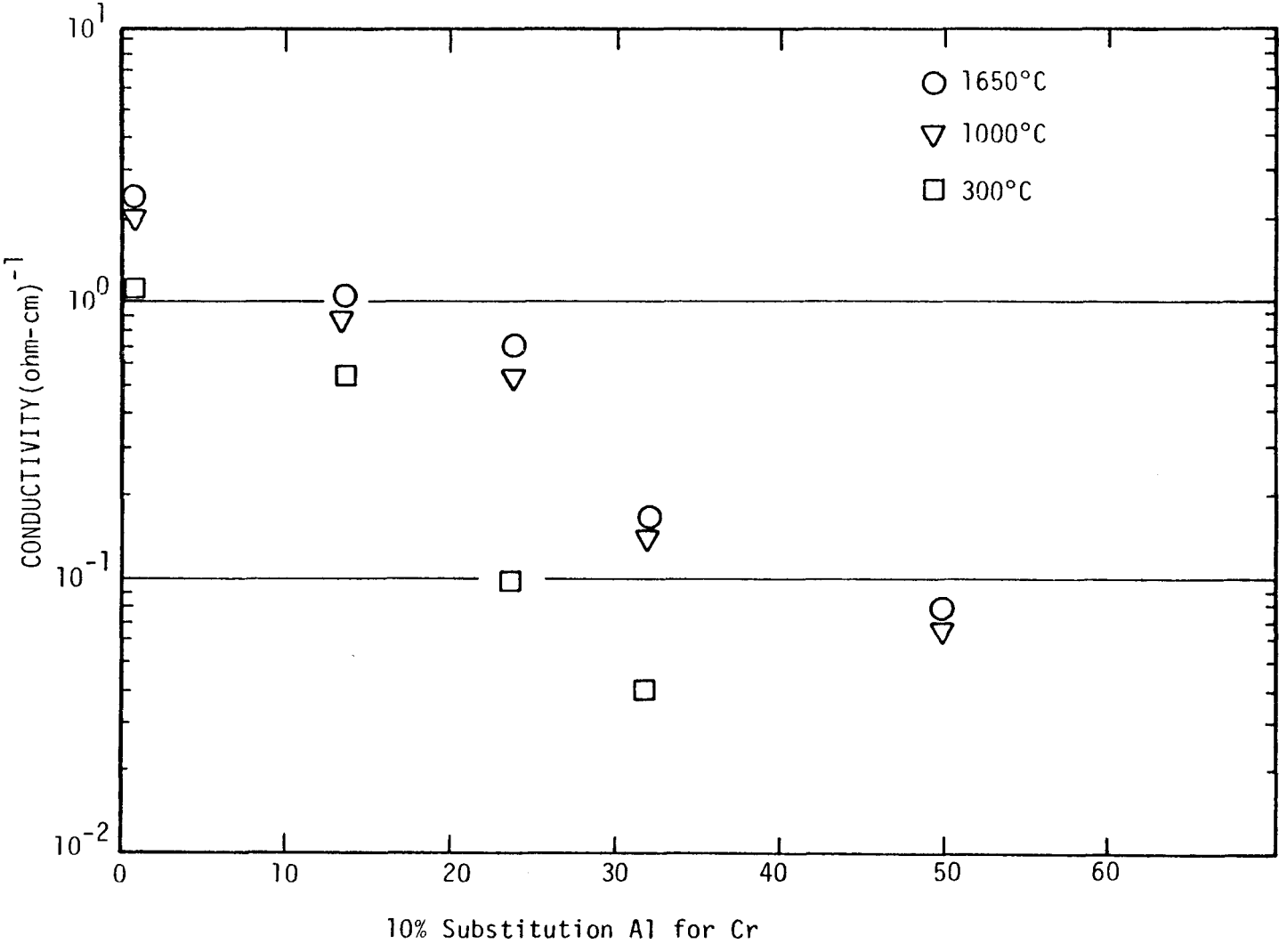

Figure 12. Electrical Conductivity of $LaMg_{.02}Cr_{.98}O_3$ with Increasing Amounts of Al Substituted for Cr Data Taken at $10^{-3}O_2$ in N_2.

function of the amount of Al substituted for Cr. It is clear that the compositional change (substitution of Al for Cr) has a greater effect on the conductivity than does a temperature change. For the U-02 Phase III module, this material will be graded (large amount of Al substitution at the hot face to smaller amounts of the backface) to maintain a fairly uniform conductivity.

Spectrochemical Analysis

The purity of the electrodes for the U-02 Phase III module was measured on random samples by emmision spectroscopy at Westinghouse R&D Center. Both powders and bulk samples were analyzed. One powder ($LaMg_{.02}Al_{.13}Cr_{.85}O_3$) was analyzed by spark source spectrochemical methods by an outside laboratory to compare results. The data are tabulated in Table 7.

X-Ray Analysis

X-ray analysis of the starting U-02 powders detected no secondary phases. Lattice parameters of the powders are shown below.

	a	b	c
$La_{.95}Mg_{.05}CrO_3$	5.48	5.51	7.76
$LaMg_{.02}Cr_{.98}O_3$	5.49	5.49	7.76
$LaMg_{.02}Al_{.13}Cr_{.85}O_3$	5.42	5.50	7.73
$LaMg_{.02}Al_{.23}Cr_{.75}O_3$	5.41	5.47	7.72

The parameters are quite similar but do reveal a distortion of the orthorhombic lattice as Al is substituted for Cr.

Electrode Microstructure

Five different electrode materials are included in the U-02 Phase III module. These materials were all hot-pressed to high densities at Westinghouse R&D Center. SEM photomicrographs of the fractured surface of each material are

TABLE 7. SPECTROCHEMICAL ANALYSIS OF ELECTRODE MATERIALS (PPM)

Element	$LaMg_{.02}Cr_{.98}O_3$		$LaMg_{.02}Cr_{.75}Al_{.23}O_3$		$LaMg_{.02}Cr_{.85}Al_{.13}O_3$		$La_{.95}Mg_{.05}CrO_3$		$LaMg_{.02}Cr_{.85}Al_{.13}O_3$
	Powder	Bulk	Powder	Bulk	Powder	Bulk	Powder	Bulk	*Powder
Al	< 100		> 1%		~ 1%		600		major
Ag	< 10	< 10	< 10	< 10	< 10	< 10	< 10	< 10	< 0.1
B	< 100	< 100	< 100	< 100	< 100	< 100	< 100	< 100	14
Ba	< 100	< 100	< 100	< 100	< 100	< 100	< 100	< 100	98
Be	< 10	< 10	< 10	< 10	< 10	< 10	< 10	< 10	< 0.15
Bi	< 100	< 100	< 100	< 100	< 100	< 100	< 100	< 100	< 0.42
Ca	< 100	< 100	< 100	200	< 100	< 100	200	< 100	86
Cd	<1000	<1000	<1000	<1000	<1000	<1000	<1000	<1000	< 0.23
Co	< 100	< 100	< 100	< 100	< 100	< 100	< 100	< 100	2.1
Cr	≥ 10%	≥ 10%	≥ 10%	≥ 10%	≥ 10%	≥ 10%	≥ 10%	≥ 10%	major
Ca	< 10	200	< 10	< 10	< 10	< 10	< 10	< 10	6.8
Fe	100	1000	100	< 100	100	< 100	< 100	< 100	50
K	< 100	< 100	< 100	< 100	< 100	< 100	< 100	< 100	240
Li	50	20	40	< 10	30	30	30	< 10	23
Mg	3000	3000	3000	5000	3000	3000	5000	3000	> 0.5 %
Mn	< 100	< 100	< 100	< 100	< 100	< 100	< 100	< 100	5.0
Mo	< 100	< 100	< 100	< 100	< 100	< 100	< 100	< 100	0.70
Na	50	1000	200	< 50	200	< 50	< 50	< 50	690
Nb	< 100	< 100	< 100	< 100	< 100	< 100	< 100	< 100	< 0.1
Ni	< 100	< 100	< 100	< 100	< 100	< 100	< 100	< 100	1.9
P	<1000	<1000	<1000	<1000	<1000	<1000	<1000	<1000	7.3
Pb	< 100	< 100	< 100	< 100	< 100	< 100	< 100	< 100	1.2
Sb	< 100	< 100	< 100	< 100	< 100	< 100	< 100	< 100	< 0.1
Si	200	100	200	300	300	300	200	300	700
Sn	< 100	< 100	< 100	< 100	< 100	< 100	< 100	< 100	0.16
Sr	<1000	<1000	<1000	<1000	<1000	<1000	<1000	<1000	1.3
Ti	< 100	< 100	< 100	< 100	< 100	< 100	< 100	< 100	0.90
V	< 100	< 100	< 100	< 100	< 100	< 100	< 100	< 100	0.37
Zn	< 100	< 100	< 100	< 100	< 100	< 100	< 100	< 100	4.7
Zr	< 100	< 100	< 100	< 100	< 100	< 100	< 100	< 100	0.45

S - 200
CL - 56
F - 100
Yt - 1.7
Nd - 47
Pr - 77
Ce - 50

*Accu-Labs, Wheatridge, CO. 80033

shown in Figures 13 and 14. $LaMg_{.02}Cr_{.98}O_3$ and $La_{.95}Mg_{.05}CrO_3$ have relatively small average grain sizes (4.3 and 3.4 μm, respectively) as compared to the other three materials. The grains are predominantly spherical and of similar size. The fracture mode is primarily intergranular. Porosity is confined to the grain boundaries, with no apparent voids in the individual particles. The $La_{.95}Mg_{.05}CrO_3/88ZrO_2$-$12Y_2O_3$ composite has a slightly larger average grain size (6.2 μm), and the grains are not of a uniform size, but are a conglomeration of course and fine particles. The 88 ZrO_2-$12Y_2O_3$ grain (-30 +70 mesh) which accounts for 30 w/o of the material is not shown in the micrograph. The fracture mode is still primarily intergranular. The Al doped electrode material, $LaMg_{.02}Cr_{.85}Al_{.13}O_3$ and $LaMg_{.02}Cr_{.75}Al_{.23}O_3$, have larger grain sizes, 14.6 μm and 11.4 μm, respectively. Most of their porosity is at triple points and grain boundaries. There are, however, some cavities in the interior of the larger grains that were not evident in the other materials. The fracture mode of $LaMg_{.02}Cr_{.75}Al_{.23}O_3$ is primarily intergranular whereas $LaMg_{.02}Cr_{.85}Al_{.13}O_3$ has a good deal of transgranular fracture as evidenced by the cleavage steps. Both of the Al doped materials have more angular grain shapes in contrast to the spherical shapes prevelant for the first three compositions.

5.2.1.3 Attachment Development

Between the proof tests and U-02 module fabrication, development work on attachments continued. Efforts were made to find suitable alternate attachments for the conductive epoxy or the active metal brazing alloy used on the Westinghouse lanthanum chromite electrodes in the U-02 proof tests. However, no alternate attachments were developed that were equal to or better than the attachments used in the proof tests. In addition to seeking new attachments additional work was directed towards improving the proof test attachments.

Problems associated with conductive epoxy attachments in the proof tests were found to be due to high contact resistances that caused overheating in the bond area. These resistances can be substantially reduced by sputtering a gold or platinum film onto the lanthanum chromite surface before making the epoxy attachment. Electrode samples prepared in this manner using ceramic pieces with good conductivity give satisfactory performance in bench scale tests.

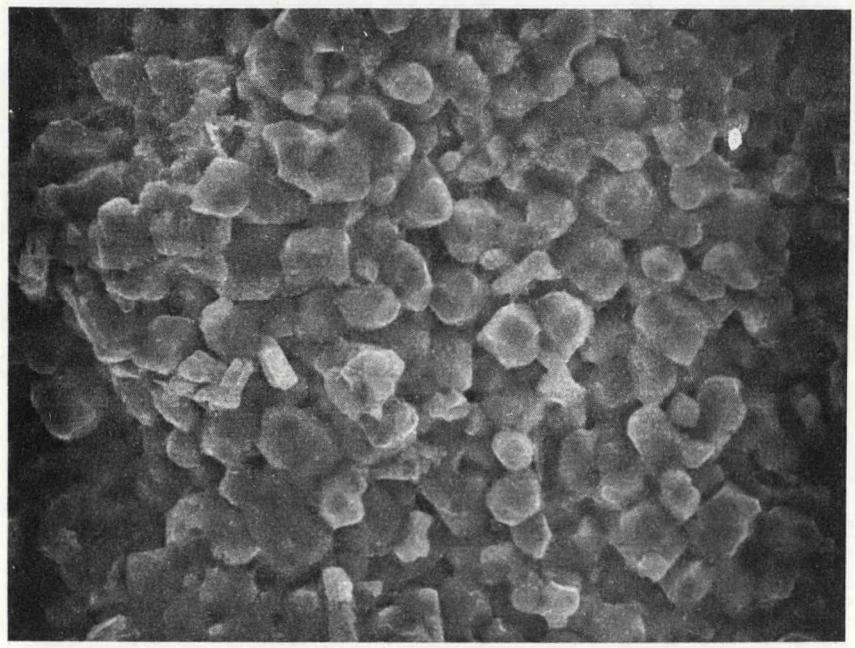

(a) $LaMg_{.02}Cr_{.98}O_3$ — 1500X, Grain Size = 4.3 μm

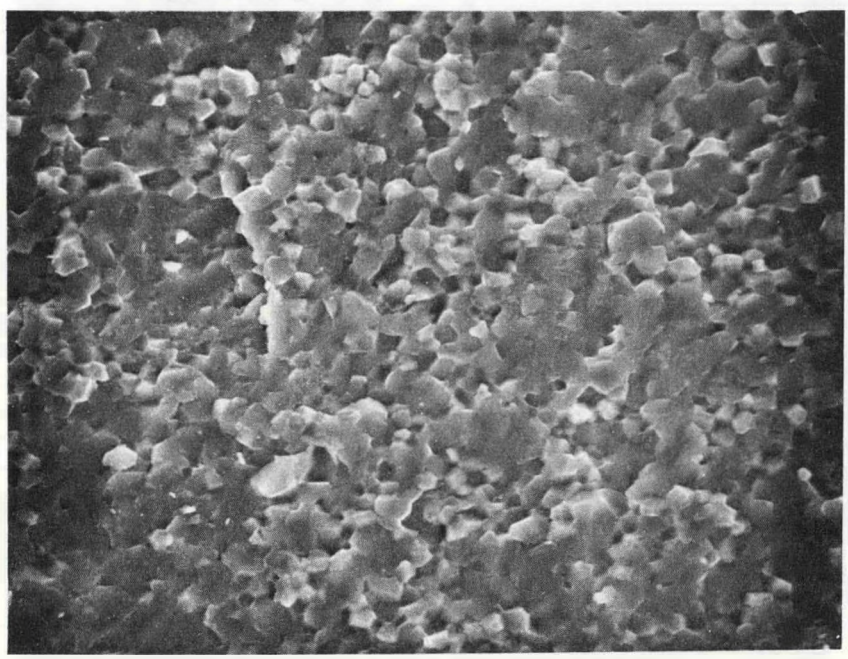

(b) $La_{.95}Mg_{.05}CrO_3$ — 1500 X, Grain Size = 3.4 μm

Figure 13. SEM Photomicrographs of Fractured Surfaces of $LaCrO_3$ Electrode to be Used in the U-02 Test

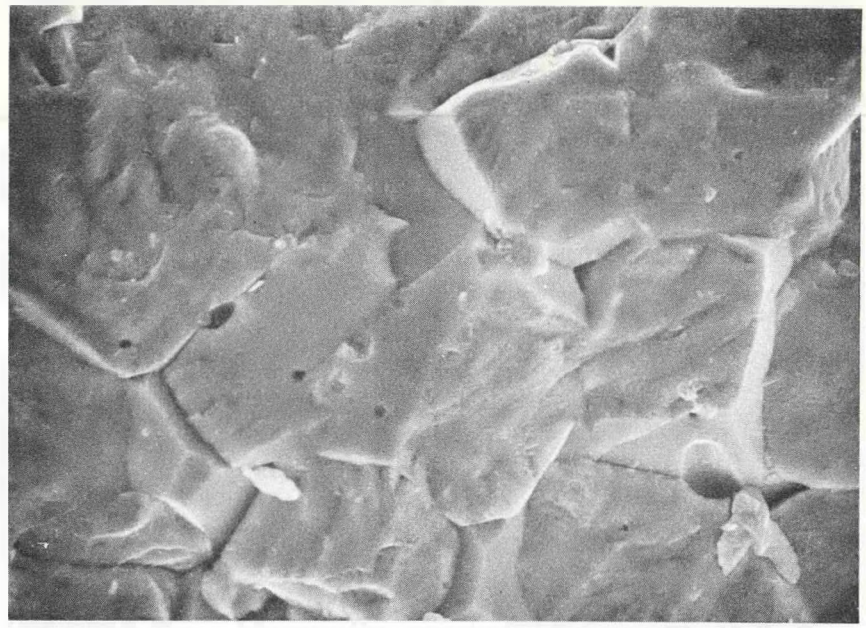

(b) $LaMg_{.02}Cr_{.85}Al_{.13}O_3$ 1500X Grain Size = 14.6 μm

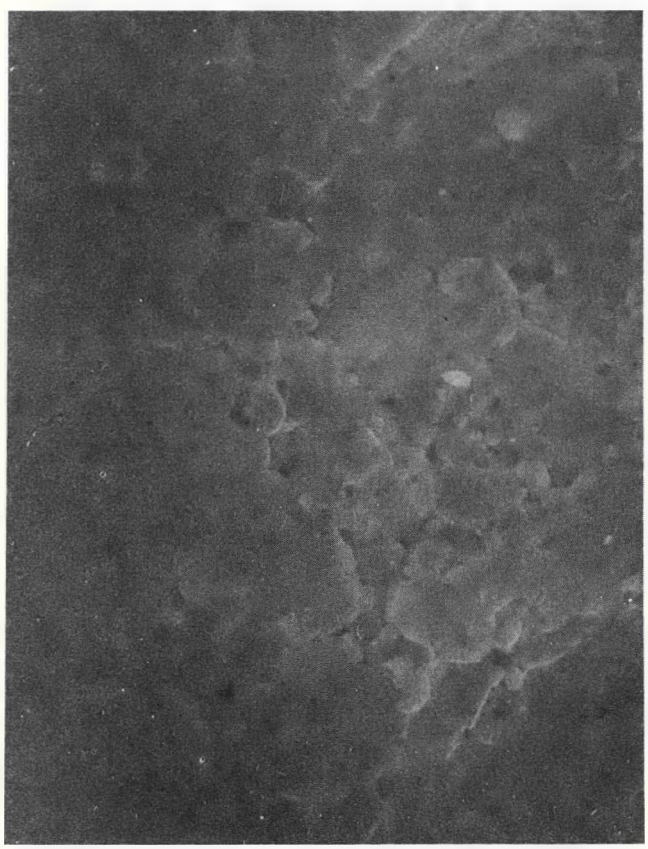

(a) $La_{.95}Mg_{.05}CrO_3/88ZrO_2$-12 Y_2O_3
1500X Grain Size = 6.2 μm

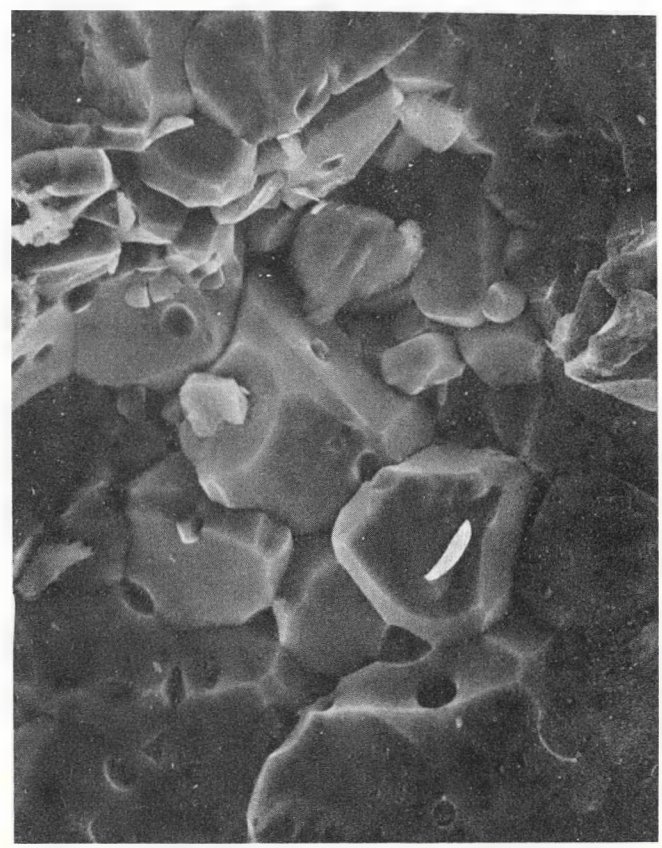

(c) $LaMg_{.02}Cr_{.75}Al_{.23}O_3$ 1500X
Grain Size=11.4 μm

Figure 14. SEM Photomicrographs of Fractured Surfaces of $LaCrO_3$-Based Electrodes to be Used in the U-02 Test

The final attachment selection for U-02 Phase III (based on results of Proof Test No. 2) consists of an active metal braze (TiCuSil*) joining the lanthanum chromite to a compliant nickel mesh+ brazed to the copper cooling block. Past experience indicates that with TiCuSil, careful control of brazing conditions is necessary to achieve satisfactory joints. Earlier work at brazing temperatures of 850°C showed that TiCuSil reduced lanthanum chromite to form lanthanum oxide and resulted in a weakening of the joint with time (Reference 3).

A closer look at brazing times and temperatures was undertaken. Three mil thick TiCuSil foil was sandwiched between 2 pieces of lanthanum chromite and held at temperatures between 830 and 850°C for 30 seconds and 2 minutes. Photomicrographs of the results of these tests are shown in Figure 15. A 30 second hold at 830°C shows a titanium core in the center indicative of incomplete melting. A 2 minute hold at 850°C shows destruction of lanthanum chromite at the interface. These results suggest a hold time of several minutes between 835 and 840°C would be desirable for production brazing.

Microscopic examination of the U-02 electrode design reveals that TiCuSil is present only in area where the nickel mesh is in close proximity to the lanthanum chromite. Areas where metal fibers are far apart are free from any measurable amount of TiCuSil on the lanthanum chromite surface. A typical example of this is shown in Figure 16.

An ion microprobe trace across the TiCuSil brazed joint between nickel mesh and lanthanum chromite shows no diffusion of metal ions across this joint, but does show an abnormally high titanium concentration in the brazing alloy at the lanthanum chromite surface. A trace for oxygen shows that it diffuses into the brazing alloy where it probably unites with titanium to form a bond. Excessive diffusion of oxygen during the vacuum or inert atmosphere brazing cycle causes destructive reduction of lanthanum chromite above the bond line.

---

*Western Gold and Plantinum Company.

+Brunswick Corporation, Technetics Division.

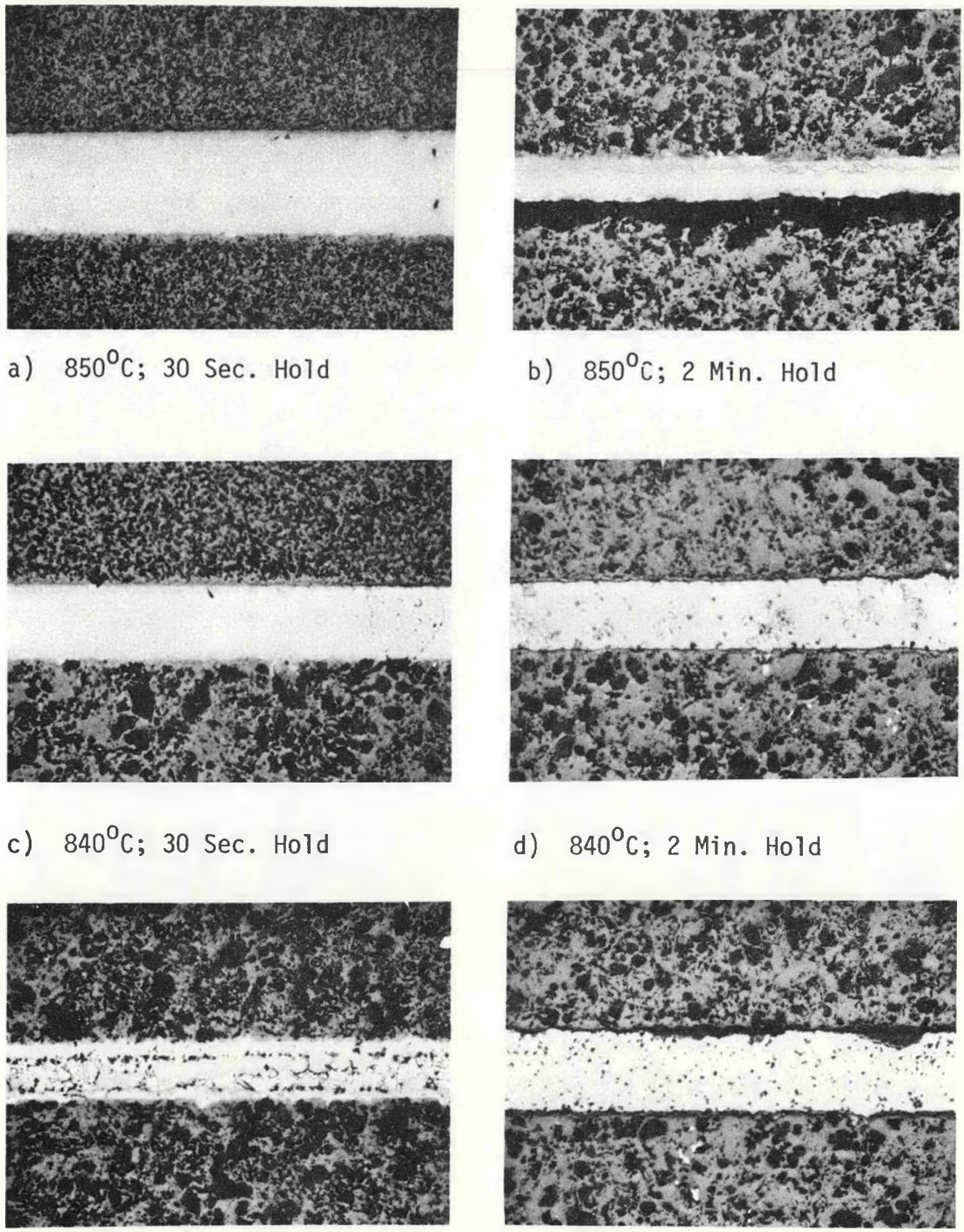

a) 850°C; 30 Sec. Hold

b) 850°C; 2 Min. Hold

c) 840°C; 30 Sec. Hold

d) 840°C; 2 Min. Hold

e) 830°C; 30 Sec. Hold

f) 830°C; 2 Min. Hold

Figure 15. Lanthanum Chromite/TiCuSil Braze Cycles (320X)

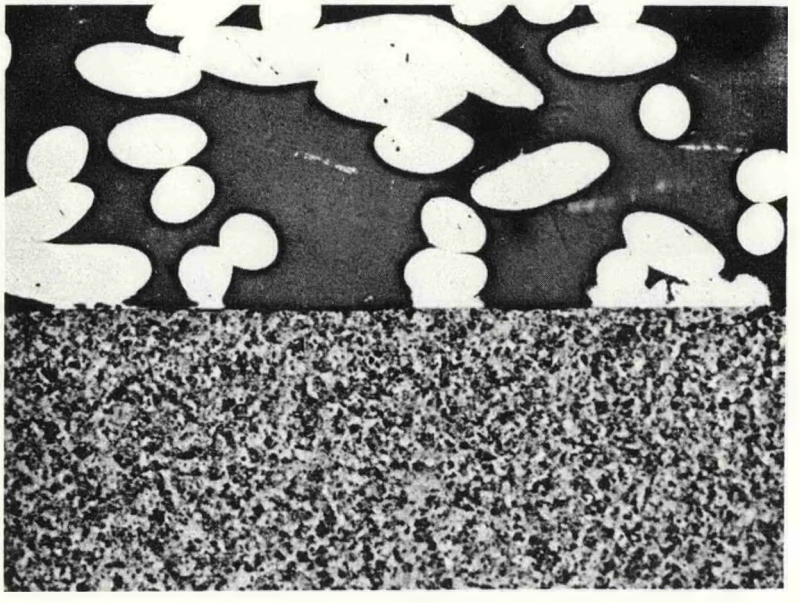

Figure 16. TiCuSil Bond Between Nickel-205 Brunsbond™ and Lanthanum Chromite (50X)

In investigating various pretreatments of the lanthanum chromite surface it was found that a 500-1000 Angstrom film of sputtered gold improved the appearance of the brazed joint. The gold film apparently reduces the activities of titanium and oxygen and permits bond formation without the destructive reduction of lanthanum chromite. Figure 17 shows the joints obtained with a sputtered gold film present. Compare these joints to those in Figure 15 for similar brazing conditions.

Samples of lanthanum chromite brazed to nickel mesh (with and without a sputtered gold film) were satisfactorily tested under a load of 1.5 amps/cm^2 with and without potassium carbonate in a furnace at 500°C for 100 hours to qualify both fabrication techniques for inclusion in the U-02 module.

5.2.1.4 Electrode System Characterization

The electrical resistivity of lanthanum chromite type electrodes with a number of different leadout attachments was measured as a function of temperature. This area was investigated because measurements made during WESTF runs 37 and 38 indicated that many of the $LaCrO_3$ electrodes employed in these tests, had significantly higher joule losses than would be expected from available data on the resistivity of these materials as a function of temperature. In order to understand the causes for the discrepancy, tests were conducted on special two terminal $LaCrO_3$ samples in which D.C. voltages were applied and the currents through the samples and their surface temperatures monitored. Some of the tests were conducted in the self-heating mode, i.e. the sample was brought to the desired temperature by joule heating. In other tests, external heating was also employed.

Typical data obtained in these tests are plotted in Figures 18 and 19. The curve of Figure 18 refers to sample L, a $La_{.95}Mg_{.05}CrO_3$/30 w/o ZrO_2 composite. The cross sectional area for passing current was 2.1 cm^2; the thickness of the sample was 1.0 cm. The impressed voltage was applied between 2 copper strips mounted on opposing surfaces of the rectangular sample. A thin layer of a silver laden epoxy adhesive was used to bond th electrical contacts to the sample. The resistivity of the sample, as calculated from the data of Figure 18, is plotted in Figure 20 as a function of temperature.

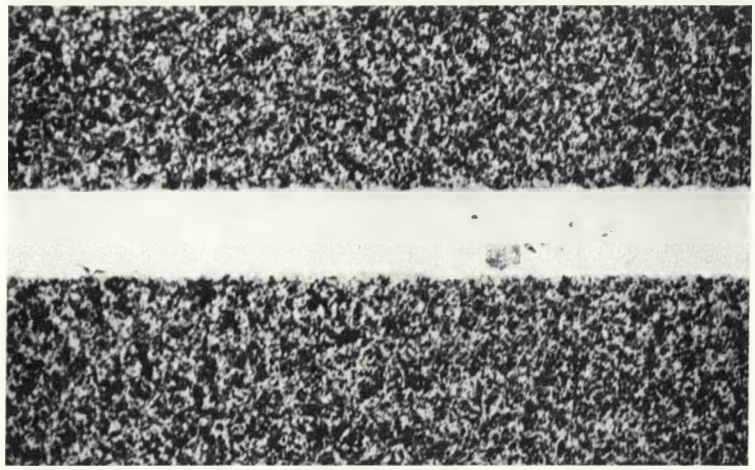

a) 860°C; 2 Min. Hold

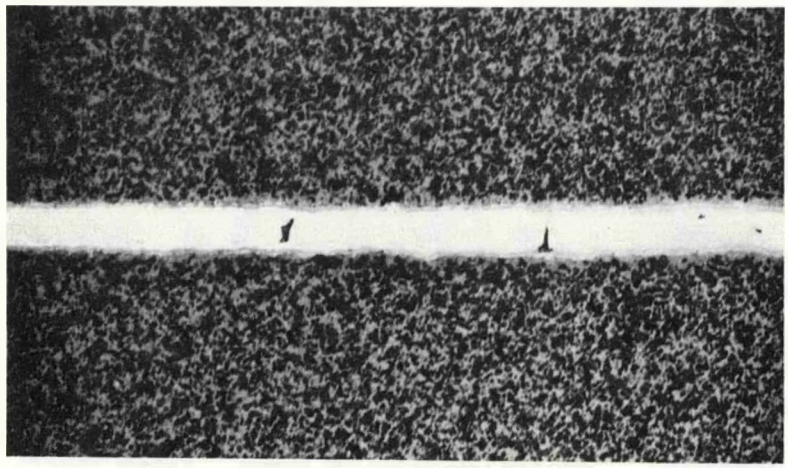

b) 850°C; 2 Min. Hold

Figure 17. TiCuSil Brazing of Lanthanum Chromite Pre-Sputtered with a 500 Angstrom Gold Film

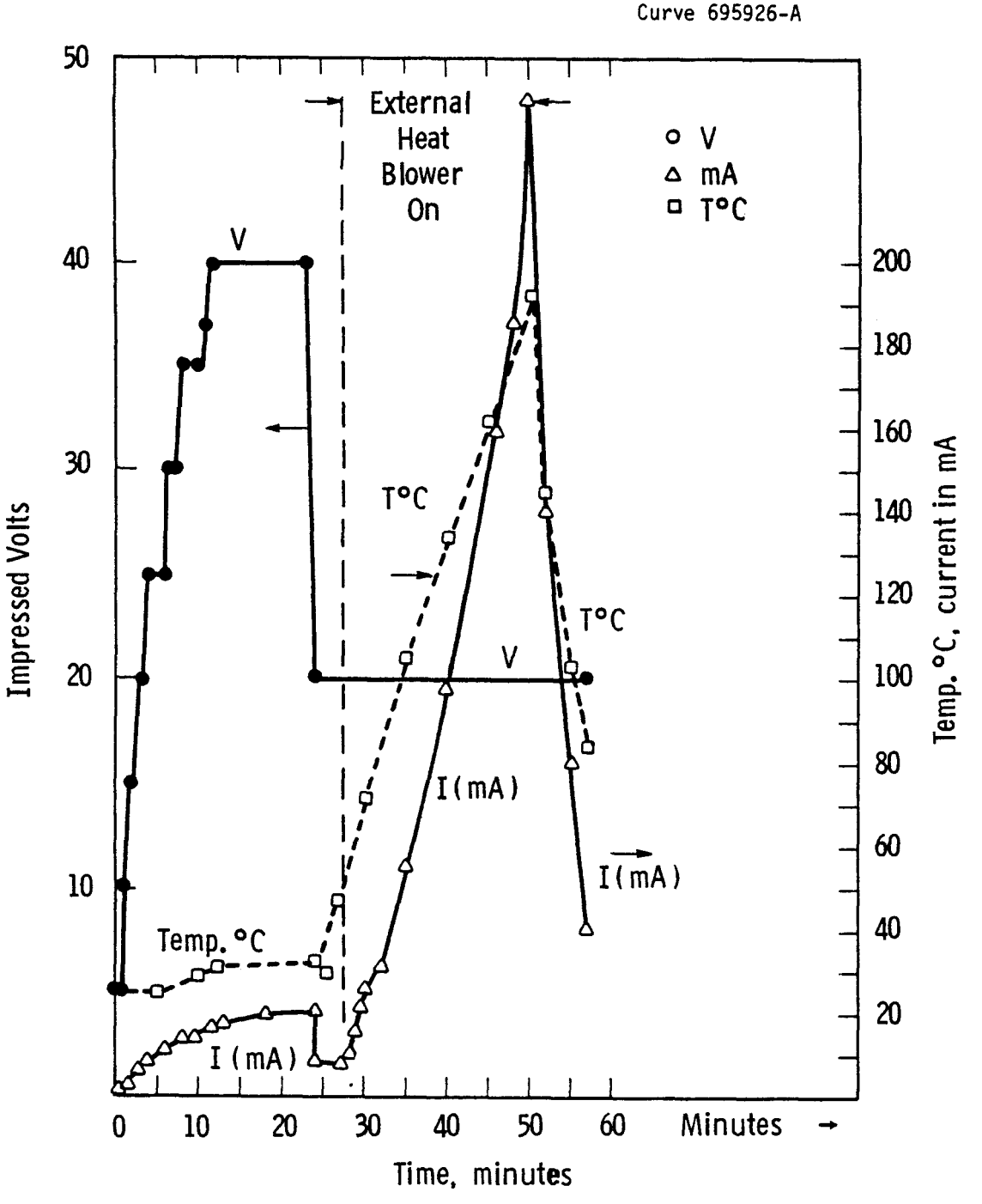

Figure 18. Applied Volts, Current, and Surface Temperature Versus Time for $LaCrO_3$ Composite with 30% ZrO_2, Sputtered Ni Contacts, Sample L

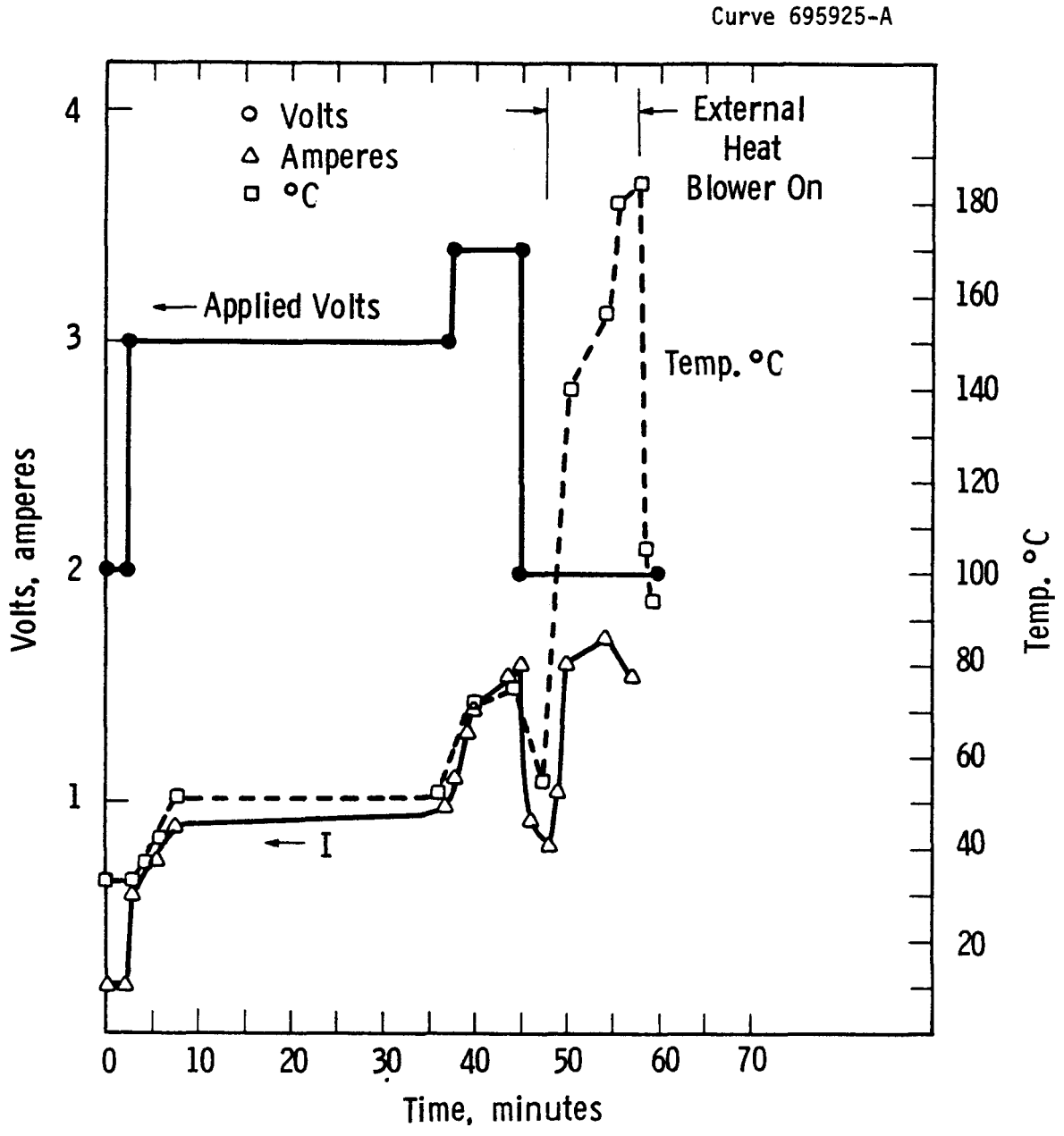

Figure 19. Applied Volts, Resulting Current, and Temperature Versus Time for $LaCrO_3$ with Ag Paste 4400 Contact, Sample N, 700°C Firing

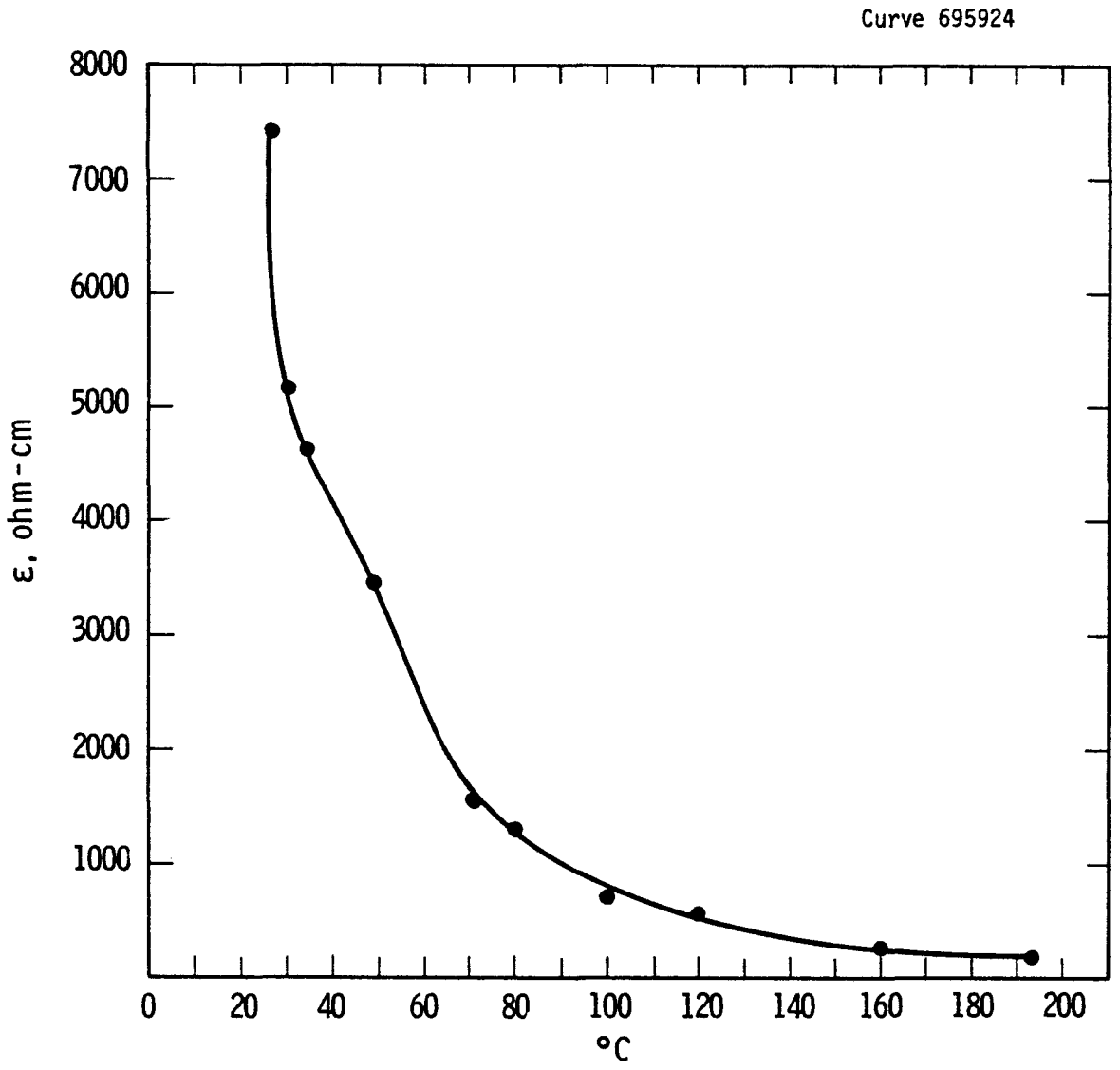

Figure 20. Resistivity in Ohm-Cms as Function of Temperature, Sample L, $LaCrO_3$ Composite with 30% ZrO_2, Sputtered Ni Contacts

From these data it is evident that if sample L operated at $1A/cm^2$ in an MHD channel its joule losses would be high. Even at 190^oC, the maximum current the sample would pass with an impressed voltage of 20 volts was less than 100 mA/cm^2.

If an electrode of sample L were thermally joined to a water-cooled copper back plate, the temperature of the contact under normal MHD service conditions would be of the order of 125^oC to 150^oC. At these temperatures the electrical resistivity of the material was approximately 350 ohm-cm. Thus, a 2 mm thick section adjacent to the contact plane of a one A/cm^2 loading would be subject to about a 70 volt drop and 70 watts power dissipation if operated in this temperature region. In practice the high voltage dissipation would increase the temperature of the material and decrease the dissipated voltage. However, an excessive wattage would still be expected in the region adjacent to the water cooled back plate.

The material and electrical contacts used in obtaining the data of Figure 19 constitutes a significant improvement over the design of L, the previous sample. This sample, N, consisted of a $La_{.95}Mg_{.05}CrO_3$ electrode which was joined to the copper terminals with a Ag paste that was fired at 710^oC, had a cross-sectional area of 2.15 cm^2, and was 1.0 cm thick.

Figure 19 shows that a current of 1.7 amperes can be transmitted through sample N with only 2 volts impressed between the terminals to give less than 4 watts dissipation at 180^oC. Joule losses in sample N should be low in actual MHD service for a one A/cm^2 loading even at temperatures as low as 125^oC.

Figure 21 gives the resistivity values for this sample as a function of temperature. The slope of the resistivity curve for "N" differs from "L" which probably indicates that the mechanism for low and high temperature conductivities also differ.

Curve 695922-A

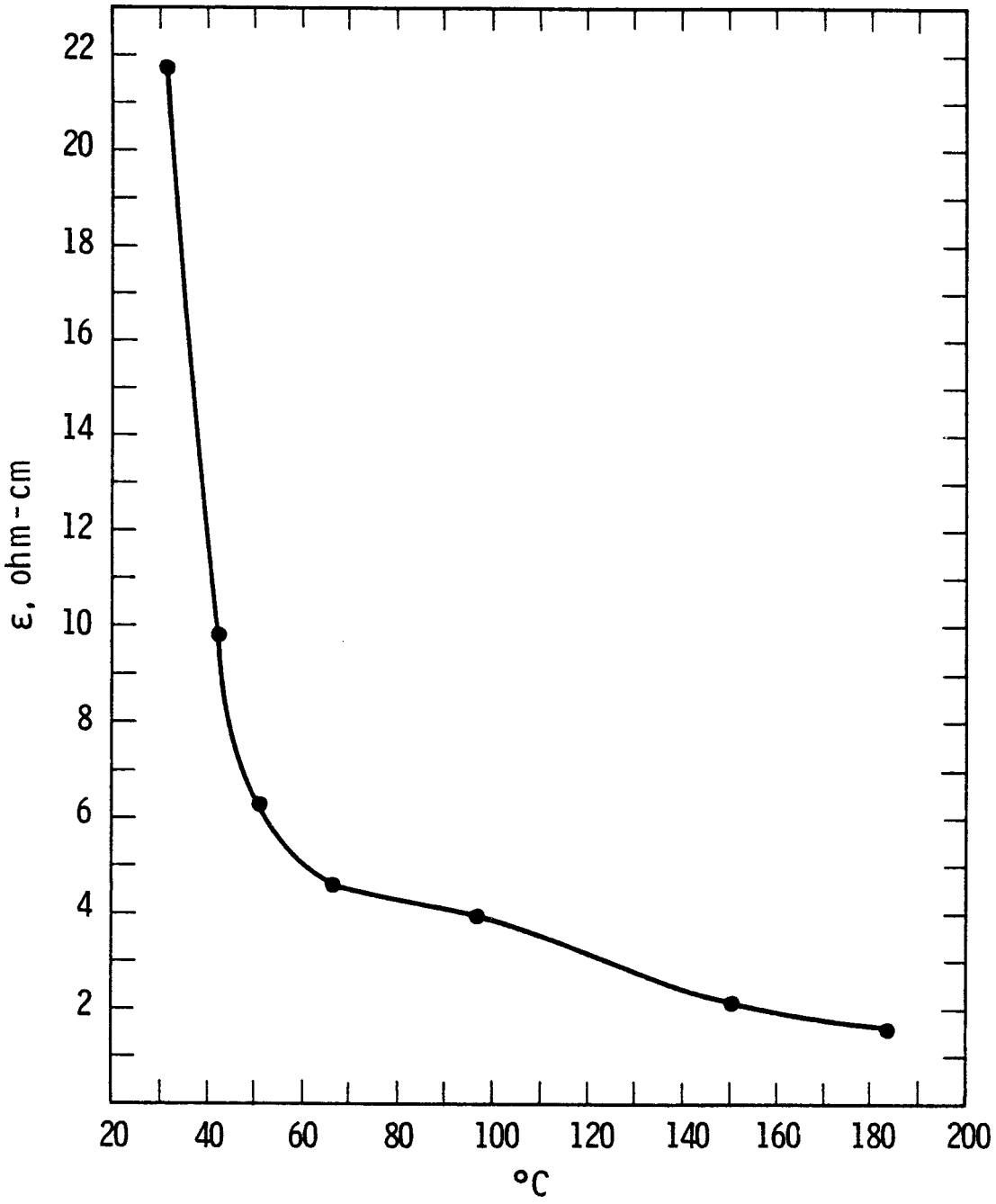

Figure 21. Resistivity in Ohm-Cms as Function of Temperature, Sample N, $LaCrO_3$ with Ag Paste 4400 Contacts, 700°C Firing

In these tests, external heat was applied to both samples to bring them to about 190°C. The same result could have been achieved without using external heat by impressing a higher voltage on the samples. For example, an impressed voltage perhaps of the order of 100 volts or more, would have been required to self-heat "L" to about 200°C.

In a similar test on a 0.5 $La_{.95}Mg_{.05}CrO_3$-0.5$SrZrO_3$ sample a "runaway condition" developed. This occurs when the impressed voltage is high enough to exceed the wattage dissipation capabilities of the material mounted in the test device. As the resistivity of the material drops with increasing temperature, the impressed current rapidly rises, and a thermal runaway occurs which if unchecked could destroy the sample.

Both the $LaCrO_3/SrZrO_3$ and $LaCrO_3/ZrO_2$ composites were found to have resistivities at 170 to 190°C that are higher than the electrically satisfactory $LaCrO_3$ sample "N" referred to previously. A resistivity dependence on voltage was also clearly evident at the beginning of the runs when the impressed voltage was increased under essentially constant temperature conditions.

A series of very instructive tests was conducted on a $La_{.95}Mg_{.05}CrO_3$ sample which was brazed on one side to "BRUNSBOND" Ni mesh*, and joined on the opposite side to a copper terminal with a silver epoxy adhesive. The cross-sectional area of the sample was 1.4 cm^2, and its thickness 2.2 cm. Its room temperature resistivity at the beginning of the test was of the order of 10^6 ohm-cm, a prohibitively high value. After 4 hours of operation at temperatures up to 300°C, the room temperature resistivity of the sample was about 1000 ohm-cm. A second 4 hour run to 217°C was terminated when the Ag epoxy terminal (weakened because of operation above recommended use temperatures) stressed and came apart. However, the room temperature resistivity had decreased to about 700 ohm-cm during this run.

---

*Brunswick Corporation, Technetics Division.

Because of a crack which occurred when the sample was being refitted with the lost terminal, the sample thickness was decreased to 1.25 cm. This sample was then loaded at 1.8 amperes corresponding to a loading of 1.3 A/cm^2, for 71 hours at a temperature of 160^oC to 170^oC. At the end of the test, the sample was still in good condition. The resistance at room temperature was now down to 170 ohms, compared to the initial room temperature resistance of over one megohm. During the course of the test the sample changed from an unsatisfactory to an electrically satisfactory condition.

Clearly, the change in electrical resistivity was significant and called for an investigation to determine its causes, and to devise means for obtaining samples for future channel tests with comparably low electrical resistances. About 25 different test runs were conducted during this investigation.

Initially it was thought that contact resistances between the terminals and the ceramic was the problem. This thesis was supported when sputtered gold layers and in some cases ion plated Ni layers were employed in fabricating the contacts, and lower resistance drops were obtained across the samples. However, other samples made in the same manner had high resistances.

Investigations with an ohmeter probe of the external faces of $LaCrO_3$ type samples having low and high electrical resistances between opposing terminals revealed that samples having high electrical resistance readings during the test runs were always associated with high ohmeter probe resistance readings on the different exposed surfaces of the ceramic. In addition, several $LaCrO_3$ type ceramics were observed to have markedly different surface resistivities from face to face. Before and after ohmmeter readings on a number of $LaCrO_3$ samples that were air-fired for several hours at 1600^oC revealed a drastic drop in the electrical resistance on the various surfaces and across the volume of the sample. However, when the samples were cut open it developed that the low resistances were observed only in a one mm surface layer.

According to these results, electrical conduction during operation may be confined to local surface regions. This thesis was supported in a test run on sample "X", a $La_{.95}Mg_{.05}CrO_3$/30 w/o ZrO_2 composite that was not high temperature air-fired. The sample, 1 cm^2 in area and 2 cm high, was particularly resistive, and it was necessary to impress 600 volts to obtain a 19 mA current at a temperature of 185°C.

During the test, an arc was observed at one of the corners and a ceramic piece chipped off in this region. At the same time a substantial decrease in load current was observed. It is believed that the current during the test was roughly confined to one relatively conductive small region in a corner of the sample. After this corner was overheated and cracked off, conduction substantially decreased.

Other tests confirmed the improvements achieved by the 1600°C air firing of different $LaCrO_3$ type electrodes. In order to determine the effect of subjecting an air-fired sample to the vacuum environment used in the TiCuSil brazing operation, several air-fired samples were brazed and the resistivity measured. Vacuum brazing increased the surface resistivity of the different exposed faces by about a factor of 2. However, the resistivity of the $LaCrO_3$ still appeared to be satisfactory.

From the tests conducted it appeared clear that the electrical quality of different $LaCrO_3$ electrodes can be evaluated by simple ohmmeter tests. It was also clear that the firing at 1600°C improved the electrical quality of the samples. However, it was not yet evident that the $LaCrO_3/ZrO_2$ composites would perform well under operating conditions. Accordingly several tests were set-up to determine what the back-face temperature would have to be and to evaluate how such assemblies would stand up at the required temperatures as a function of time.

A group of $LaCrO_3$/30 w/o ZrO_2 composite samples, "R1" through "R4", were prepared by TiCuSil brazing "BRUNSBOND" nickel mesh terminals to opposite

faces of each of the samples. The samples were identical except that "R1" and "R4" had sputtered gold intermediate contacts at the brazed joints. These attachments, both with and without the gold film, were selected for the U-02 Phase III electrodes. In testing "R1" and "R2" it was found necessary to bring the samples to the 250°C to 350°C temperature range in order to be able to impress 1 ampere through them in the absence of an external heating system. Both of the samples dissipated between 10 and 15 watts in order to maintain the equilibrium temperatures. Both samples were in satisfactory condition after the tests. As with the $LaCrO_3$ samples, the electrical conductivities of both samples improved with continued operation. At the conclusion of the tests the warm temperature resistivities of the samples were less than 10 ohm-cm.

At the beginning or constant temperature portion of the test, both "R1" and "R2" experienced a significant reduction in resistance with increasing voltage. Thus, it was evident that the $La_{.95}Mg_{.05}CrO_3$/30 w/o ZrO_2 composite responded favorably to the same kind of electrical "seasoning" responsible for the improvement of $La_{.95}Mg_{.05}CrO_3$ itself.

In order to evaluate the ability of the $La_{.95}Mg_{.05}CrO_3$/30 w/o ZrO_2 composite to operate at high temperatures for sustained periods of time, the samples were mounted at room temperature in an air-furnace, with provisions made to impress a load of $2A/cm^2$ through them. The furnace was then brought to 400°C and the currents through the samples gradually increased.

Sample "R2" operated in the furnace at 400°C for an additional 66 hours at a load of $2A/cm^2$ with a dissipation of approximately 4.0 watts. It had been found from similar runs that a dissipation of 3 to 4 watts in a sample would increase the temperature of the sample about 100°C over ambient. Thus a sample temperature of 500°C is estimated for a furnace temperature of 400°C.

Samples "R1" and "R2" were then subjected to an additional test at a 400°C furnace temperature. The voltage required to impress $2A/cm^2$ through "R2" progressively decreased to 4.0 volts. This sample was in good condition after the additional 41 hours of operation.

Sample R1 failed after 18-1/2 hours of power operation. The voltage requirement impress 2A/cm^2 through the sample progressively increased by a small amount during the test to 6.0 volts. Failure was indicated by an open circuit. Examination of the sample after the test revealed the failure was due to progressive oxidation of the weld between the connecting .020" Ni lead wire and the Ni-mesh.

In summary, operation of R1 included 65 hours at 2.0 amp/cm^2 under self heating conditions at temperatures between 300 and 375^{o}C, and 18-1/2 hours of operation at 500^{o}C in the furnace test at the same loading density.

Sample R2 operated for 18 hours at 2.0 A/cm^2 under self-heating conditions and 110 hours in the furnace at 500^{o}C. Resistivity data as a function of temperature as taken in the furnace tests is plotted in Figure 22 for both samples. Resistivity tests on the two "seasoned" samples in Figure 22 have a single linear slope. R1, the sample with a sputtered contact layer at the terminals had a lower resistivity than R2 without a gold sputtered contact layer in the self heater tests.

Self-heating and furnace tests were also conducted on "R3" and "R4", but these samples were presoaked in a concentrated K_2CO_3 solution. "R4", the sample with a sputtered gold film, again showed a lower contact resistance in the self heating tests. A hot spot, .06 x .03 was observed at one of the interfaces between the ceramic and the mesh that may have been due to a local high conductivity area near the contact that carried a disproportionate share of the load.

Figures 23 and 24 show the resistivities of both sample as a function of temperature as observed in the self-heating and furnace tests, respectively. "R4" ran for 95 hours at 2A/cm^2 at a furnace temperature of 375^{o}C (estimated ceramic temperature of 475^{o}C). Its power dissipation decreased from 5.8 to 4.8 watts during the tests. The sample was in good condition at the end of the test.

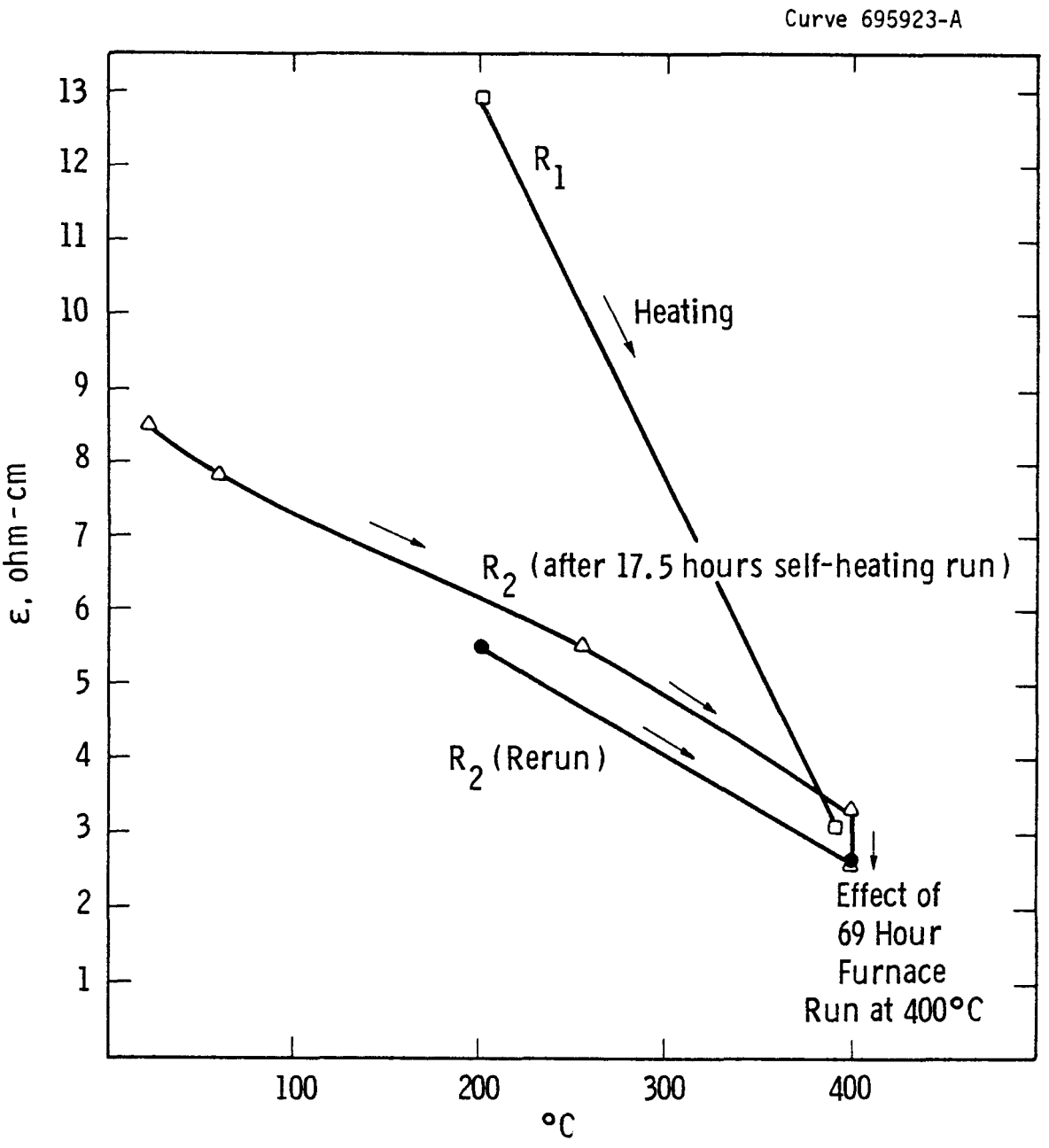

Figure 22. Resistivity of $La_{.95}Mg_{.05}CrO_3$ + 30% ZrO_2 Composites as Function of Furnace Temperature. R2 has Sputtered Layers of Gold at Contact to Terminals.

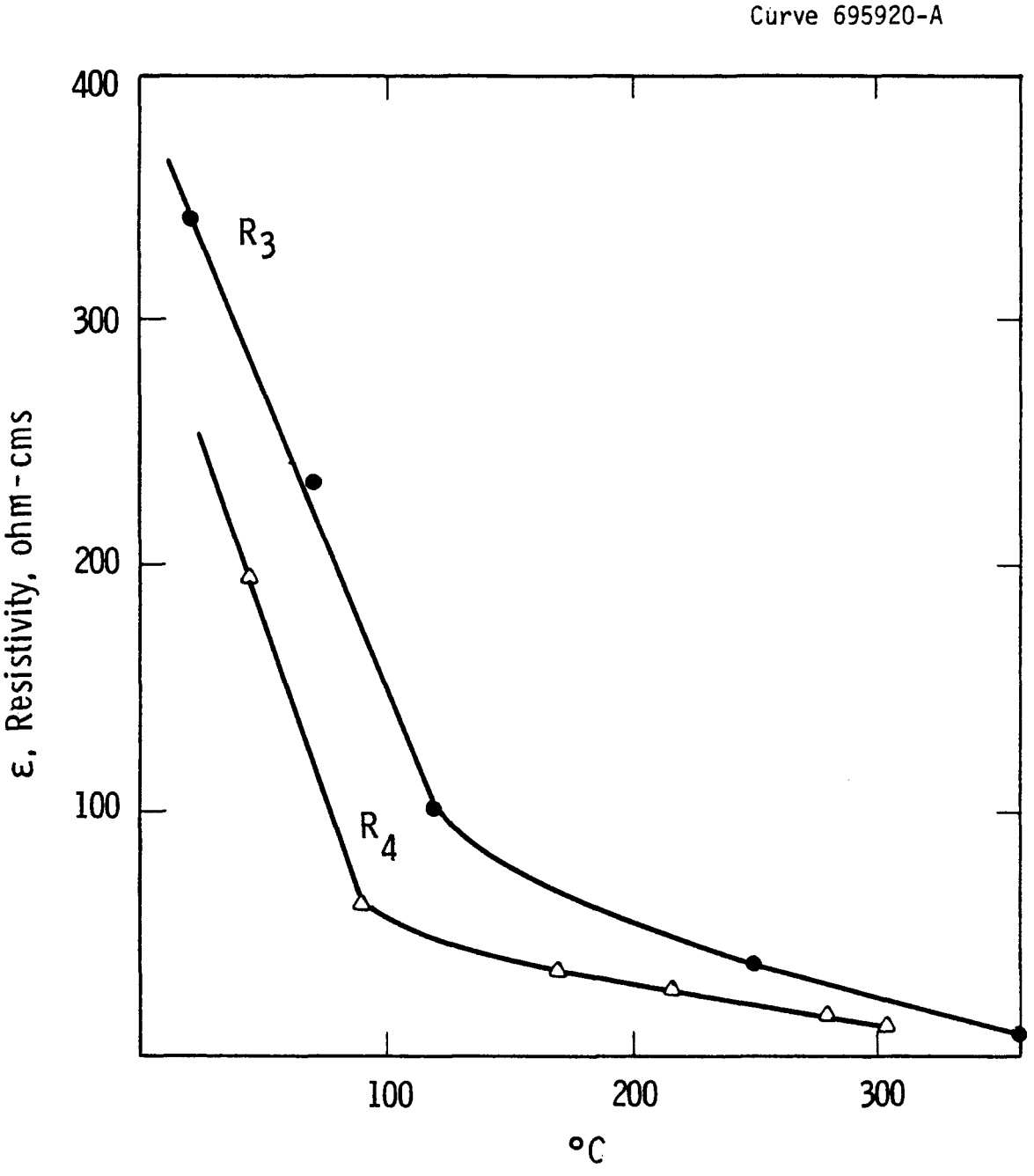

Figure 23. Resistivity of K_2CO_3 Soaked $La_{.95}Mg_{.05}CrO_3$ + 30% ZrO_2 Composites Under Self-Heating Conditions

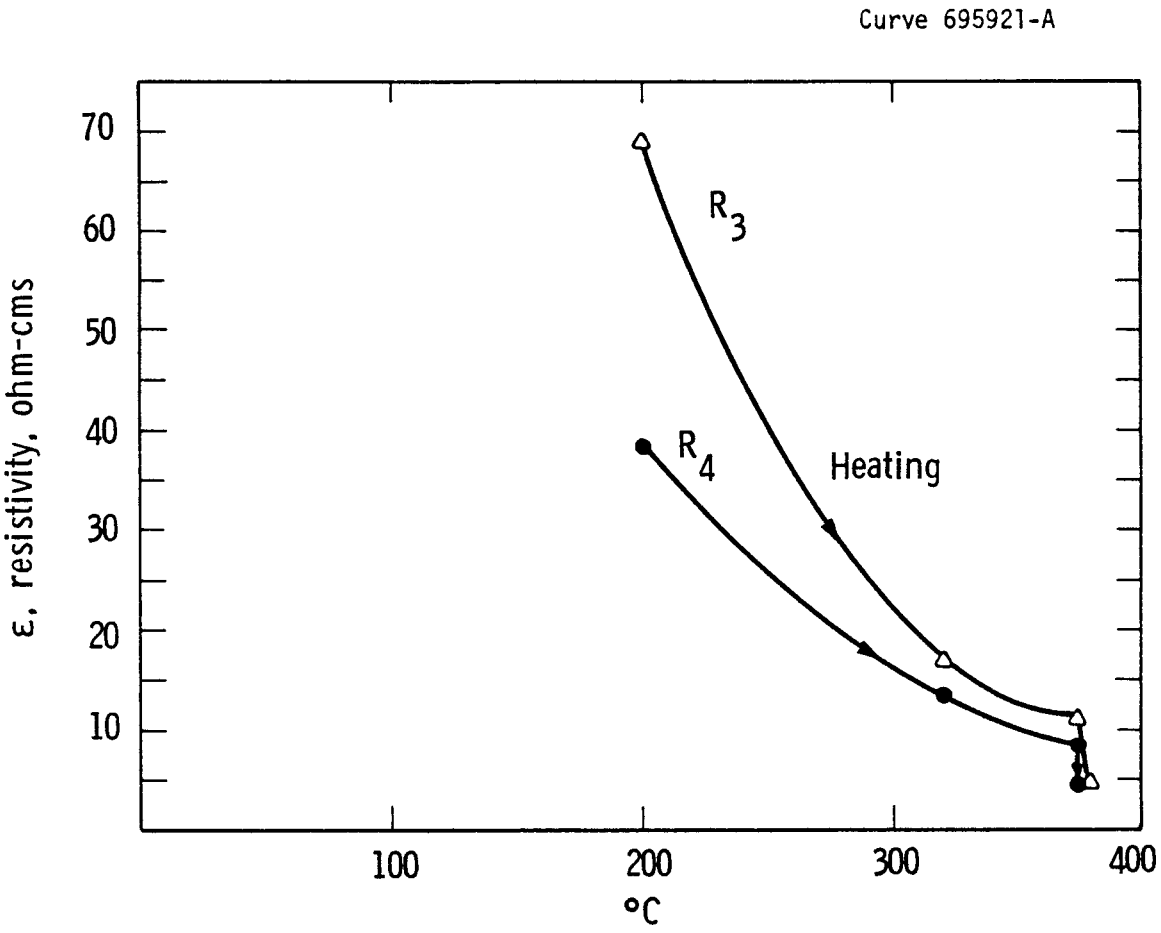

Figure 24. Resistivity of K_2CO_3 Soaked $La_{.95}Mg_{.05}CrO_3$ + 30% ZrO_2 Composites as Function of Temperature with $2A/cm^2$ Load in Furnace

"R3" operated about 91 hours in the furnace tests at $2A/cm^2$. Its power dissipation gradually increased during the test, due to an increasing requirement for voltage. Failure occurred after 91 hours when one of the Ni connecting wires came off the mesh to give in open circuit. The power dissipation in the R3 sample, which did not have the gold sputtered contacts, was 6.6 watts at the end of the test.

From the tests of samples R1, R2 and R3 and R4 it seems clear that the K_2CO_3 exercised minimal effect on the capabilities of the ceramic to stand up under severe conditions. Some of the K_2CO_3 material oozed out of the interior and deposited on the surface of the ceramic during operation. However, an examination in which R3 and R4 were sectioned indicated that a substantial fraction of the K_2O_3 penetrated and remained inside the interior of the mesh. During the one month storage period at room temperature, the TiCuSil junction between the mesh and the ceramic had weakened to the extent that the mesh sections fell off. It is surmised that the soldered joints performed adequately during the test, but that hydrolysis of the seed after the samples were removed from the furnace was responsible for the later failure of the seals. It is possible that the oxidation and erosion of the fine wires of the Ni mesh during operation in the furance contributed to the failure.

Thus, these investigations demonstrated that the electrical quality of the $LaCrO_3$ is improved by high temperature oxidation. One of the principal consequences of the high temperature "seasoning" of the electrodes is to gradually decrease the low temperature resistivity of the samples. The higher temperature intrinsic resistivity is much less effected by the seasoning schedule. The use of a sputtered gold film to lower the contact resistance was also observed. Finally, an electrical "proof test" demonstrated the survivability of the attachments selected for the U-02 Phase III module at high contact temperatures in the presence of seed.

5.2.2 U-02 Proof Tests

The U-02 Proof Tests were structured to allow evaluation of:

- General Resistance of electrode systems to high temperature and corrosive conditions,
- electrode system thermal design, interface temperatures and heat flux and
- electrical performance of electrodes and interelectrode insulators.

Table 8 presents a brief comparison of pertinent facility characteristics while Figure 25 shows the electrode/test section configuration for U-02 and WESTF.

The proof tests were conducted in accordance with a Work Plan which included the general objectives, operating conditions, test philosophy and test procedure. This Work Plan was approved by the non-Westinghouse electrode suppliers. Test Monitors, selected by DOE-MHD, participated in and monitored the conduct of the proof tests.

During this quarter the following significant activities for the U-02 Proof Test Series were completed:

- Conduct of Proof Test 3, including preparation of the Express Report for this test
- Post-test evaluation of facility operation and electrode thermal and electrical performance for Proof Test 3
- Comprehensive materials characterization for Proof Test 1, 2, and 3
- Selection of electrode systems for U-02 Phase III Module.

Results of these activities are presented in the following sections. Information on previous Proof Tests, electrode thermal/structural design, and the fabrication and assembly of Proof Test 3 is given in Reference 1.

5.2.2.1 Test Operations

Proof Test 3 Operational Summary (WESTF 39)

A test of four candidate electrode systems (described in Section 5.2.2.2 of Reference 1) was carried out at the Westinghouse Electrode Systems Test Facility on January 4-5, 1978. A schematic diagram of the electrode walls is shown in Figure 26. These

TABLE 8

COMPARISON OF U-02 AND WESTF

Parameter	U-02	WESTF
Fuel	Natural Gas	Toluene
Plasma Temperature, °K	2500-2600	2500-2600
Plasma Velocity, m/sec	400-500	∿450
Mass Flow Rate, kg/sec	∿0.7	∿0.1
Static Pressure, atm	∿0.9	∿1.05
Channel Dimensions, cm (w x h)	26.0 x 6.0	2.5 x 5.0
Number Electrode Pairs	36	12
Current Density, A/cm^2	0 to 1.25	1.25
Magnetic Field, T	1.5 - 1.7	None
Test Duration, hours	∿100	∿20

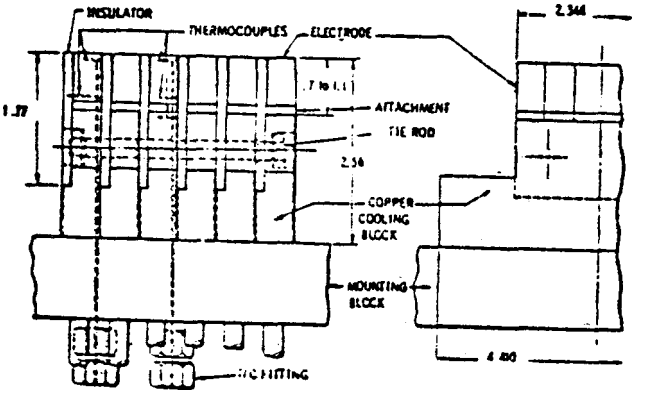

a) U-02 Electrode Assembly

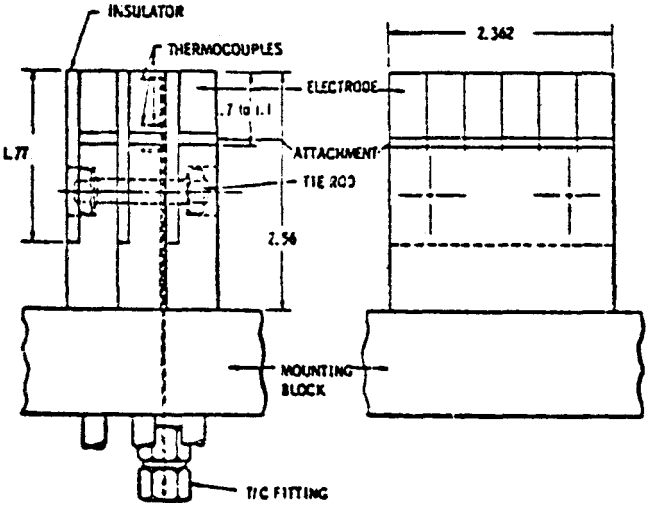

b) WESTF Electrode Assembly

Figure 25. U-02 and WESTF Electrode Assembly

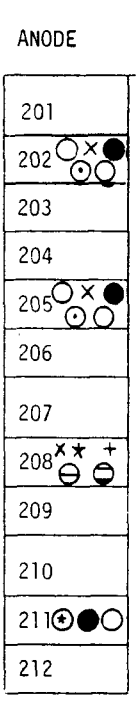

ELECTRODE MATERIAL	ATTACHMENT	INTERELECTRODE INSULATOR
Layered Al_2O_3 doped	Ag Epoxy	Monolithic
$LaCrO_3$ - Westinghouse	Au Film	MgO (Norton
Hot Pressed	(Back Face)	(one side)
$.5LaCrO_3$ - $.5SrZrO_3$	Ag Epoxy	Monolithic
A-T Research	PT Film	Spinel (Trans-
Sintered	(Back Face)	tech) (one side)
$LaCrO_3$	Flexbed	Monolithic
General Electric		Spinel
Sintered		(both sides)
MAFF-31/Hercynite	Spray Bond	S-71 Spinel (both sides)
APS Materials	To ION -	APS Materials
Plasma Sprayed	Plated Ni	Plasma sprayed

THERMOCOUPLES

Symbol	Location	Designation	Type	Sheathed	Bare Wire
⊗	Electrode (Hot) Center	T_1	B	X	
X	" " "	T_1'	B		X
✶	Electrode (Hot) End	T_1''	B		X
⊙	Electrode (Hot) Center	T_1'''	S	X	
●	Electrode Cold Center	T_2	K	X	
+	Electrode Cold Center	T_2'	B		X
⊙	Insulator (Cold) Center	T_3	K	X	
○	Copper (Block) Center	T_4	K	X	
⊖	Copper (Block) Center	T_4'	K		X
⊖	Copper (Block) End	T_5	K		X

Figure 26. Electrode Wall Schematic-Proof Test 3 (WESTF Test 39)

12 pair of electrodes ran for 21.8 hours with electrode surface temperatures between 1600 and 1785°C. External power supplies produced a flow of current through all but two electrode pairs at a current density of 1.0 A/cm^2.

Elapsed time from ignition until the combustor was shut off totaled 33 hours 3 minutes; of this time, 9 hours 46 minutes, 21 hours 51 minutes and 1 hour 26 minutes were heating the test section, test conditions and cooling the test section, respectively. A brief chronology of this test is shown below. The flow rates of fuel, air and oxygen during test are shown in Figure 27.

CHRONOLOGY OF PROOF TEST 2

		Time	Date	Lapse Time
1.	Startup	0600	1-4-78	0 hrs
2.	Preheater Ignition	0630	1-4-78	0.4
3.	Combustor Ignition	0904	1-4-78	3.0
4.	1850°C Calibration Hold	1100	1-4-78	4.9
5.	1600°C Electrode Surface Hold	1330	1-4-78	7.4
6.	1700°C Electrode Surface Hold Without Seed or Current	1500	1-4-78	8.9
7.	Start of Life Test with Seed and Current	1550	1-4-78	9.8
8	Mid-Test Electrical Tests	0233	1-5-78	20.5
9	Final Electrical Tests	1150	1-5-78	29.8
10.	Seed Off	1341	1-5-78	31.6
11.	Start of Cooldown	1341	1-5-78	31.6
12.	Fuel Off	1455	1-5-78	32.8
13.	Preheater Cooldown	1507	1-5-78	33.0

Average values for the various parameters during the life tests were:

Mass Flow	73.2 g/s
Pressure in mixing chamber	1.22 atm
Oxidant preheat temperature	368°C
Oxygen temperature	23°C
Oxygen in oxidant	40.3% wt

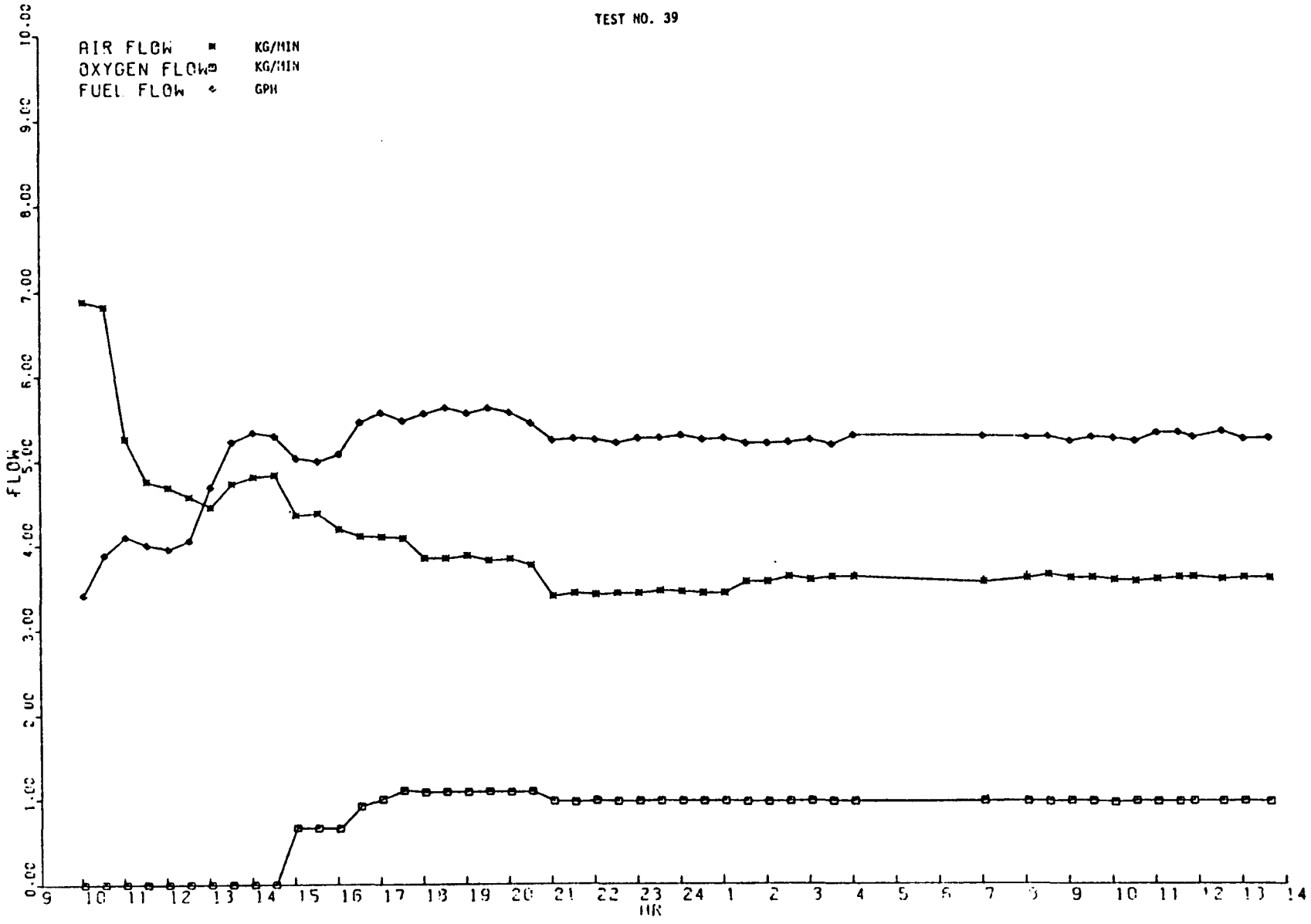

Figure 27. Proof Test 3 - Mass Flow Rates (WESTF Test 39)

Seed solution	50% wt K_2 CO_3/50% wt H_2O
Potassium concentration	1.12% wt
Fuel	Toulene
Stoichiometry	1.4 S.O.
Plasma temperature	2450°K
Plasma conductivity	4.6 mhos/m
Plasma velocity	355 m/sec

In order to simulate U-02 conditions, the objective in this test was to operate all electrodes at approximately 1700°C (surface) with heat fluxes in the range(s) anticipated in the U-02 Phase III test, and with the plasma having a conductivity greater than 3 mhos/m. The current carrying capacity of each material group was to be demonstrated by impressing a sufficient voltage (bias) across the electrode material and plasma resistance such that at design point a density of 1.25A/cm^2 would be sustained.

Proof Test 3 Post-Test Visual Examination

After completion of the cool-down phase of the proof test, the test section was removed from WESTF and moved into the laboratory for disassembly of the test section. The top insulating wall was removed from the test section and it was noted that several electrode groups were severely damaged. Also, the potassium attack, erosion and corrosion appeared to be greater on the anode wall than on the cathode. (Figure 28). The top insulating wall was also severely damaged due both to the attack of potassium on the Mgo brick and the hydration of entrapped potassium seed.

A summary of post-test visual observations of individual electrode groups are given below. Electrode identities can be established by referring to Figure 26.

For the anode wall

- The most severely eroded-corroded anodes are the 204-206 ($SrZrO_3$-$LaCrO_3$) electrodes. The severe corrosion-errosion resulted in enhanced damage to electrodes 203 and 207. The 204 anode is deeply eroded. The electrode erosion on 204-206 is generally more severe than the adjacent insulators leaving some protrusion of the MgO insulators.

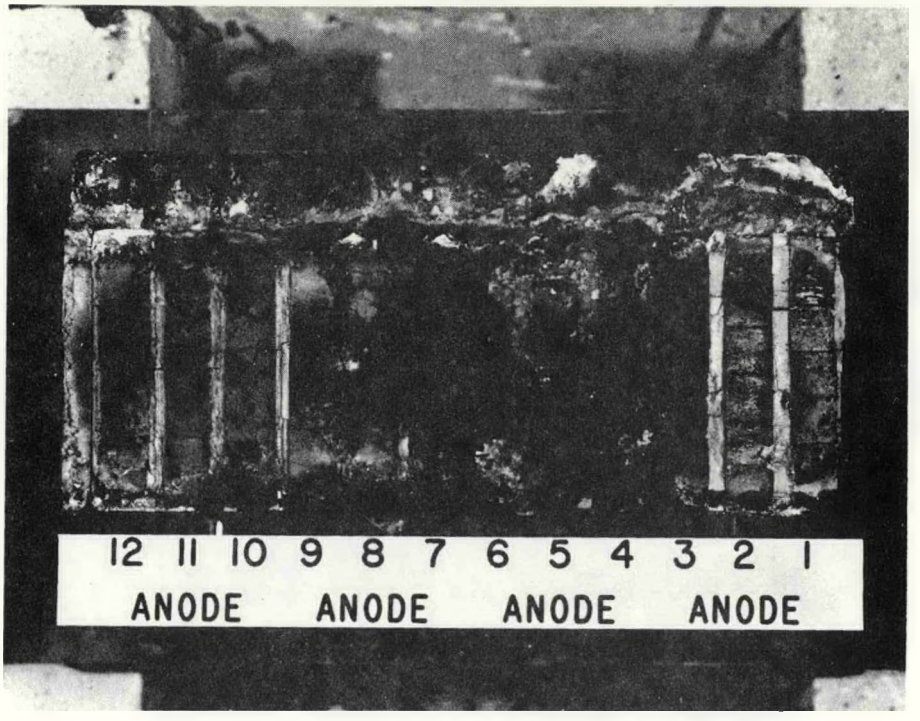

a. Top View

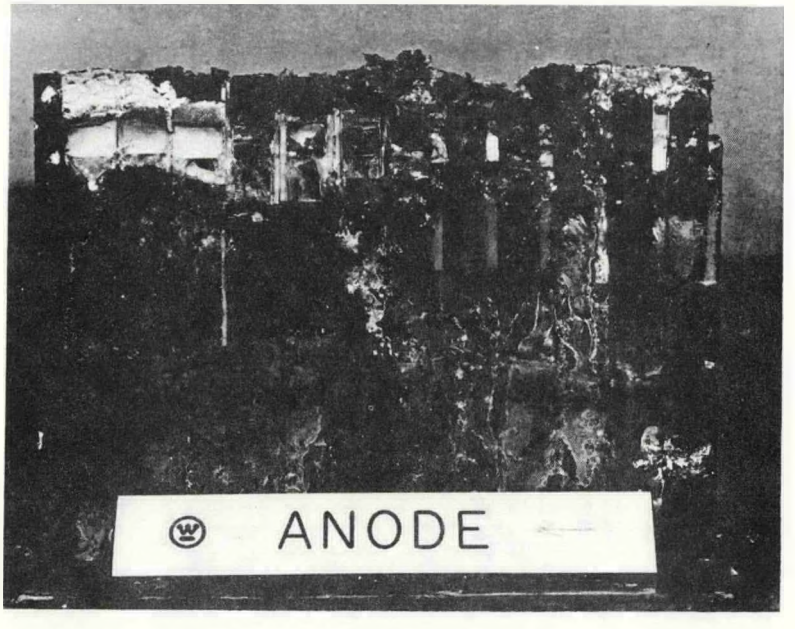

b. Side View

Figure 28a. Anode Wall-Proof Test 3 (WESTF Test 39), Post Test

a. Top View

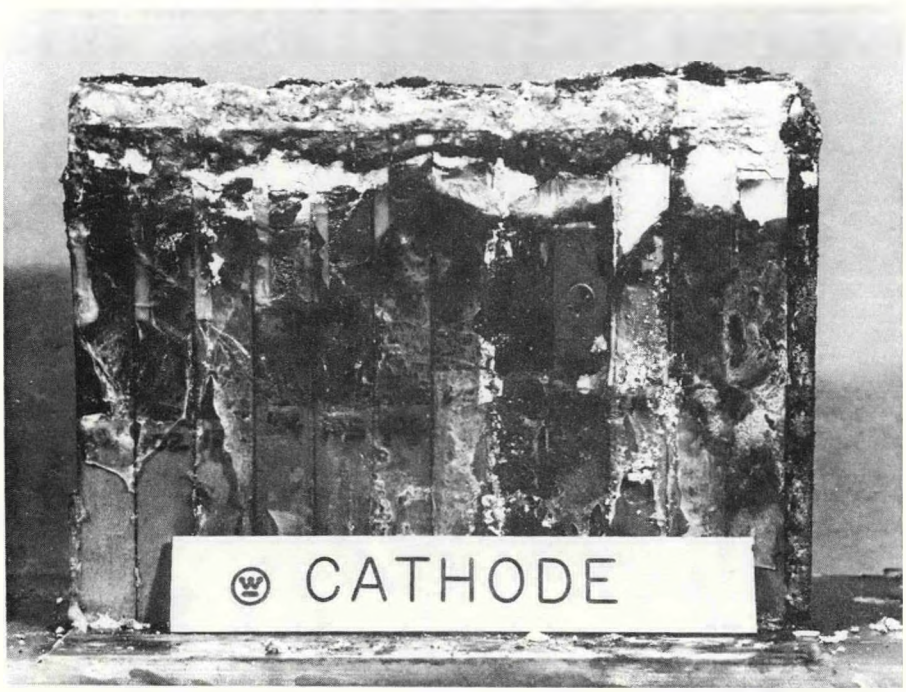

b. Side View

Figure 28b. Cathode Wall-Proof Test 3 (WESTF Test 39), Post-Test

- The next most severely damaged electrodes were 207-209. In this case the insulators have eroded even further below the surface of the electrode. The insulators appear to be preferentially attacked.
- Electrode 203 appears to have reacted with 204. Electrodes 201 and 202 remain relatively unchanged and appear the least damaged of all the anodes.
- Electrodes 210-212 are uniformly eroded but not excessively so.

For the cathode wall

- The most severely damaged cathodes were 104-106. As opposed to the anodes, these cathodes were more uniformly eroded.
- The next most severely damaged was electrode 110-112. Part of the damage is due to bloating. The bloating is most severe adjacent to the top insulating wall (which had degraded due to excess potassium attack). The bloating was occurring during examination. The bloated region appears to contain the reddish colored hematite. The MAFF has separated on some of the blocks from the hercynite.
- The third most damaged are electrodes 107-109. Some surface spalling has occurred. The insulators remain intact and are not as severely eroded as the respective anodes. Bloating due to the hydration of lanthanum was found on these cathodes.
- By far the best cathode is 101-103. They are uniformly and slightly eroded.

Subsequently both anode and cathode wall were each cast in epoxy resin. Each module (anode and cathode) was cut through the center in a plane parallel to the plasma flow and perpendicular to the plasma-electrode surface. Sections were distributed to the National Bureau of Standards and to Battelle Pacific Northwest Laboratories for post-test analysis. The results of these analyses, as well as those for Proof Tests 1 and 2, are reported in Section 5.2.2.4.

5.2.2.2 Experiment Analysis

Results of the post-test experiment analysis are presented in the following sections for Proof Test 3. Subsections are provided for thermal performance and electrical performance. The materials performance for Proof Test 3 is included in a comprehensive section covering the performance of materials in all three Proof Tests (WESTF tests 37 through 39).

Detailed thermal analyses were completed for each electrode system under Westinghouse design cognizance to size all but the General Electric electrodes in Proof Test 3. Electrode thermal design is discussed in detail in References 1 and 9.

Facility operating conditions were defined through predictions using a one-dimensional duct analysis code. This code can be used to identify mass flow and plasma temperature based on a specified surface temperature and heat flux for each electrode.

Thermal Performance - Proof Test 3 (WESTF Test 39)

In establishing final experimental conditions, surface temperatures were calculated based upon a thermal model for each electrode system. Radiographs and dimensional inspections of the final assemblies of each electrode segment containing thermocouples, consideration of individual sensor geometry (including pre-assembly accommodations in the sensor to insure compatible fits with the ceramic) and the thermal models were used to establish the projected electrode surface temperature readings based upon the indicated instrument readings from twelve type B and two type S thermocouples located approximately 3 mm from their respective electrode surfaces.

These analyses were based upon nominal (as determined by a heat balance model for design conditions) operating parameters predicted for the test facility. In addition, these predictions also included an error analysis reflecting possible errors due to thermocouple calibration error, thermocouple bead location, uncertainty in electrode and thermocouple thermal conductivity data and uncertainty in the surface heat transfer coefficient.

This procedure enabled the plotting of graphs of surface temperature (Ts) vs thermocouple reading (T_1 or T_2) for each electrode system design incorporating an error band ranging from (Ts) minimum to (Ts) maximum. Series of such curves were plotted for three distinct sets of test operating parameters scheduled for the normal chronology. These conditions were:

1) 1850°C (combustion gas) system calibration hold.
2) 1600°C electrode surface temperature hold and
3) System design point a 1700°C without and with superimposed current.

With the aid of these sets of data, and curves, personnel monitoring Proof Test III could readily obtain expected surface temperature readings from actual thermocouple readings during the normal chronology of the test. This prediction report was also useful in that it aided in the identification of electrode thermal performance and channel performance operating conditions, thereby providing a continuous guideline and index for the conduct of the test in order to meet the desired objectives.

(A) Test Conditions and Diagnostic Checks

Calculated surface temperatures for several electrodes are shown in Table 9 at three different times; at 1530 on January 4 just prior to the introduction of seed, at 0100 on January 5 just after final thermal and electrical conditions had been established and at 1000 on January 5 shortly before the end of the life tests. Also, prior to reaching the final test conditions, the holds were maintained at two calibration points to make cross checks between several diagnostic sensors, i.e., the electrode thermocouples, Ir-Rh thermocouple extending into the gas stream in the mixer and inlet transistion section and the optical pyrometers sighting onto the mixer wall and electrode 108 in in the test section. At these calibration points, one at approximately 1850°C plasma temperature and a second at approximately 1600°C electrode surface temperature, comparisons were also made between thermocouple, pyrometer and heat flux data and the test predictions calculated prior to testing.

(B) Test Data Analysis

As can be seen from Table 9 there was a progressive loss of thermocouples during the life test. Also the unsheathed thermocouples read 40-50°C higher than the sheathed thermocouples in the same electrode implying calculated surface temperatures 120-150°C higher.

The temperature rise due to joule or resistive heating was determined at the mid-point of the test and was found to compare favorably with the predicted values for cathodes 102 and 105. The values for the anodes for these material groups varied significantly from predictions when the same comparison was made. The second material group demonstrated the greatest consistency in

TABLE 9

CALCULATED ELECTRODE SURFACE TEMPERATURES (^{o}C)

Electrode No.	Thermocouple # (Type)	1530 1/4/78	0100[2] 1/5/78	1000[2] 1/5/78
102	0 (Sheath)	1690 ± 75	1607 ± 65[3]	1593 ± 75[3]
105	1 (Sheath)	1565 ± 75	1666 ± 75	*
105	11 (No Sheath)	1711 ± 70	*	*
111	9 (Sheath)	1634 ± 75	*	*
202	13 (Sheath)	1831 ± 75	*	1745 ± 75
205	14 (Sheath)	1663 ± 75	1774 ± 75	*
205	15 (No Sheath)	1785 ± 70	*	*
211	9 (Sheath)	1590 ± 75	*	*

*Either inoperable or unreliable thermocouple.

(1)Design point just prior to seed addition, I = 0 amps.

(2)Design point with seed and I = 5 amps.

(3)102-202 I = 1.2 amps.

thermal behavior between anode and cathode (experimental) resistive heating at full current load and pre test predictions.

Thermocouple readings throughout the test have been plotted and are shown in Figures 29-32 grouped either according to location from the plasma surface, i.e., electrode front face (hot), electrode back face (cold), insulation and copper.

Cooling water flow rates to eighteen electrodes were individually controlled and ranged between 4 and 6 cc/sec. The six electrodes (107-109, 207-209) provided by General Electric had a flow rate of 10-12 cc/sec. Heat fluxes as determined calorimetrically, ranged from 16 to 35 w/cm^2 for all electrodes except for pairs 7 through 9, the GE "flexbed". As in proof test 1, the "flexbed" electrodes exhibited higher heat fluxes than the others in the test assembly, 40 to 50 w/cm^2 for the cathode and 50 to 70 w/cm^2 for the anode. No significant change in heat fluxes was noted following the addition of seed. Representative heat flux data are shown in Figures 33-36

Electrical Performance - Proof Test 3 (WESTF Test 39)

(A) Characteristics of Applied Voltage versus Current as a Function of Time.

Computer plots, as a function of time, of V_L, the applied voltage; V_H, the voltage of the positive electrode; and V_K, the voltage of the negative electrode relative to ground are given in Figures 34 through 37. The distance between V_H and V_K gives the magnitude of V_L as do the small triangles at the top of the graphs. The currents in the positive and negative electrode circuits, I_2 and I_1, respectively, are plotted in the lower part of the figures.

The usual slow rise in the potential of the cathodes with continued operation was evident for each electrode-pair with the exception of the first pair. For this electrode pair, V_K was more negative than V_H was positive until the mid-point of the test. After mid-run tests were completed, electrode pair 1 drew current and followed the customary pattern, with V_K slowly rising to zero potential and V_H slowly approaching V_L. However, neither it nor

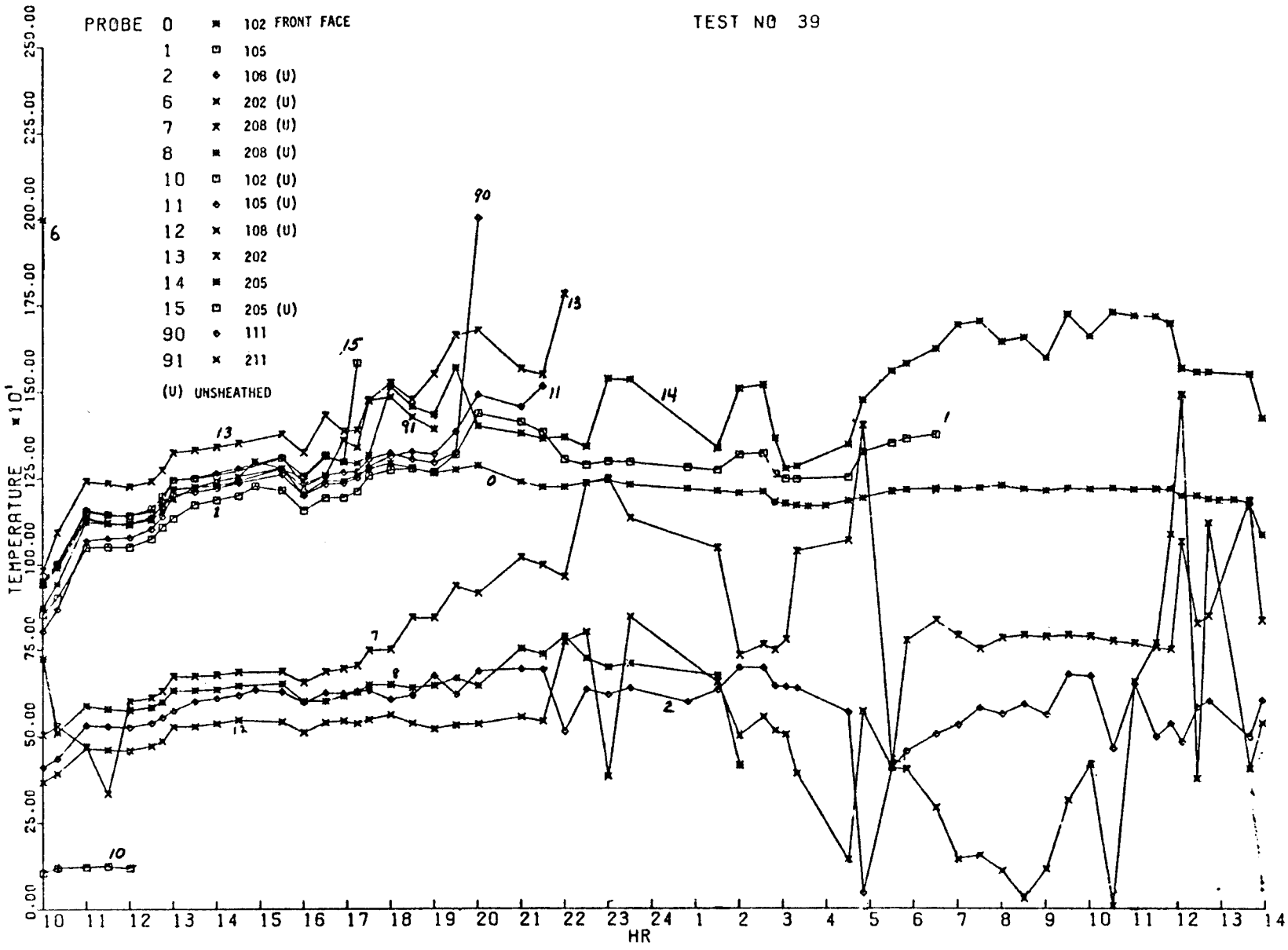

Figure 29. Proof Test 3 - Electrode Temperatures (T.C. 3 mm from Plasma)

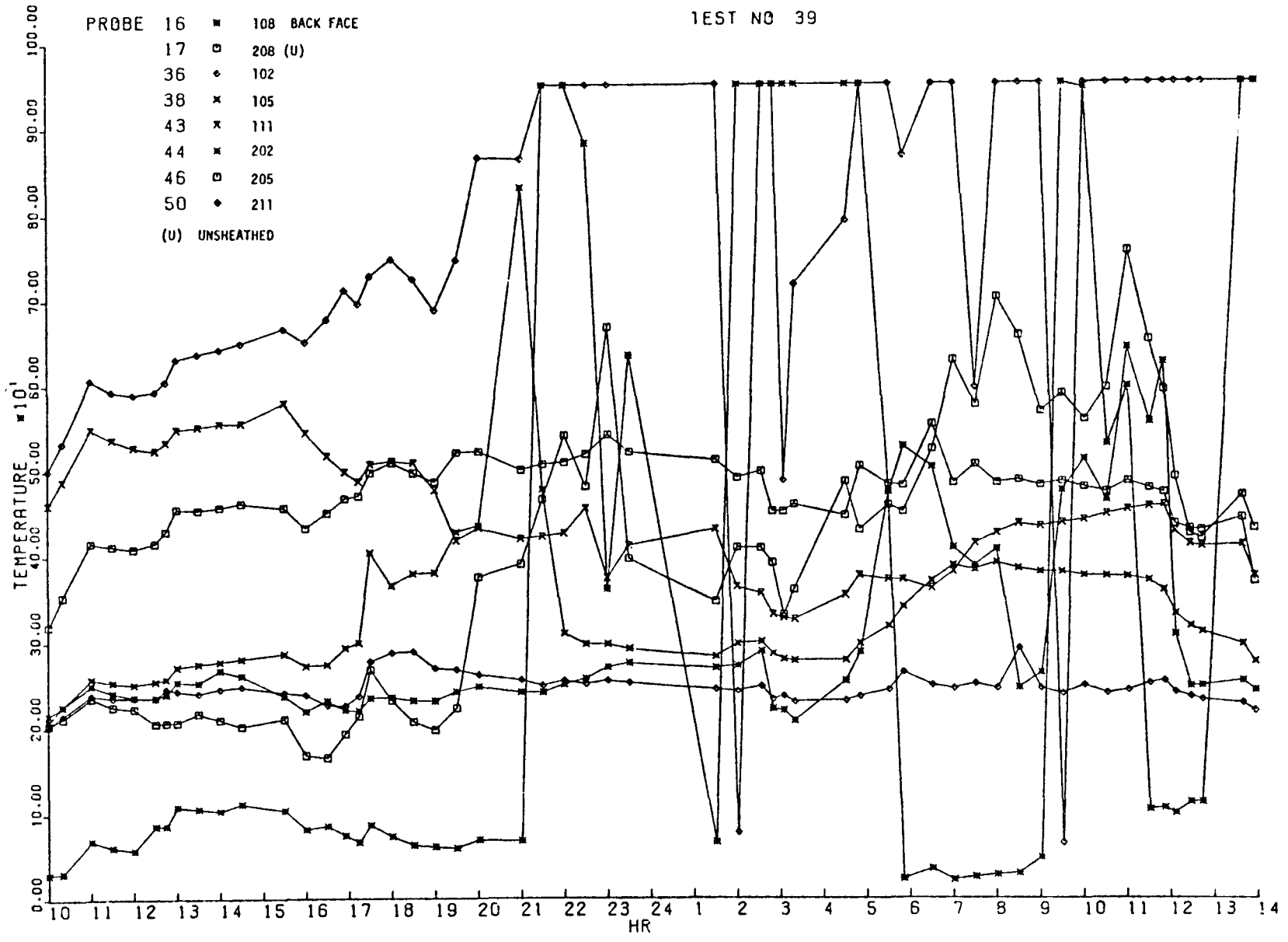

Figure 30. Proof Test 3 - Electrode Temperatures (T.C. 3 mm from Attachment)

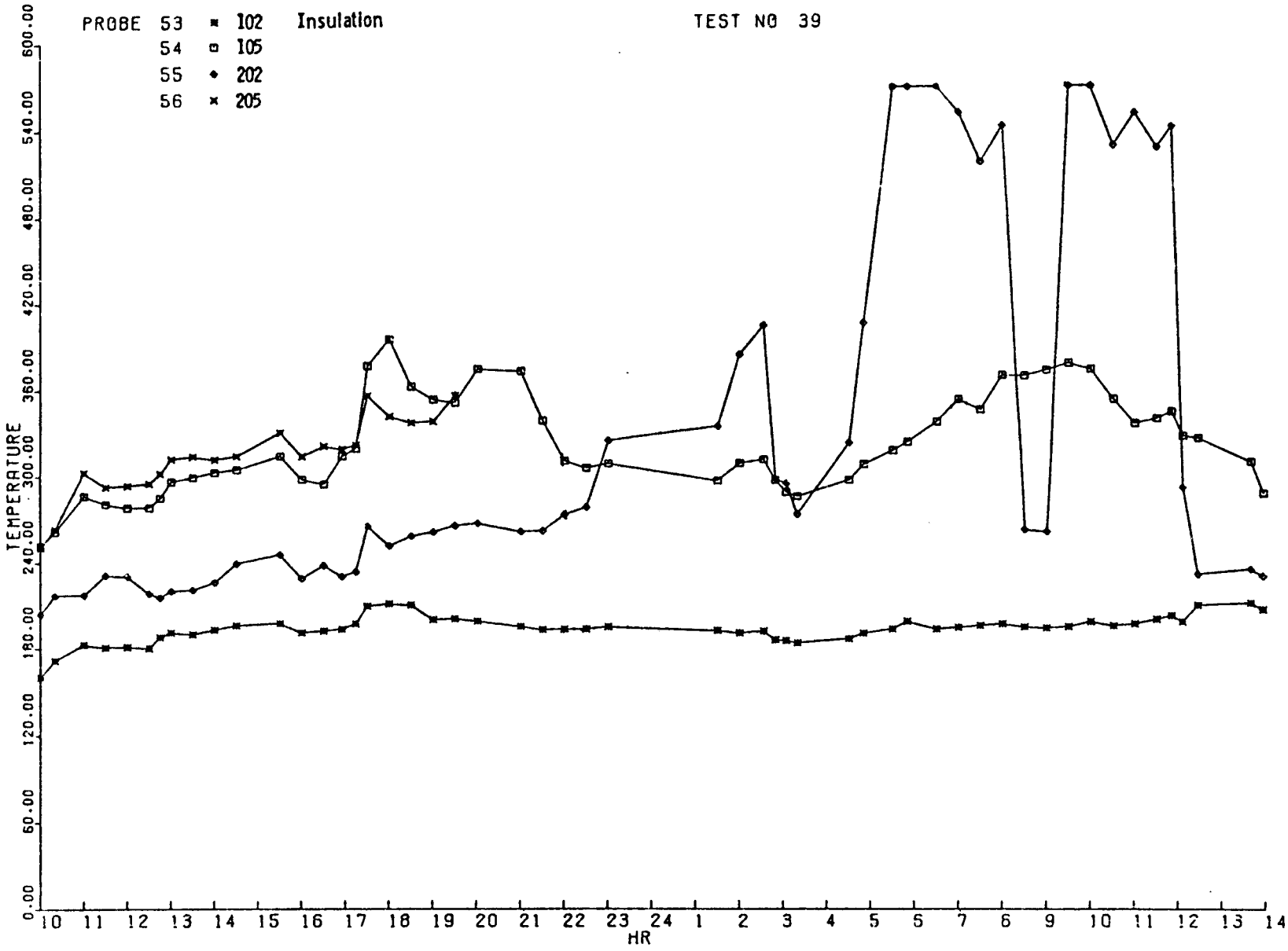

Figure 31. Proof Test 3 - Insulator Temperatures (T.C. in Plane with Backface T.C.) (See Fig. 30)

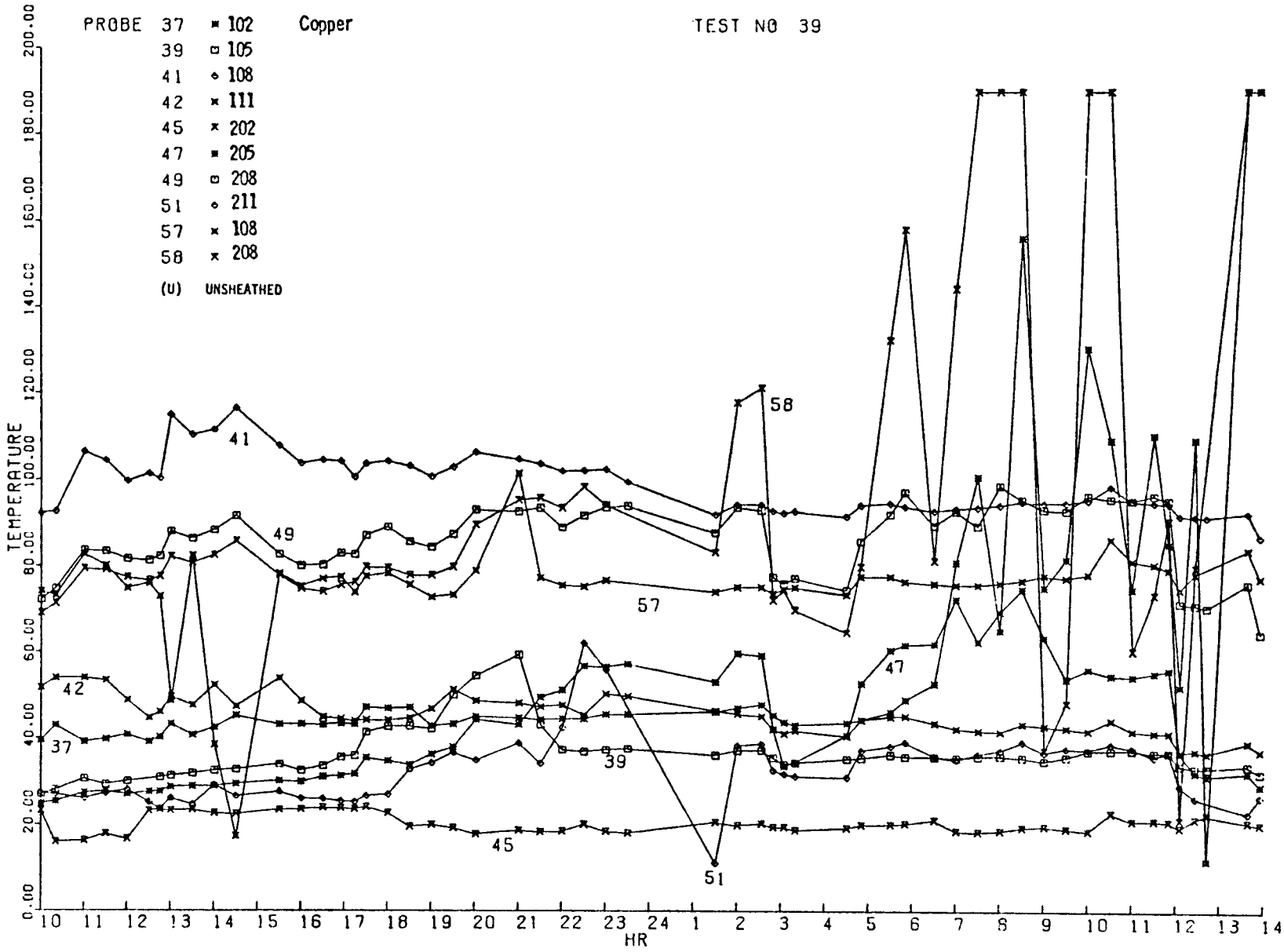

Figure 32. Proof Test 3 - Copper Temperatures (T.C. 3 mm from Electrode Attachment)

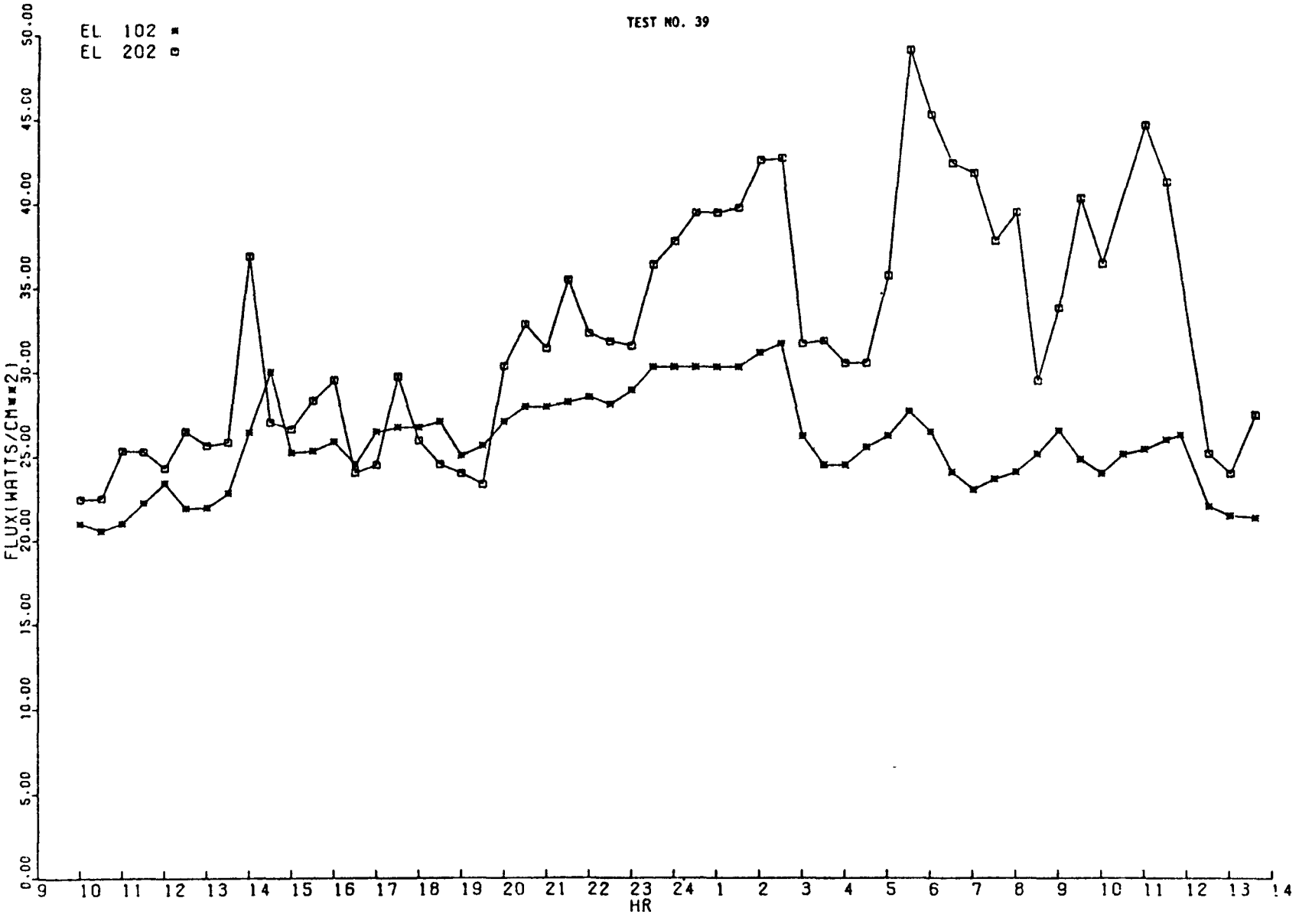

Figure 33. Proof Test 3 - Heat Flux Data - Electrode Pair 102-202

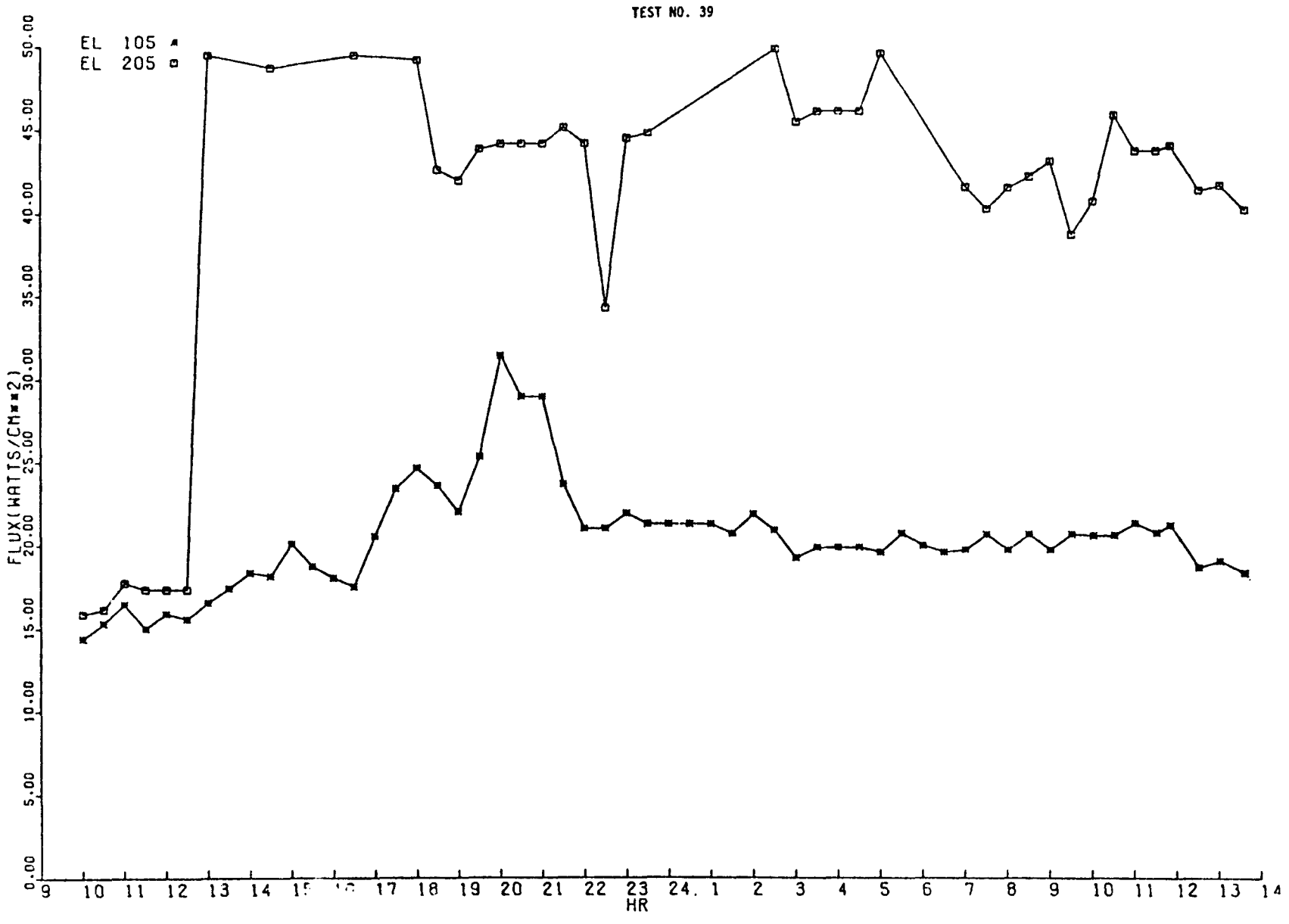

Figure 34. Proof Test 3 - Heat Flux Data - Electrode Pair 105-205

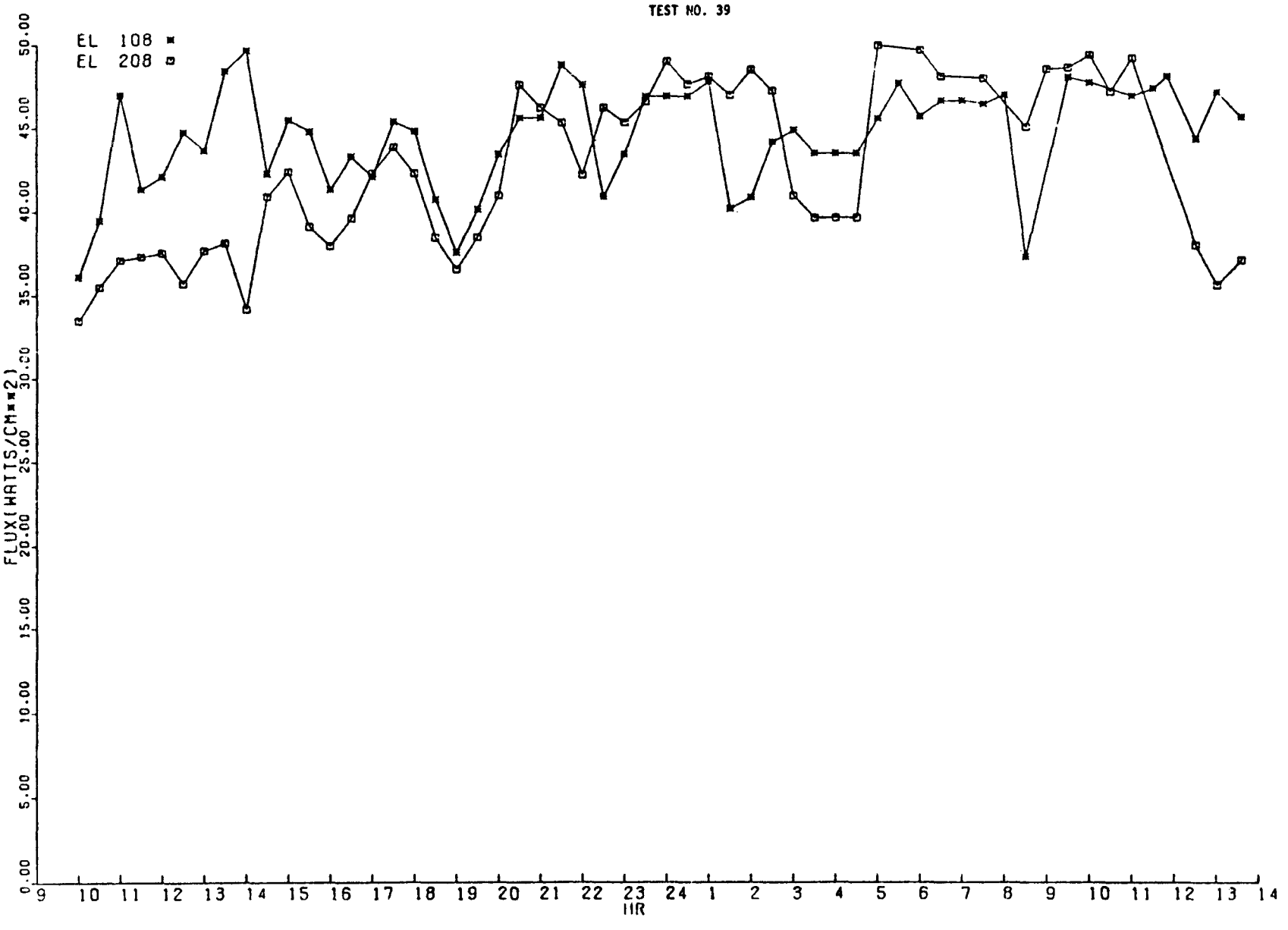

Figure 35. Proof Test 3 - Heat Flux Data - Electrode Pair 108-208

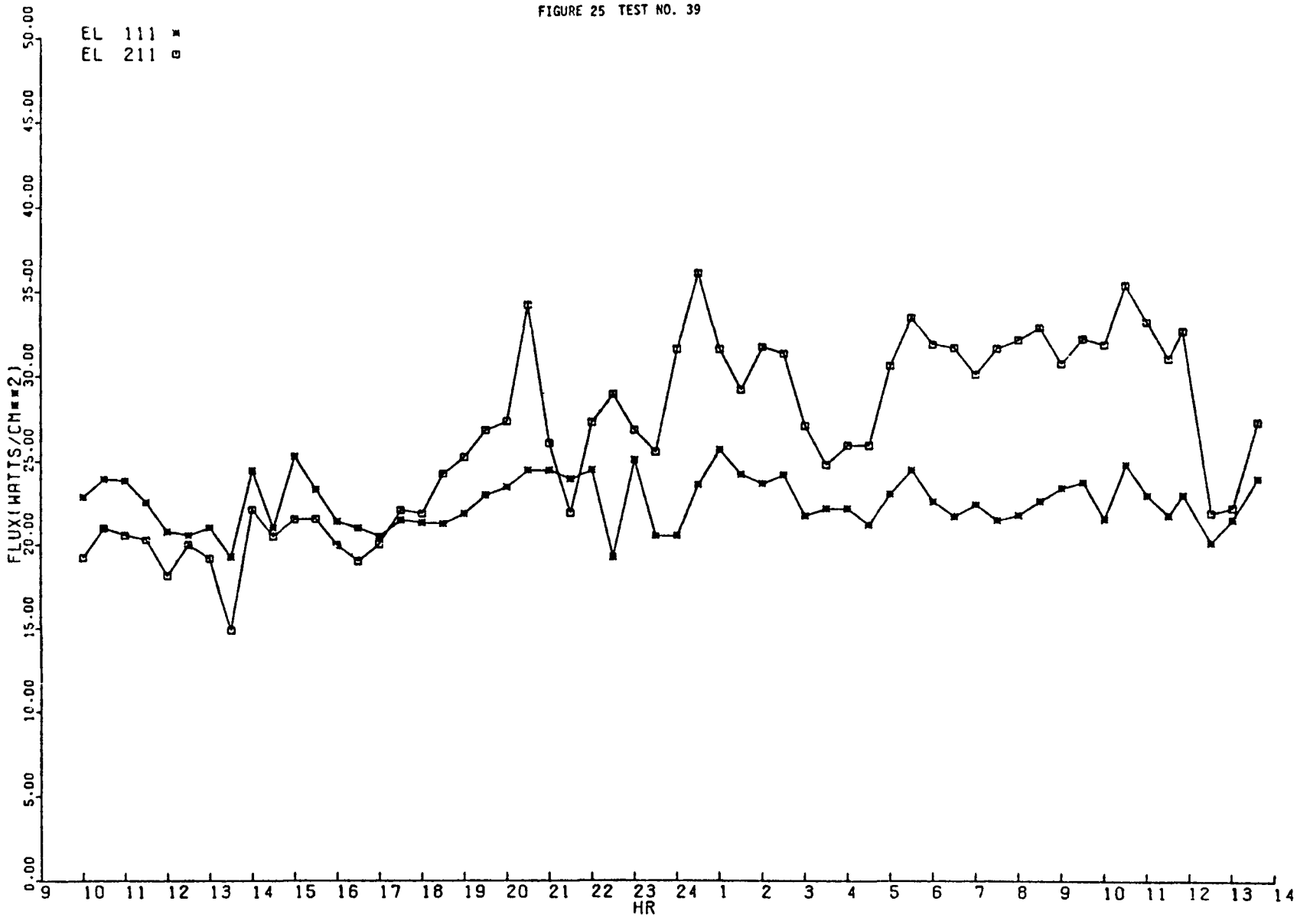

Figure 36. Proof Test 3 - Heat Flux Data - Electrode Pair 111-211

electrode pair 12 could be brought to the maximum loading of 5 amperes. It is possible that poor electrical contact was responsible for the departure from expected performance. The gradual rise in V_K is believed due to increased leakage between the negative electrodes and ground as a result of the migration of seed ions to the cathode.

All of the data shown in Figures 37 to 39 were taken with the electrodes floating. When the electrodes are floating, I_2, the current to the positive electrode, should equal I_1, the current to the negative electrode. The two currents were substantially equal for all electrode-pairs in run 39 except for 4 and 12. I_2 for electrode pair 4 was equal to I_1 for the early part of the run, but because of a suspected systems error, became significantly different from thereon. The reason for the discrepancy in the two currents at E.P. 12 is not understood. Such discrepancies should be investigated during the run to determine whether they are caused by errors in instrumentation or are real effects.

A comparision of curves for Proof Test 3 with those of Proof Test 2 (Reference 1) indicate that the curves of electrode voltage versus elapsed time at a 5 amperes load for Proof Test 2 were substanitally more stable than for Proof Test 3. This effect may be due to changes in plasma conductivity instabilities within the channel.

At various times during the test the voltage required to pass 5 amperes through a given electrode-pair dropped precipitously as if the electrode-pair was substantially shorted. Such a temporary near-short is evident in electrode pair 2 (see Figure 37) at about 8.5 hours into the run. A near-short of longer duration is evident in electrode-pair 3 between 8.5 and 12 hours. The curves for electrode pairs 7 and 8 reveal (see Figure 39) near-shorts of fairly long duration at the beginning and end of the run.

Table 10 gives average values for the applied voltage V_L and the load currents for time periods of about 1.5 hours duration just prior to the mid-point tests and prior to the end of run tests. Also shown are the calculated plasma voltages, V_p, required to pass these currents. The calculations of

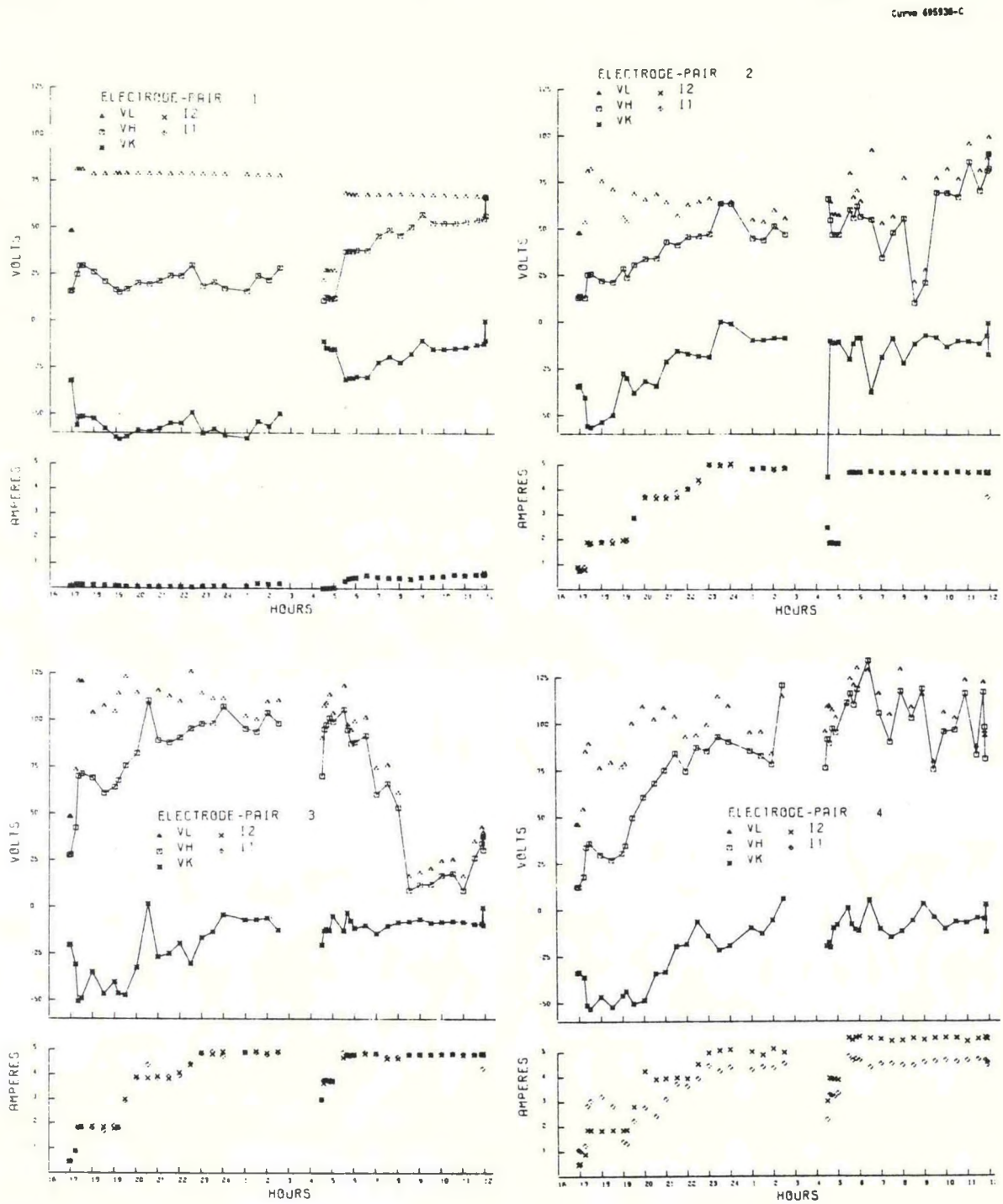

Figure 37. Applied Voltages and Currents for Different Electrode-Pairs, V_L is Applied Voltage, V_H is Voltage of Positive Electrode, V_K is Voltage of Cathode Relative to Ground Potential

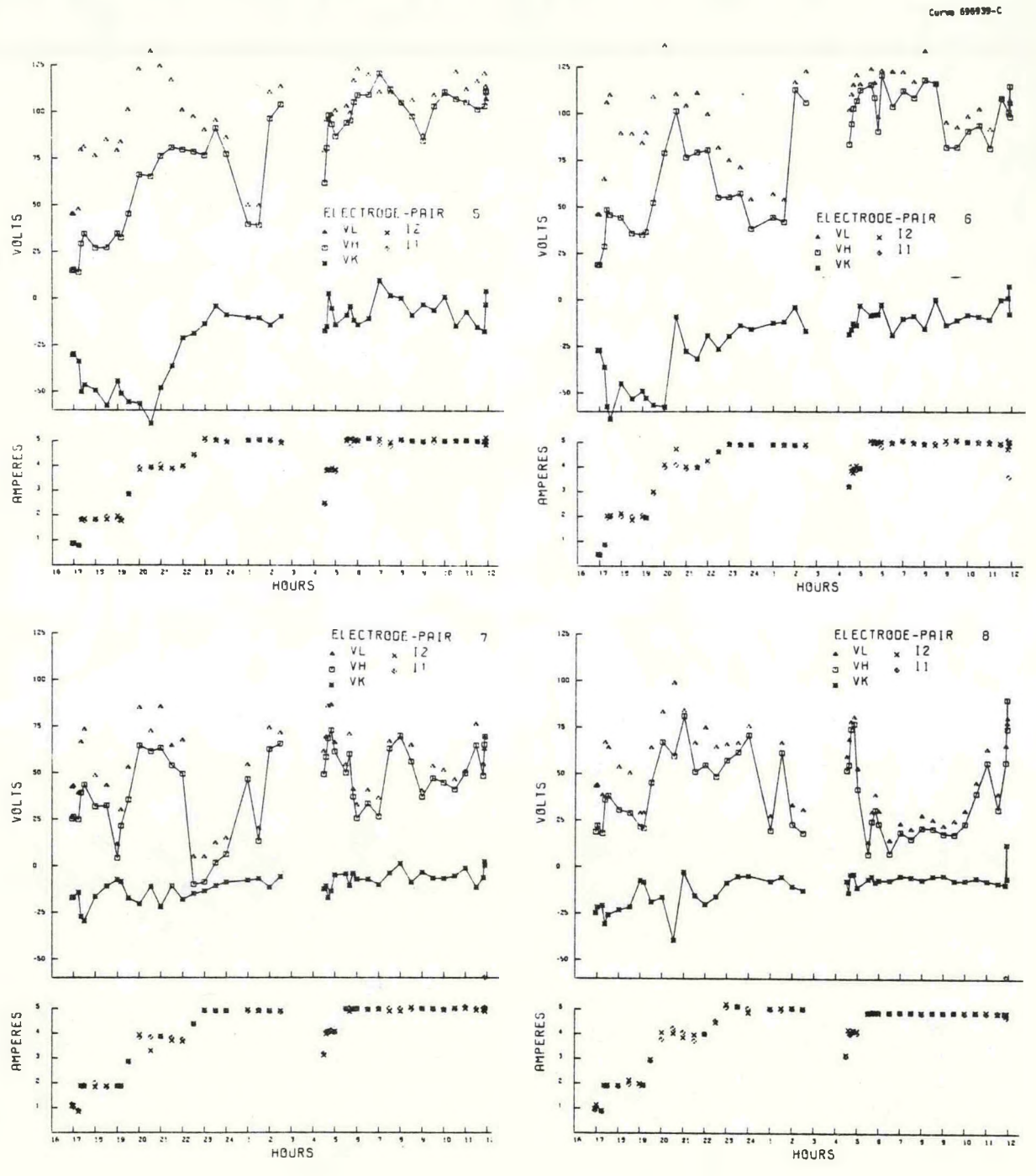

Figure 38. Applied Voltages and Currents for Different Electrode-Pairs, V_L is Applied Voltage, V_H is Voltage of Positive Electrode, V_K is Voltage of Cathode Relative to Ground Potential

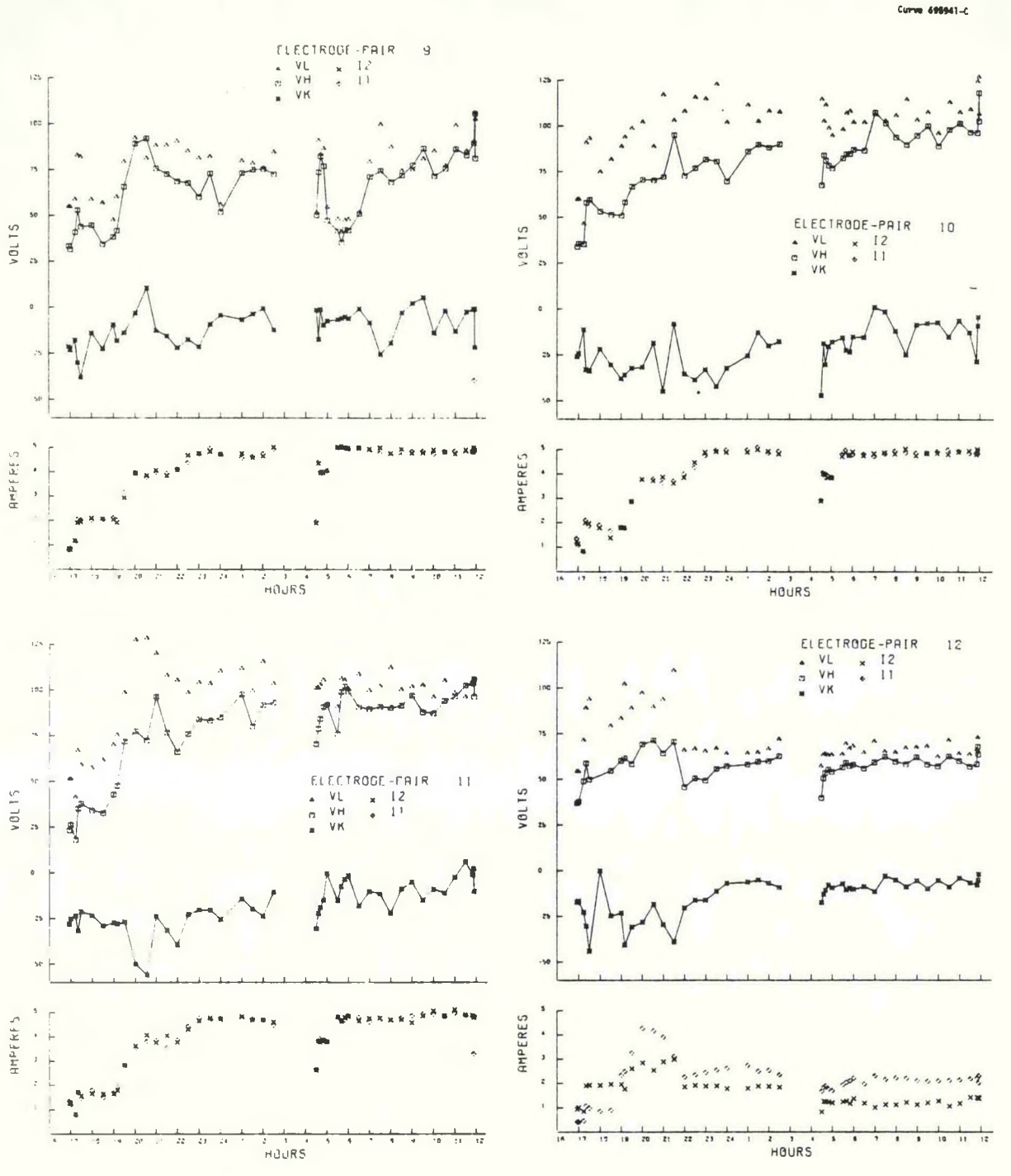

Figure 39. Applied Voltages and Currents for Different Electrode-Pairs, V_L is Applied Voltage, V_H is Voltage of Positive Electrode, V_K is Voltage of Cathode Relative to Ground Potential

TABLE 10. VALUES OF ΔV FOR DIFFERENT ELECTRODE PAIRS AT MID-POINT AND END OF PROOF TEST 3

Electrode Pair	Time: 1-2:30 - 1/5/78 VL	IL	V_p	ΔV	Electrode Materials	Avg. T = 4.5 mhos/m Time: 10:31-11:54 - 1/5/78 VL	IL	V_p	ΔV
1	-	-	-	-	Graded Solid Solution of $LaCrO_3$ + $LaAlO_3$	-	-	-	-
2	56	4.9	21	35	" "	89	4.7	39	60
3	106	4.9	21	85	" "	38	4.8	40	-
4	97	4.5	19	78	Mixture of $LaCrO_3$ plus $SrZrO_3$	101	4.7	39	63
5	112*	5.0	21	91	" "	114	5.0	41	73
6	120*	4.9	21	99	" "	102	5.0	41	61
7	71*	4.9	21	50	$LaCrO_3$ 88% dense with flexbed backing	61	5.1	42	57
8	67	5.0	21	46	" "	57	4.8	40	17
9	80	4.7	20	60	" "	91	4.9	40.0	51
10	108	5.0	21	87	Plasma Sprayed MAFF graded to Hercynite	109	4.9	40.0	69
11	108	4.7	20	88	" "	101	4.9	40.0	61
12	-	-	-	-	" "	-	-		
Avg.				72					51

* Abnormally low values of V_p, which are considered to represent near-shorts were ignored in making the averages.

V_P are based on average values of conductivity determined immediately after the two time periods noted in the Table.

The difference between the applied voltage and the voltage drop across the plasma, defined by the equation $\Delta V = V_L - V_P$, expresses the combined sum of the anode and cathode potential drops and the joule voltage loss in the electrodes. From the Table it is evident at ΔV losses are somewhat lower at the end of the run. The average value of ΔV dropped from 72 to 51 volts. Comparable average values of ΔV at the beginning and end of Proof Test 2 were 53 and 56 volts, respectively.

From separate tests in which the joule losses across electrodes of different materials were evaluated as a function of current and temperature, it is concluded that a significant part of the ΔV losses was due to joule heat losses resulting from high resistances of the cooled back faces of the electrodes.

The separate electrical tests are different electrode materials also established that the $LaCrO_3$ type materials are susceptible to a "seasoning" effect, in which the apparent resistivity of the material experiences a very substantial decrease after being loaded at currents of about one ampere/cm^2 for extended period of times. This effect would be expected to show up in the life tests as a drop in the value of applied voltage required to impress a given current through an electrode-pair. Such drops in applied voltages can be seen in electrode pairs 2, 3, 5, 6, and 11. The lowest ΔV lapses were experienced by electrode-pair 7 and 8, which consisted of 88% dense $LaCrO_3$ with a "flexbed" attachment. However, both of these electrode-pairs experienced relatively long intervals when they were apparently operating under near-short circuit conditions.

A more direct comparison of the different electrode materials is afforded by Figures 40, 41 and 42 in which the applied voltages and resulting load currents are plotted as a function of electrode-pair number at different times during the run.

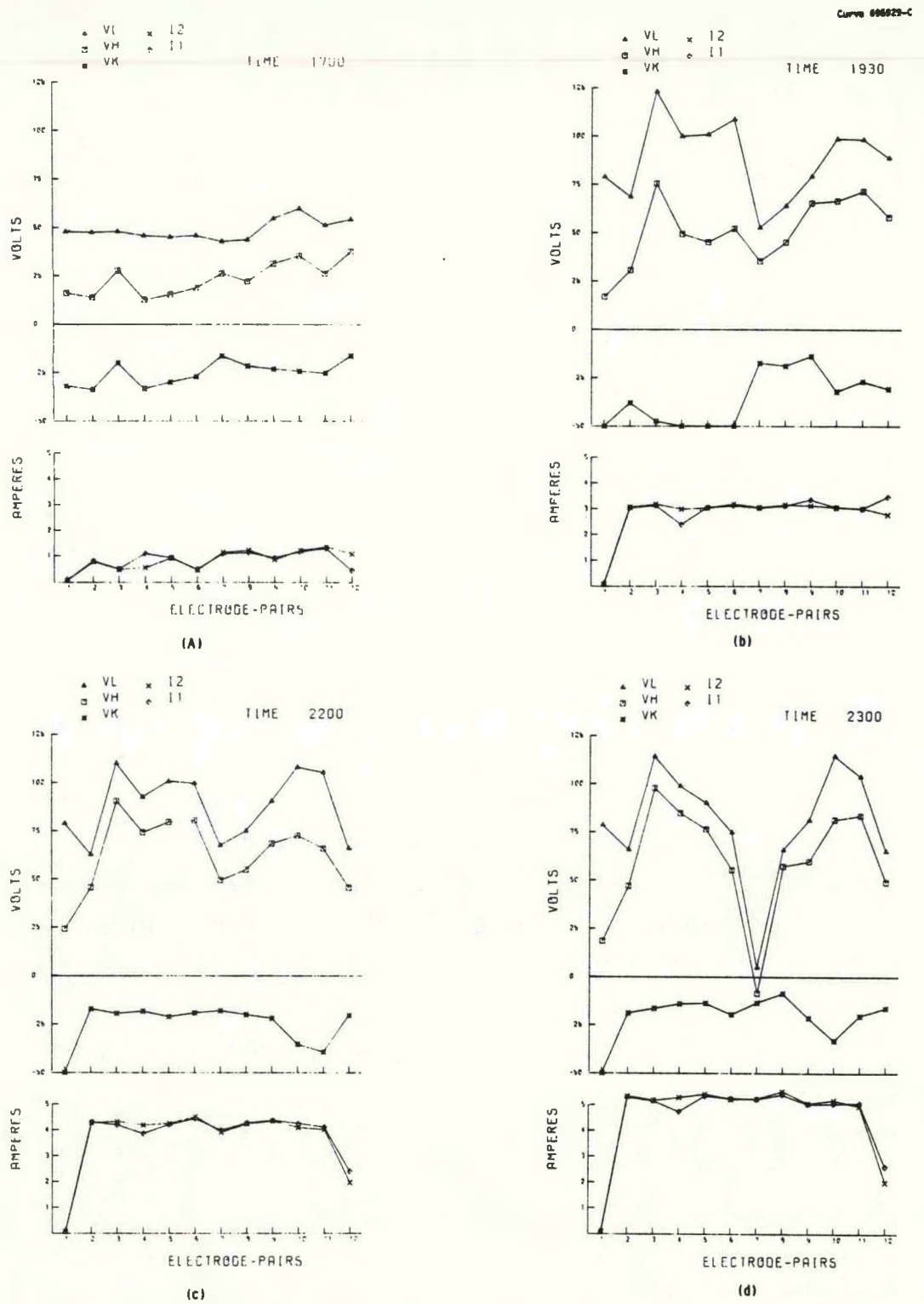

Figure 40. Applied Voltages, Voltages to Ground of Positive and Negative Electrodes and Electrode Currents as Function of Electrode-Pairs at Different Times During Run 39, 1/4/78

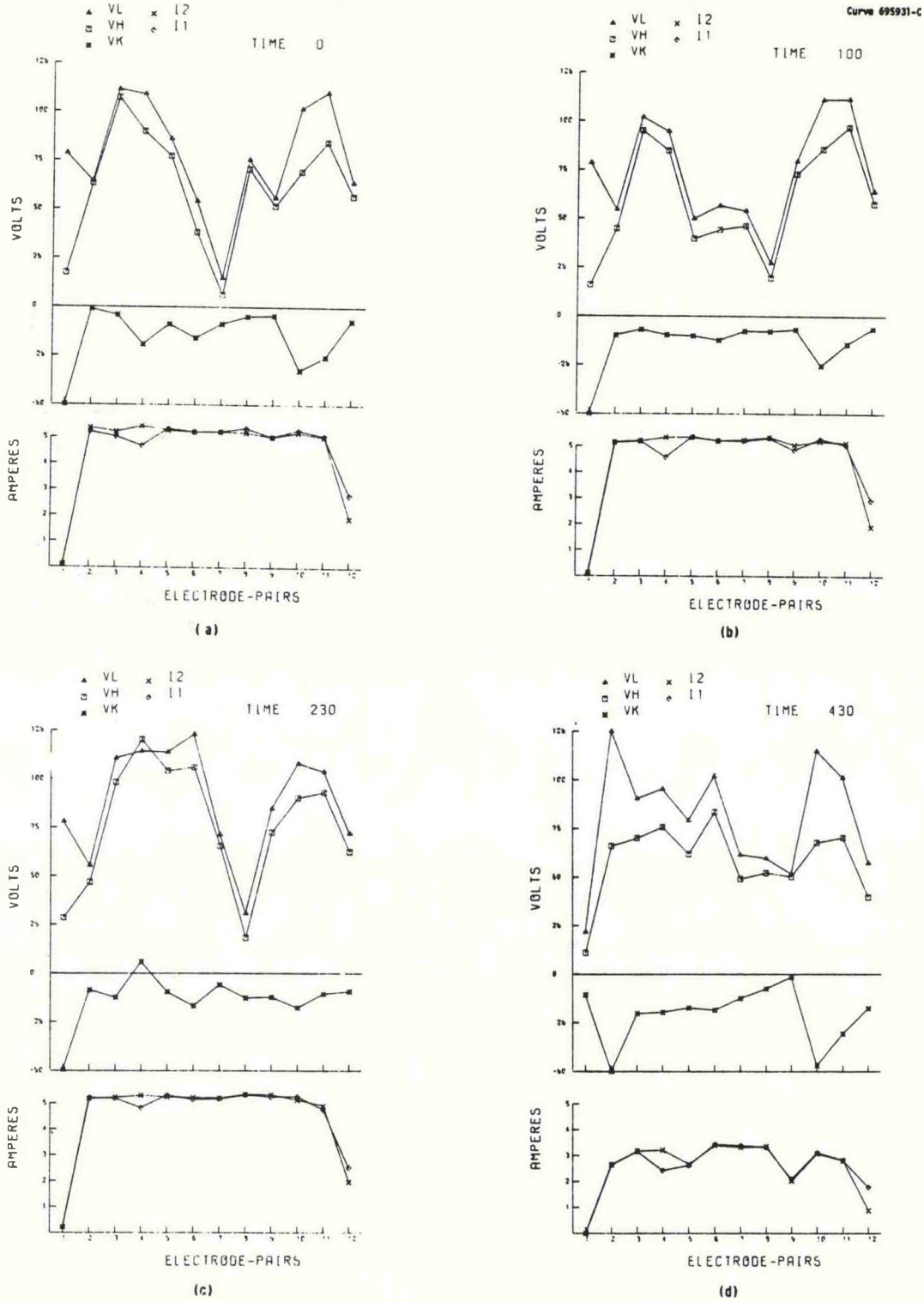

Figure 41. Applied Voltages, Voltages to Ground of Positive and Negative Electrodes and Electrode Currents as Function of Electrode-Pairs at Different Times During Run 39, 1/5/78

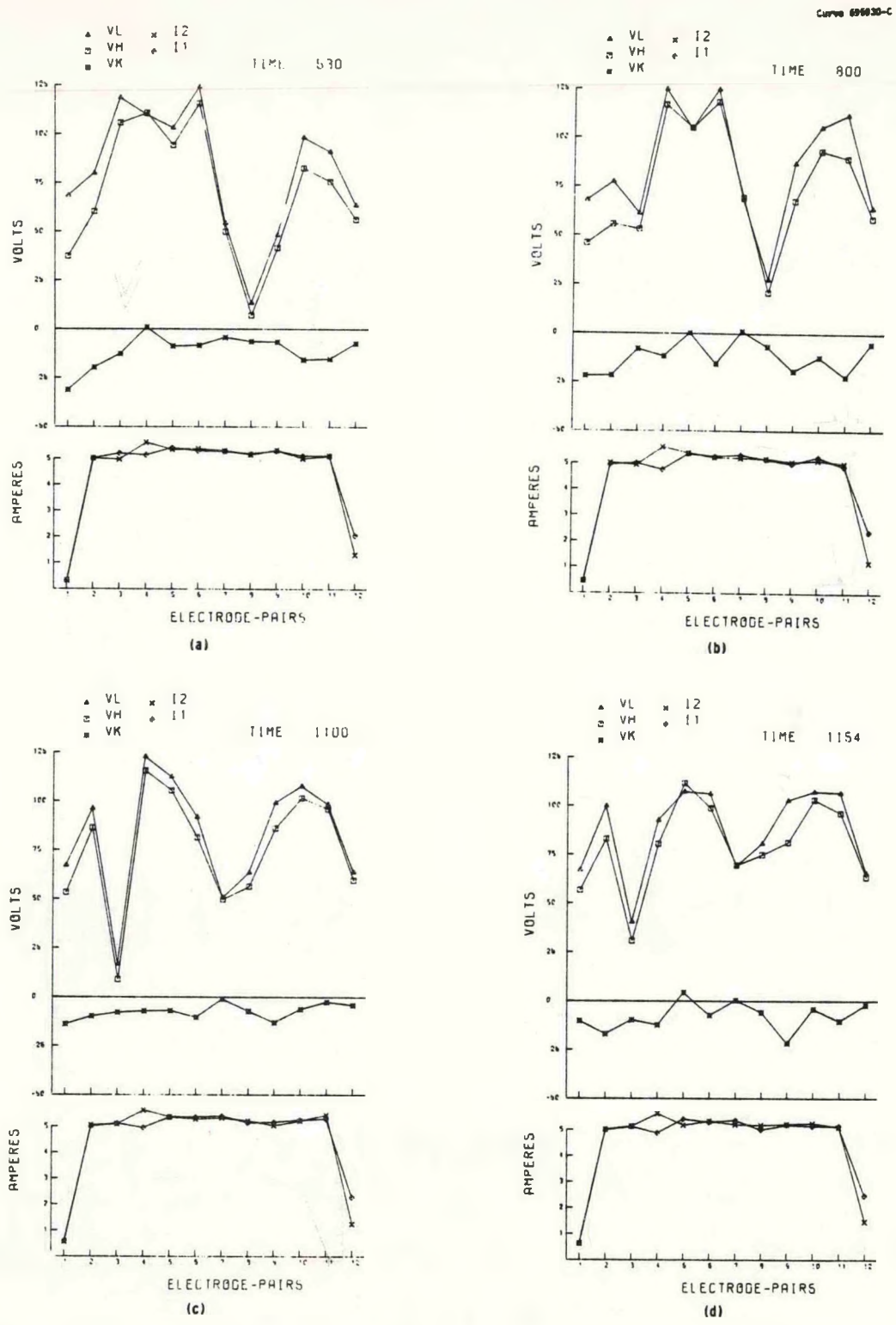

Figure 42. Applied Voltages, Voltages to Ground of Positive and Negative Electrodes and Electrode Currents as Function of Electrode-Pairs at Different Times During Run 39, 1/5/78

From Figure 40(a), it is seen that the application of 50 Volts produced currents between .8 and 1.4 amperes for all electrode-pairs except 1, 3, and 12. Once the current level is increased to 3 amperes, (see Figure 40(b) at time 1930) it is apparent that electrode-pairs 7, 8 and 9 require significantly lower values of V_L than the neighboring electrode-pairs. The values of V_L for electrode-pairs 10, 11, 12 were higher than those for electrode pairs 7, 8, 9, but lower than the remaining electrode-pairs in the channel. However, by the time a 4 amperes current loading level was reached, the values of V_L for electrode-pairs 10, 11, 12 were comparable to the remaining electrode pairs.

At time 2300 (see Figure 40(d)) there is a clear short across the elements of E.P.7. The shorts, or near-shorts, across electrode-pairs 7 and 8 are evident at various time intervals shown in Figures 41 and 42. A similar near-short is apparent in electrode pair 3 at time 1100 (see Figure 42(c), just before the end of the run. Comparable evidence of shorts and near-shorts across given electrode-pairs did not occur in Proof Test 2.

The evidence, both from recent runs and from the separate electrical tests on electrode materials referred to previously, strongly indicates that the pure $LaCrO_3$ electrodes have significantly lower voltage drops and lower joule losses than mixtures of $LaCrO_3$ with other ceramic materials. However, since the resistivity of $LaCrO_3$ is a function of processing, it is important that optimum processing be employed to insure that the low temperature resistivity is at a minimum to prevent excessive voltage drops across the electrodes.

Figures 43 and 44 compare the electrical performance of the channel at the beginning of the mid-point tests with the performance observed at the end of the tests. The electrical data taken during the mid-point tests under electrically floating cathode grounded and anode grounded conditions are plotted on the left side of the figures. Similar data taken at the end of the run are plotted on the right side of the figures. The change in electrical characteristics does not appear to be very marked. The electrical leakage

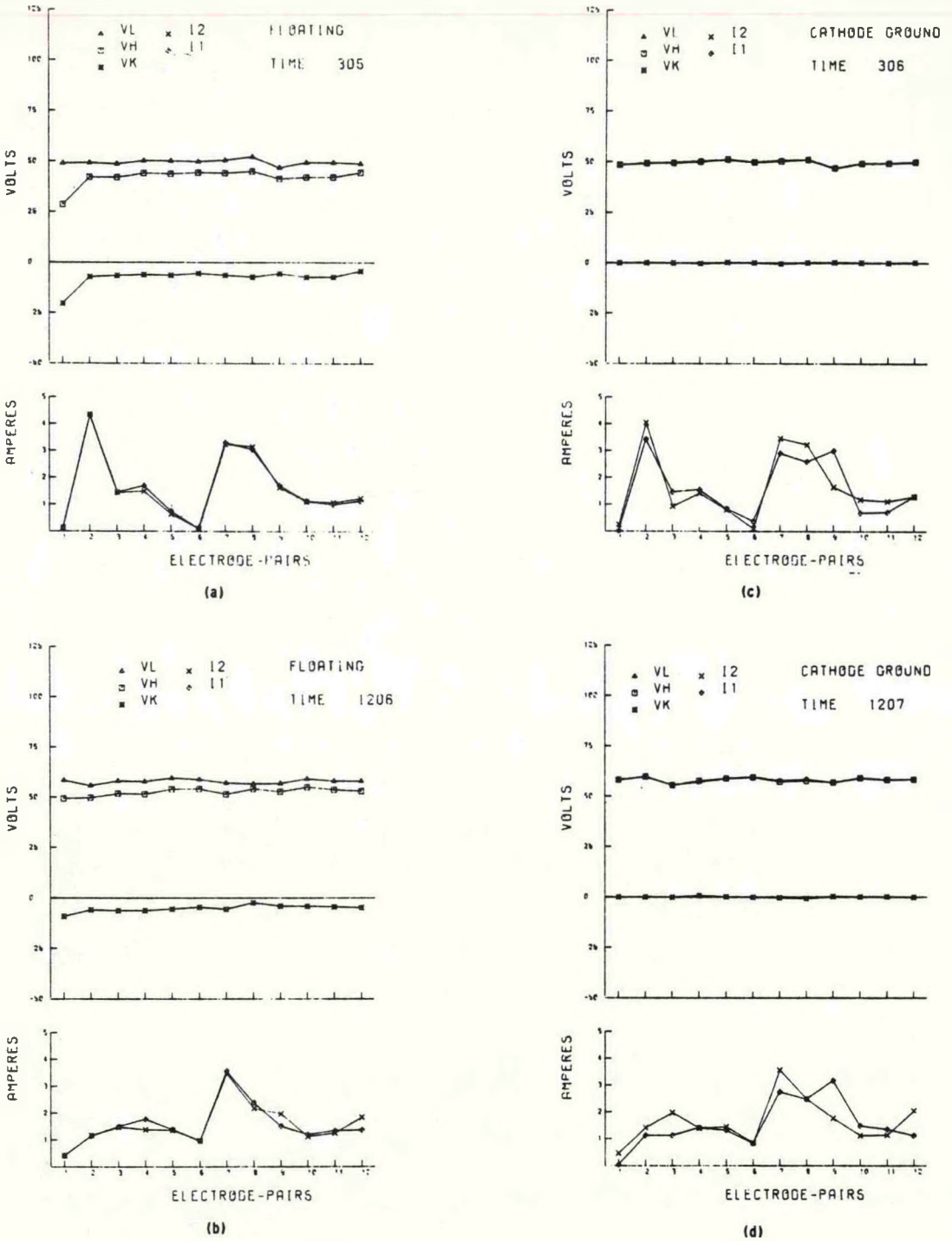

Figure 43. Comparison of the Electrical Characteristics of Different Electrod Pairs at the Mid-Point Test with Characteristics During the End of the Run Tests for Run 39, 1/5/78.

Curve 695944-8

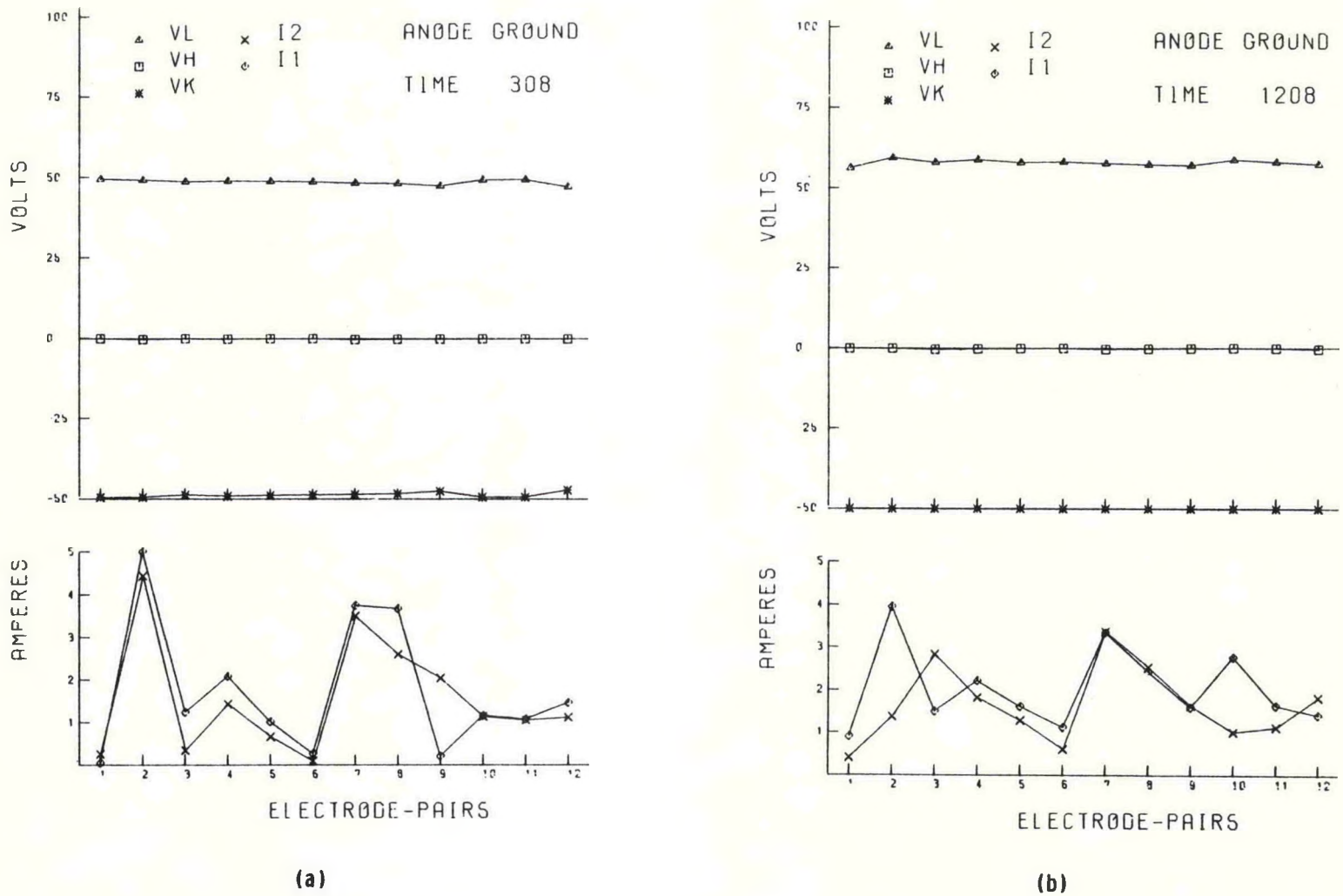

Figure 44. Comparison of the Electrical Characteristics of Different Electrode-Pairs at the Mid-Point Test with Characteristics During the End of the Run Tests for Run 39, 1/5/78

currents from the cathode electrodes at the end of Proof Test 3 was not as pronounced as they were at the end of Proof Test 2.

(B) Current Versus Voltage Characteristics

The current versus voltage characteristics of the channel were taken just prior to the mid-point tests by dropping the current from 5 amperes to zero amperes in 0.5 ampere steps and recording the data. The current-voltage data taken at this time (between 2:36 and 2:53 on 1/5/78) are shown in Figures 45 and 46. Only electrode-pairs 2, 4, 7, 8, 9 form straight lines which go through the origin. The remaining curves show sharp decreases in slope. These changes in slope have been shown by Heywood and Womack and by Hara and Uchida (References 4, 5). The latter experimenters indicate that the initial shallow slope at low current is due to the rather large changes in potential required to impress a given amount of charge across the interface between the electrodes and the plasma. Once the inflection point is reached, they postulate that an arcing mechanism takes over at the electrode surfaces and the higher current region of the current represents the voltage drops required to impress a given current through the volume of the plasma.

More detail in the very low current region of the I vs V_L curves is afforded by data taken at the end of the run between 12:01 and 12:34 on 1/5/78. These data are plotted on Figures 47 and 48. Again only electrode-pairs 2, 4, 7, 8, 9 are characterized by straight lines which go through the origin. Electrode pairs 7, 8, 9, and 12 have particularly steep slopes. Between 1.5 and 2.0 amperes are drawn by these electrode-pairs when 50 volts are applied, while the remaining electrode-pairs (except for 4) gave a current of less than 1.0 ampere when 50 volts was applied.

It is interesting to note in Figure 45 and 46 that, for a number of electrode-pairs, a decrease in current resulted in an increase rather than a decrease in the required applied voltage (see electrode-pairs 4, 7, 8, 9, and 10 of Figures 45 and 46).

From the electrical tests conducted on separate samples, this effect is believed to be due to an increase in resistivity of the cooled back face of

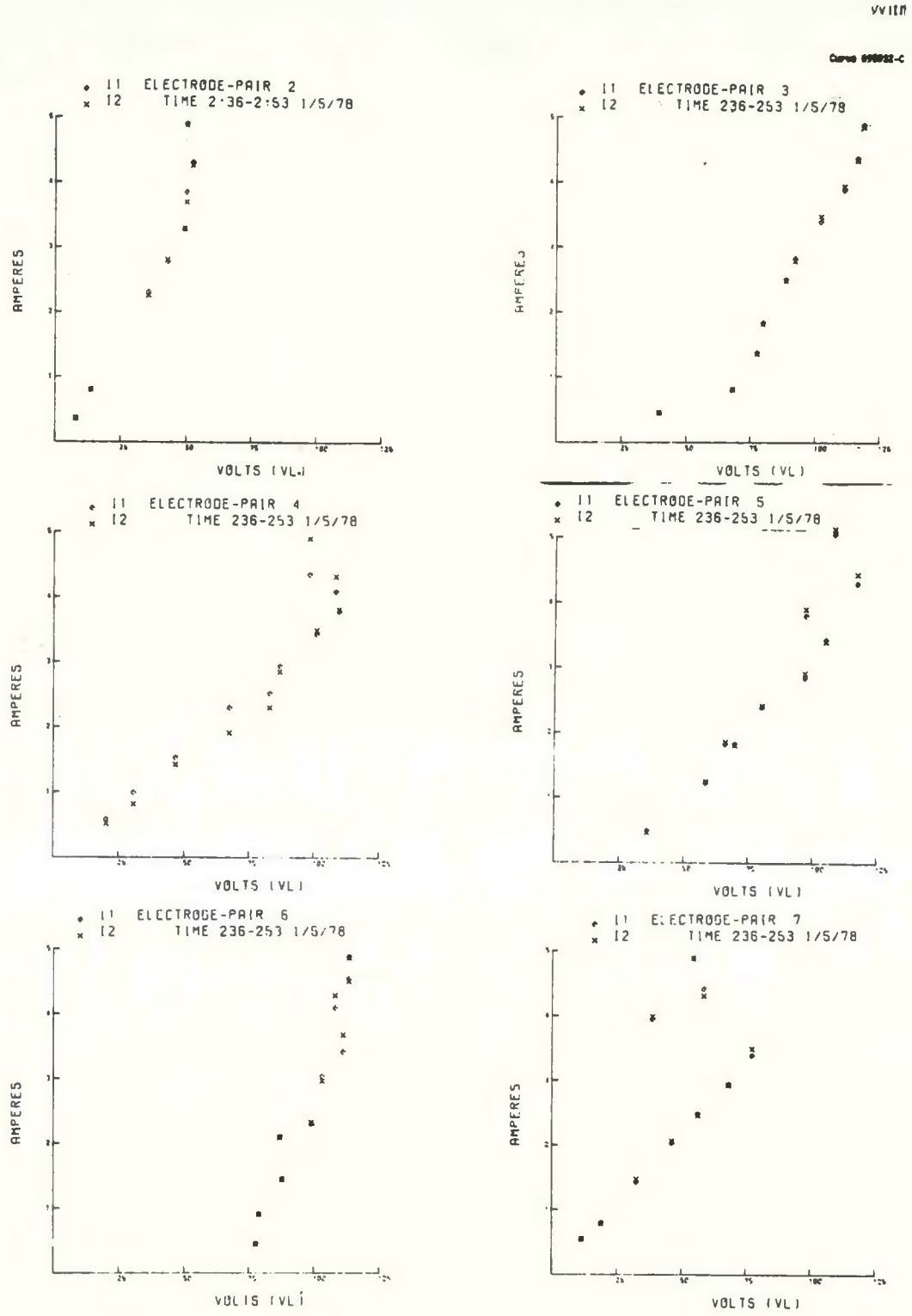

Figure 45. Load Current Versus V_L, Applied Voltage, Taken During Test 39, 1/5/78. Load Current was Decreased From 5 Amperes During Above Measurements.

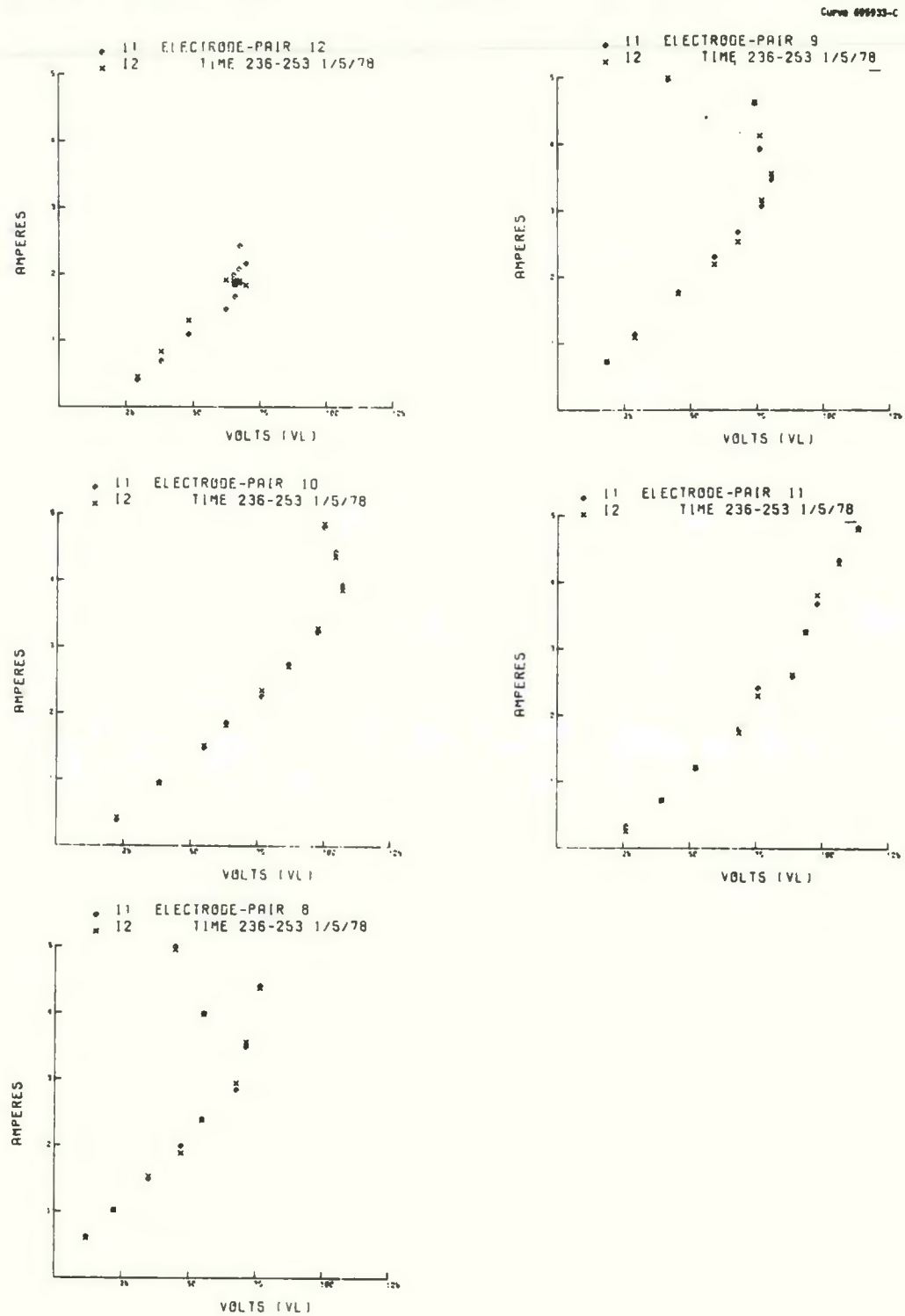

Figure 46. Load Current Versus V_L, Applied Voltage, Taken During Test 39, 1/5/78. Load Current was Decreased from 5 Amperes During Above Measurements.

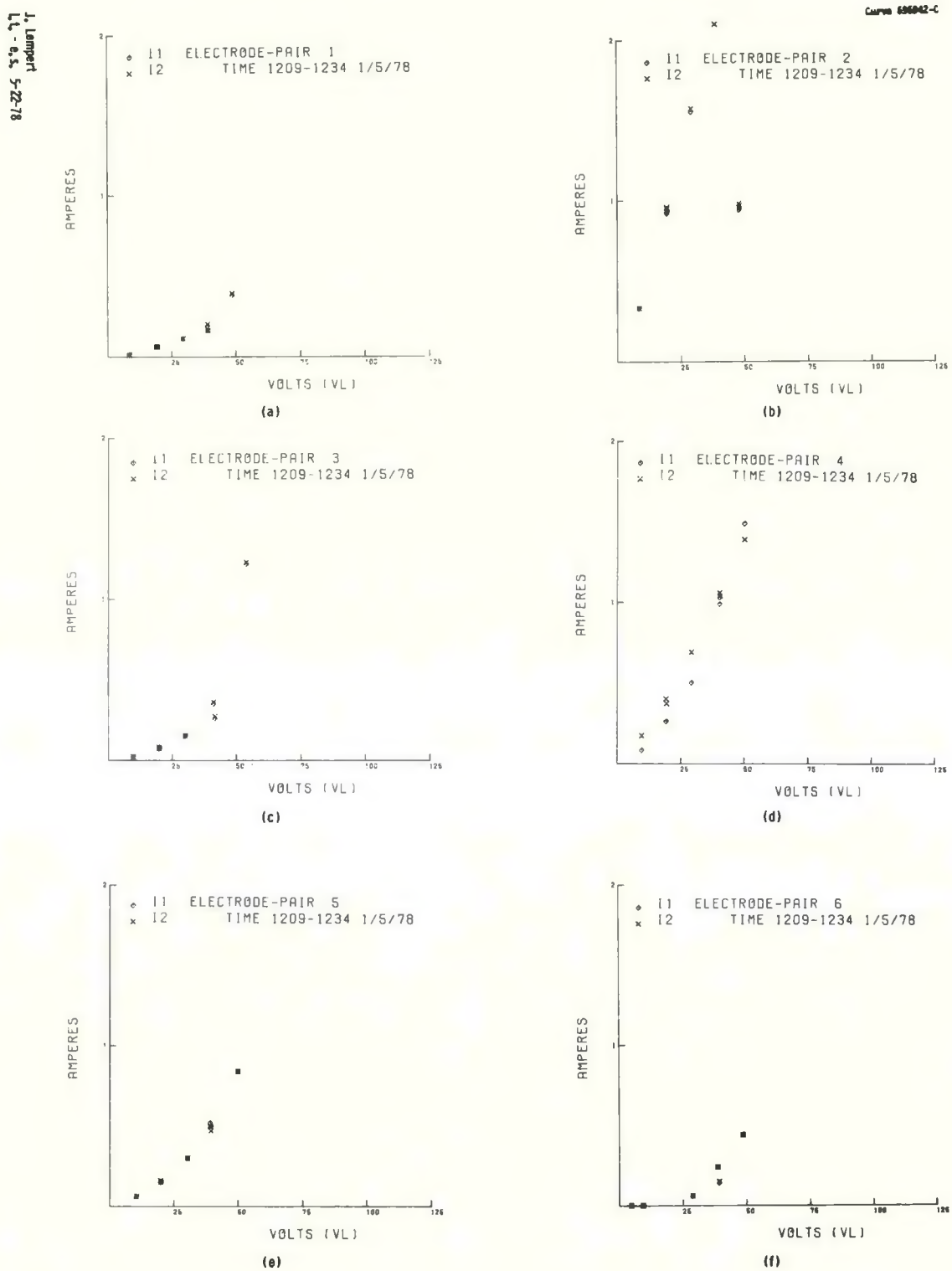

Figure 47. Load Current Versus Applied Voltage V_L Taken During Test 39

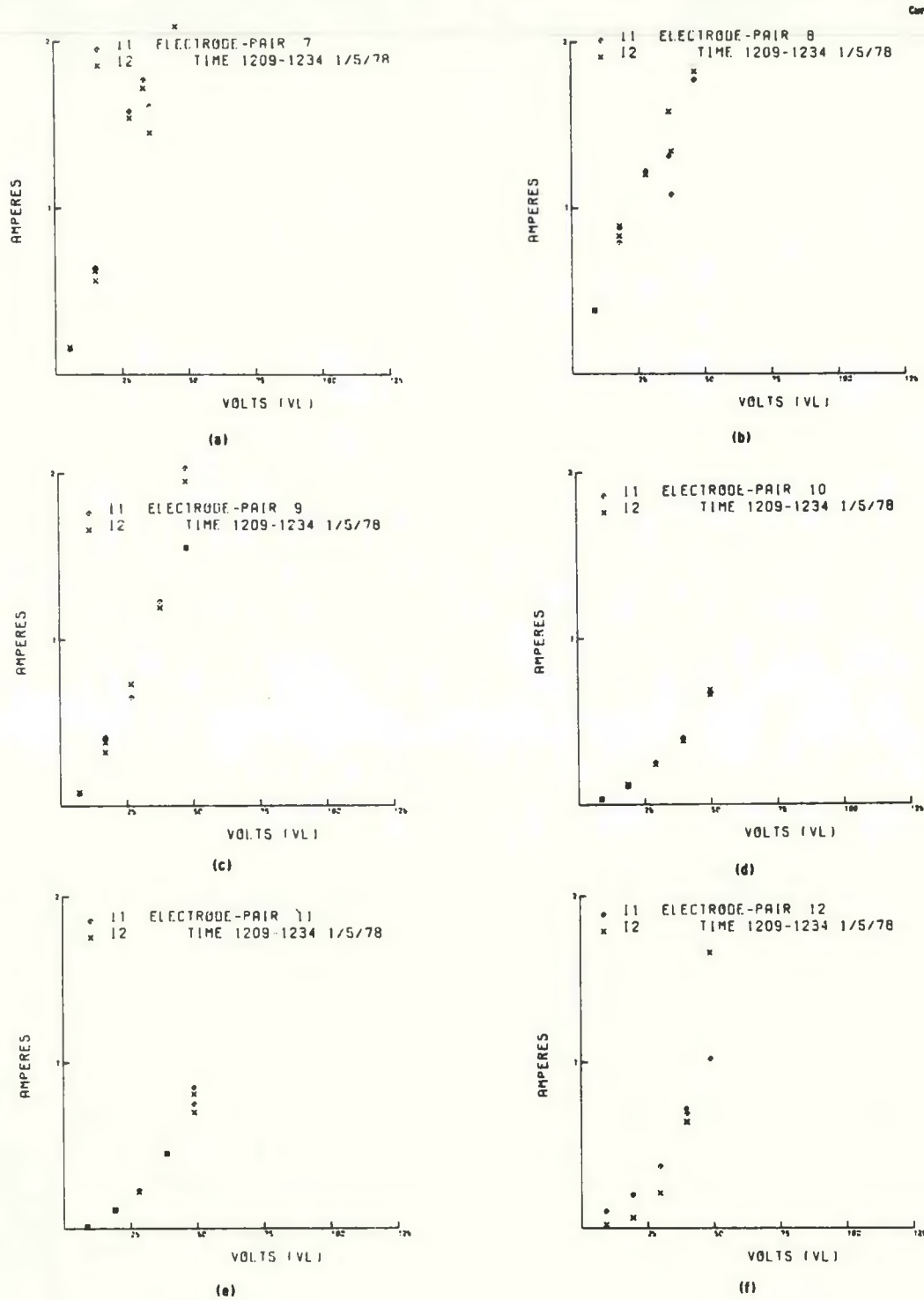

Figure 48. Load Current Versus Applied Voltage V_L Taken During Test 39

$LaCrO_3$ type electrodes. As the I^2R losses decrease, the resistance across the electrodes increase, and the voltage required to pass low current through them increases.

The effect is perhaps better demonstrated by curves in which the voltages required to impress given currents through the various electrode-pairs are plotted as a function of time as the currents are decreased. The data from Figures 45 and 46 are plotted in Figures 49 through 51 as a function of time at which the measurements were made. In all cases, the curve of V_L a function of time has a significantly lower slope than the corresponding current curves.

In most cases as the current is reduced from 5 amperes to 3 amperes, the applied voltage changes very little. In the case of electrode-pairs 4, 5, 7, 9, 10 and 11 some increase in applied voltage is apparent at the current is decreased. (The data were taken with the power supplies in the constant current mode. In this mode, the power supply automatically adjusts the voltage to provide the called for current.)

(C) Measurements of Plasma Conductivity

Plasma conductivities were measured after the 5 ampere life tests at the mid-points and end of the run. As in previous tests, plasma conductivity determinations were made by impressing a voltage between selected upstream and downstream electrodes, that were shorted together. A set of voltage profiles, shown in Figure 52 and 53 were taken as the currents to the two sets of shorted electrodes were recorded.

The current density J in the plasma is obtained by dividing the plasma current by the channel cross-sectional area. The electric field E is obtained from the slope of the voltage profile curves and the knowledge of the electrode pitch. The conductivity is then calculated from the equation $\sigma = \frac{J}{E}$. Plasma conductivities measured in this way represent average values for the channel.

For all of the conductivity measurements made during this test, the second and third electrodes were shorted together to constitute the up-stream electrode and the 10th and 11th electrodes were shorted together to form

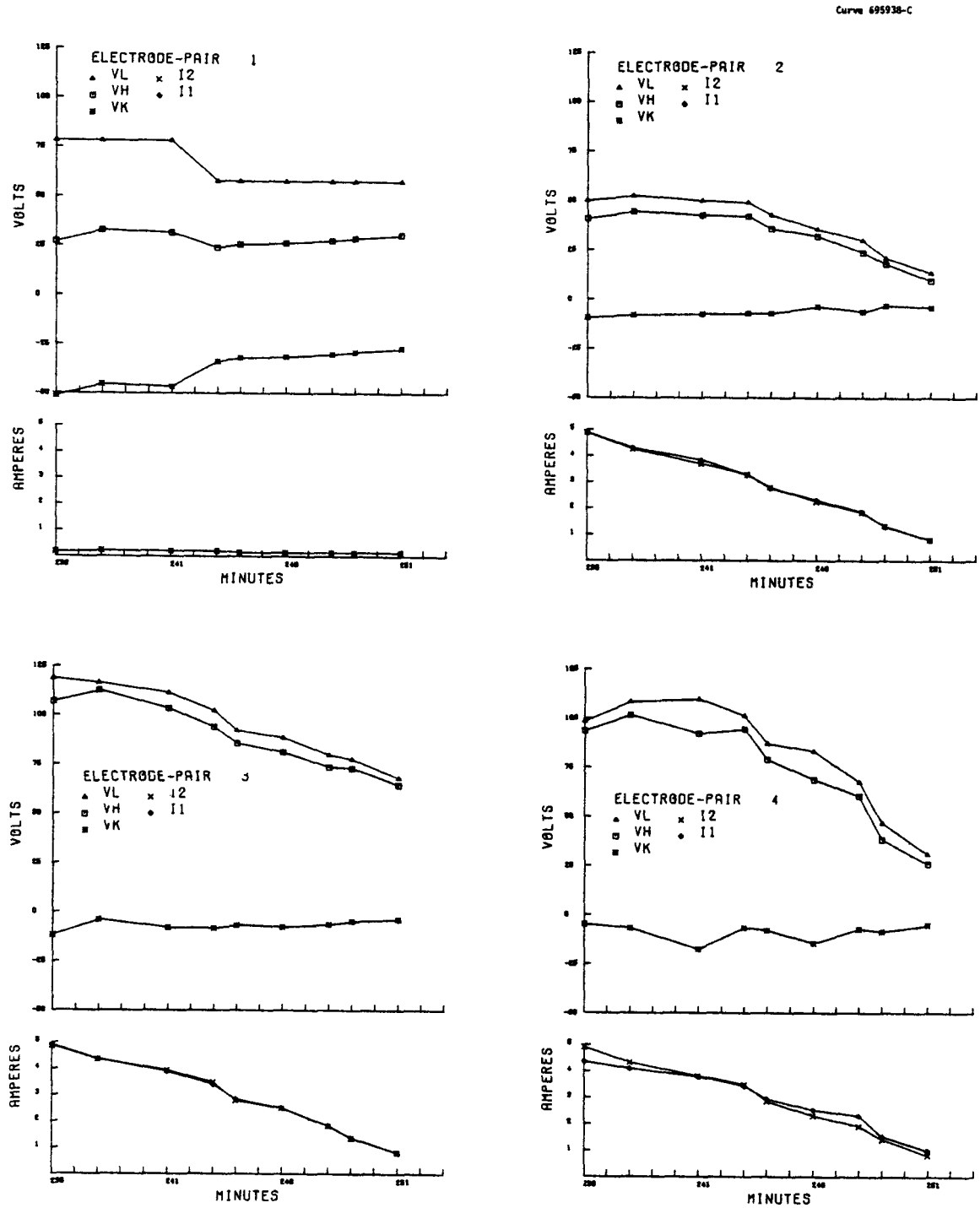

Figure 49. Applied Voltage V_L and Load Current as Function of Time as Load Current is Progressively Decreased, Run 39

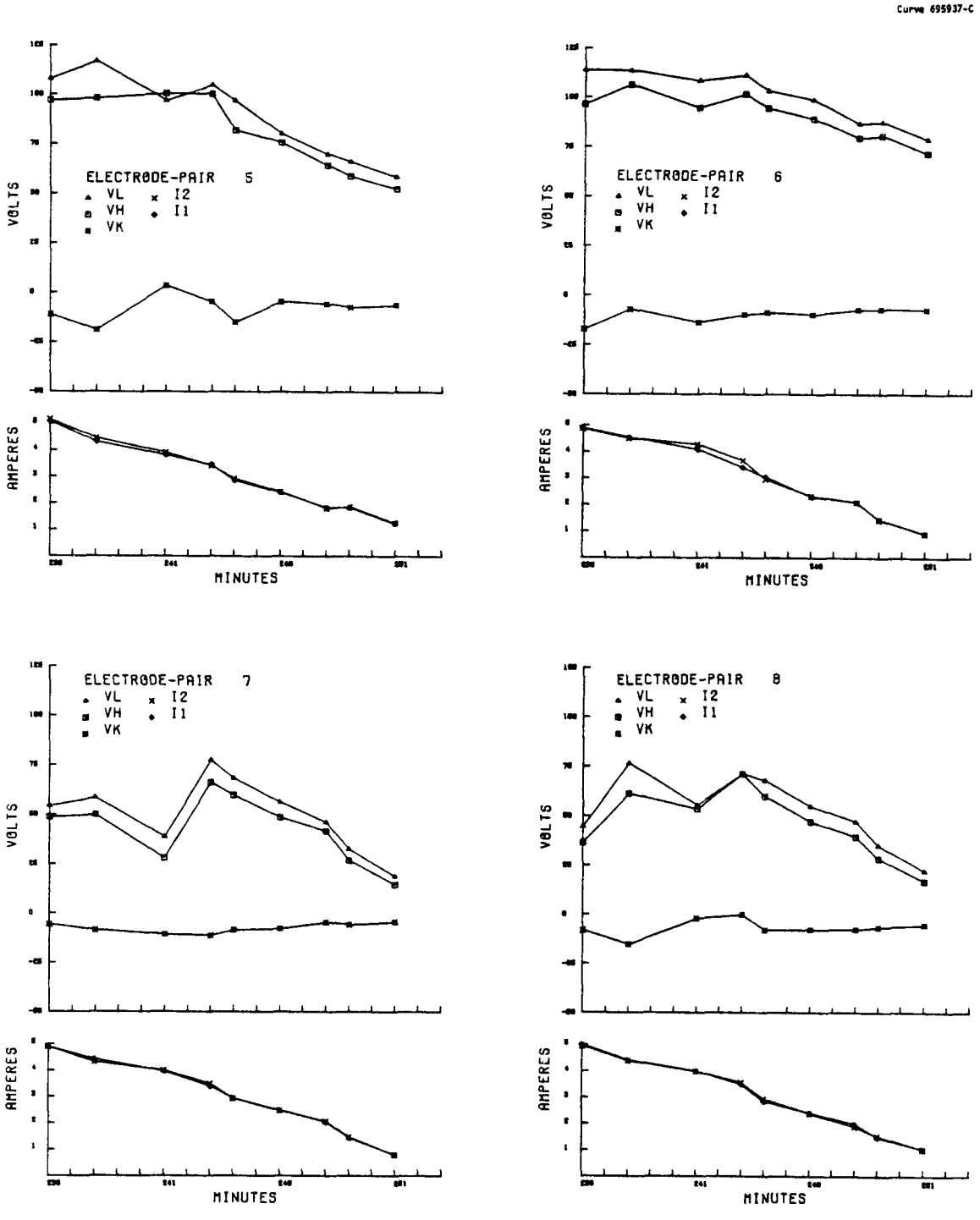

Figure 50. Applied Voltage V_L and Load Current as Function of Time as Load Current is Progressively Decreased, Run 39.

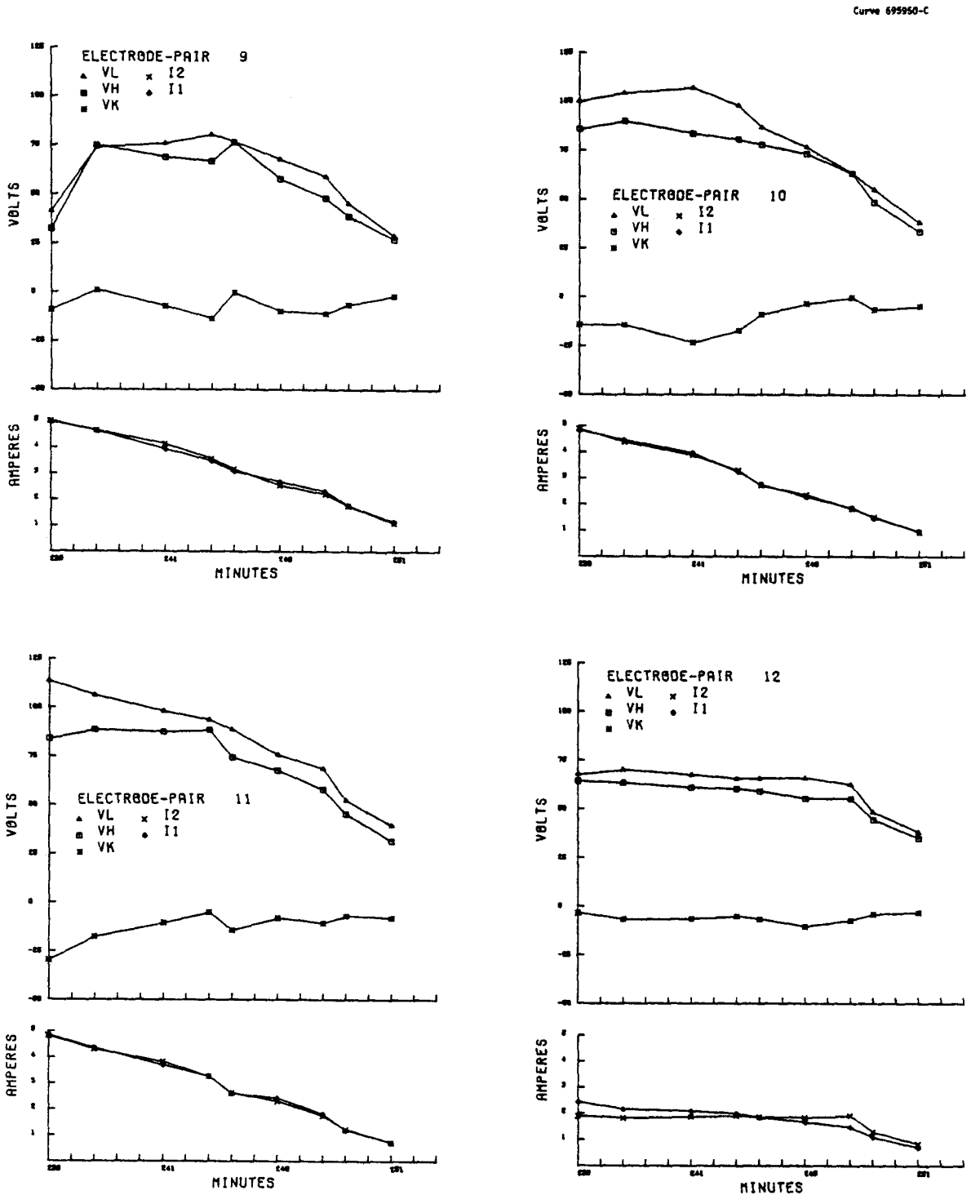

Figure 51. Applied Voltage V_L and Load Current as Function of Time as Load Current is Progressively Decreased, Run 39.

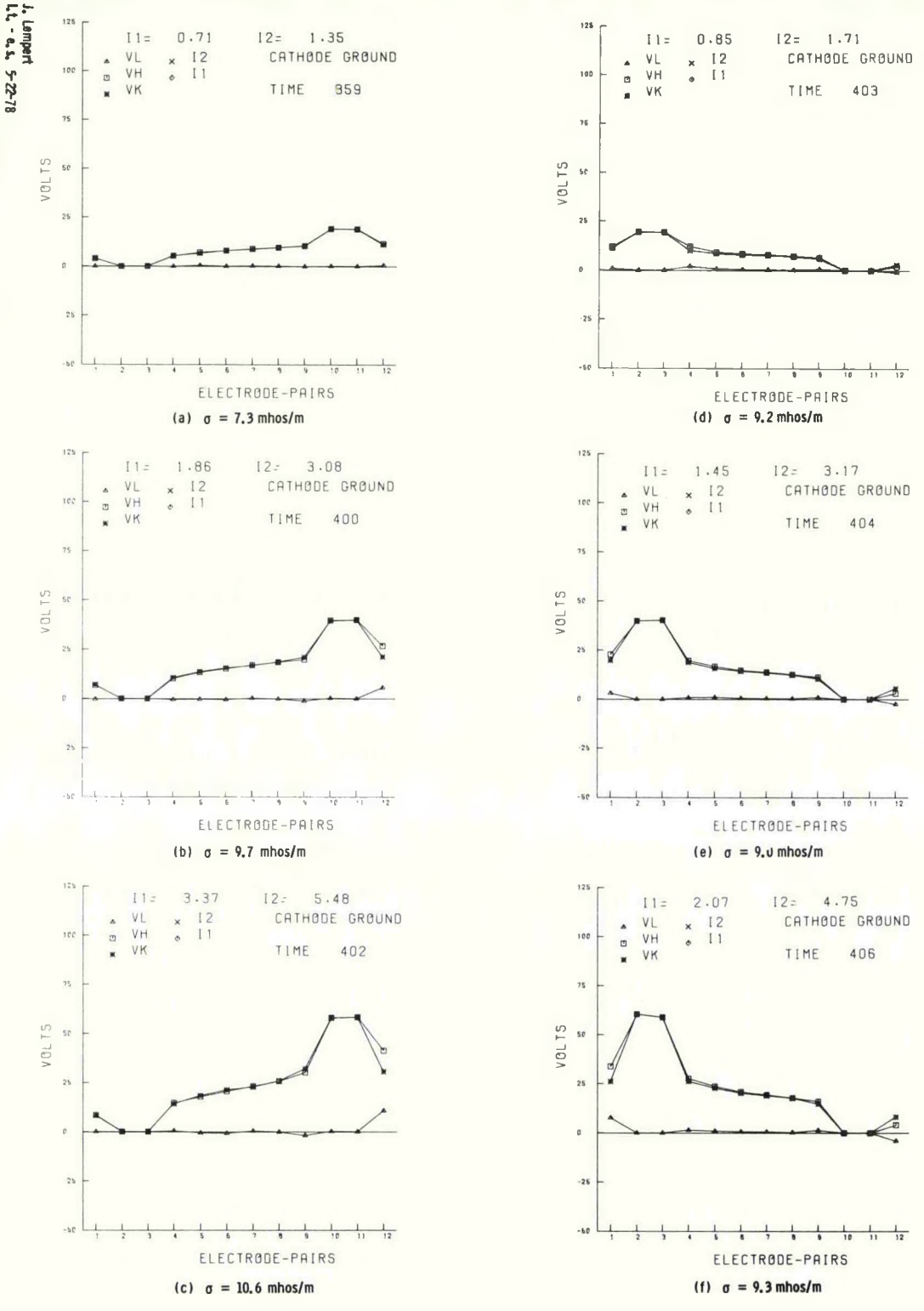

Figure 52. Voltage Profiles Taken During Conductivity Measurements at Mid-Point Tests, Run 39.

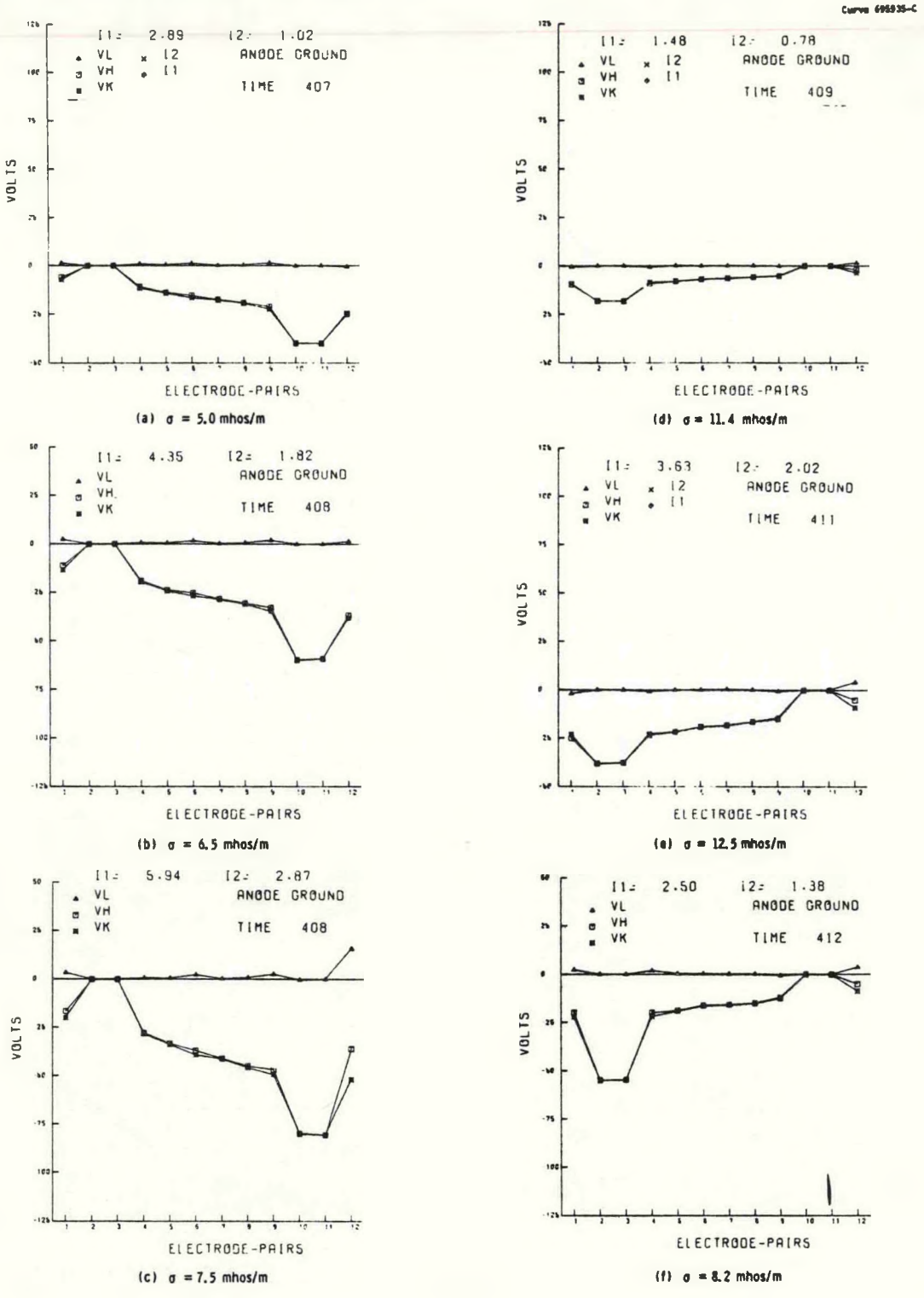

Figure 53. Voltage Profiles Taken During Conductivity Measurements at Mid-Point Tests, Run 39.

the downstream electrode. An axial voltage was applied between the two sets of electrodes. The measurements made to obtain the voltage profiles for Figure 52 used a cathode grounded circuit, i.e., the negative lead to the power supply was grounded. The measurements for the left side of Figure 52 (see (a), (b), and (c)) were made with the upstream electrodes at ground and the downstream electrodes at a positive potential. The data for the right side of Figure 52 were taken with the downstream electrodes grounded and made the cathode, and the upstream electrodes operated at a positive potential. The voltages and plasma currents were progressively increased for both sets of data. The plasma conductivities associated with the voltage profile in Figure 52 are noted below each plot. The data on the left side of Figure 52 shows some increase in plasma conductivity with plasma current. However, the average values of the conductivities taken using the two different techniques were identical, 9.2 mhos/m.

Figure 53 shows the voltage profiles associated with plasma conductivity measurements which were taken with the anode instead of the cathode electrode grounded as it was in Figure 52. The data on the left side of Figure 53 were taken with the upstream electrodes grounded and the downstream electrodes at a negative potential. The data on the right side were taken with the downstream electrodes grounded and the upstream electrodes negative relative to ground. The average of the plasma conductivities on the left side of Figure 53 was 6.3 mhos/m as compared with an average value of 10.7 mhos/m.

Table 11 summarizes all of the plasma conductivity data taken during the mid-point tests. The plasma conductivities determined using three of the four modes of operation described in the table were fairly consistent with each other. However, the plasma conductivities taken between 4:06 and 4:08 hours tended to be significantly lower than the other measurements. These data were taken with the upstream electrodes at ground and the downstream electrodes, which served as the cathodes, at negative potentials. It is likely that the discrepancy was due to changes in plasma conductivity with time rather than on how the electrical connections were made. In support of this thesis, note in the 4:11 and 4:12 time measurements on Table 9 that despite an increase in voltage from -38 volts to -55 volts, the currents

TABLE 11. PLASMA CONDUCTIVITY AND ASSOCIATED DATA TAKEN DURING MID-POINT TESTS ON RUN 39, JAN. 5, 1978

Time Hours, Minutes	Electrode Potential (Volts) E.P. (2 & 3)	Electrode Potential (Volts) E.P. (10 & 11)	Mode of Operation	Currents (Amperes) I_2	Currents (Amperes) I_1	E v/cm Plasma	T mhos/m Plasma	Anode "Fall" Volts	Cathode "Fall" Volts
3 59	G	+19	Cathode Ground	1.35	0.71	0.8	7.3	8.7	5.3
3 59	G	+30	" "	2.19	1.20	1.2	8.0	13.7	8.3
4 00	G	+40	" "	3.08	1.86	1.5	9.7	19.4	10.5
4 02	G	+48	" "	3.99	2.29	1.8	10.2	23.5	12.4
4 02	G	+58	" "	5.48	3.37	2.5	10.6	27.0	14.5
4 03	+20	G	" "	1.71	0.85	0.7	9.2	8.4	6.3
4 04	+31	G	" "	2.55	1.19	1.0	9.3	15.0	9.1
4 04	+40	G	" "	3.17	1.45	1.3	9.0	20.9	10.9
4 05	+50	G	" "	3.79	1.74	1.4	9.4	29.0	12.9
4 06	+60	G	" "	4.75	2.07	1.7	9.3	33.3	15.4
4 06	G	-20	Anode Ground	0.42	1.41	0.8	4.3	4.5	10.2
4 07	G	-40	" "	1.02	2.89	1.6	5.0	11.2	18.2
4 08	G	-60	" "	1.82	4.35	2.2	6.5	19.3	25.8
4 08	G	-80	" "	2.87	5.94	3.0	7.5	28.2	32.1
4 09	-18	G	" "	0.78	1.48	0.5	11.4	5.2	9.4
4 11	-38	G	" "	2.02	3.63	1.25	12.5	14.7	14.9
4 12	-55	G	" "	1.38	2.50	1.3	8.2	12.2	34.1
Avg.							8.7		

dropped. Thus the drop in plasma conductivity observed at 4:12 appears to be correct. Note in the Table that the increase in voltage is entirely absorbed in the "cathode fall".

Figure 54 shows the variation in plasma conductivities and currents as a function of time. While there appears to be some evidence that there is a proportional relationship between plasma conductivity and plasma current, the data are not conclusive. A dependence of plasma conductivity on plasma current might be expected on the basis of the Kerrebrock non-equilibrium ionization effect in which the plasma is heated by the impressed current. However, the current densities in the plasma are probably too low for this effect to occur.

The plasma fields shown in Table 11 range from .75 volts/cm to a maximum of 3 volts/cm. These axial fields are relatively modest compared to Hall fields which may be as high as 20 to 30 volts/cm.

In the calculations of conductivity, the plasma current is assumed to be the smaller of the two currents shown in Table 11. In the previous quarterly report, it was shown that the larger current is associated with leakage currents from ground to electrodes which are off-ground potential. The difference between the two currents is the leakage current from these "hot" electrodes to ground. It is believed that a substantial fraction of this leakage current goes through the plasma to electrically grounded regions of the system which are both upstream and downstream from the test channel. The basis for this conclusion will be discussed in the next section.

In Table 11, it will be noted that the higher electrode current, whether I_2 or I_1, and the higher electrode "falls", whether anode or cathode, are always associated with electrodes which are ungrounded in the conductivity tests. This is due to the leakage currents through the plasma which impose additional loads on the ungrounded electrodes.

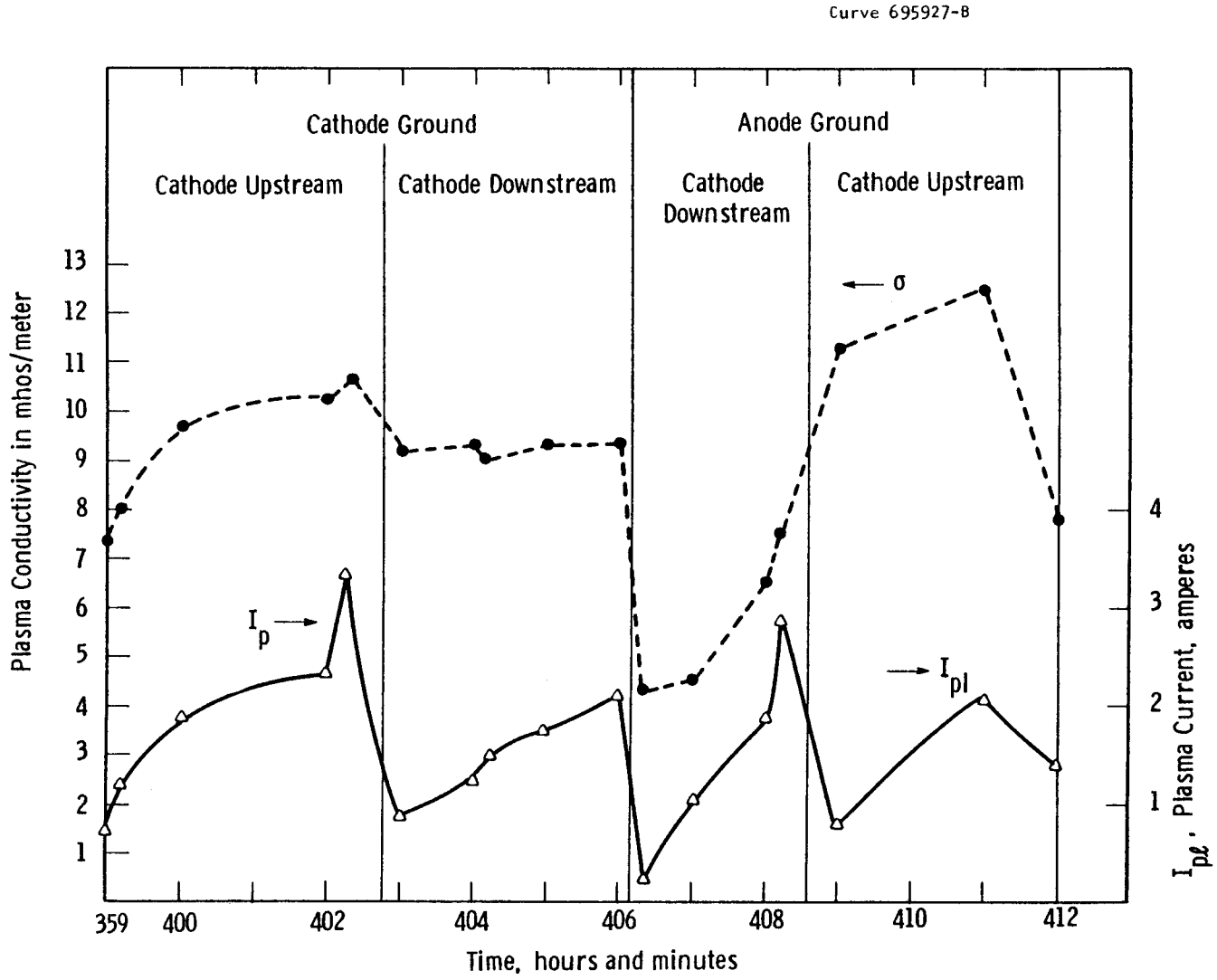

Figure 54. Measured Plasma Currents and Calculated Plasma Conductivities as Function of Time, Run 39, As Applied Voltage is Increased.

In Figures 52 and 53, it is apparent that the voltage profile curves are characterized by a region of constant slope in the center of the curves and by a sharp increase in slope at the anodes and cathodes. While these terminal voltage differences are referred to as anode and cathode falls, in the next section we will show that the the higher voltage requirements at the anodes and cathodes do not necessarily represent the usual type of cathode or anode falls, but more likely are the voltages required to produce changes in the trajectories of the plasma charges as they change from a flow parallel to the channel axis to a transverse flow to permit their collection by the electrodes.

Table 12 summarizes a similar set of conductivity data taken at the end of run 39. The conductivities measured at the end of the test were significantly lower than the ones taken in the middle of the test. The average plasma conductivity at the end of the test was 4.5 compared to the average of 8.7 mhos/m taken during the mid-point tests. The lowest conductivities in both instances were measured under anode-grounded conditions with the cathode electrode at the downstream end of the channel.

(D) Determination of Equipotential Contours for Proof Test 2.

One of the advantages of knowing the potential contours of a channel in which external voltages are used to simulate MHD loading, is that the trajectories for the transport of charge coincide with the electric field lines, which are perpendicular to the equipotential lines. This is not the case for a high vacuum device. Thus, a knowledge of the equipotential lines provides significant information on the direction of charge flow within the channel. The equivalent of this information per standard MHD operation is the knowledge of the vector sum of the $\overline{U} \times B$, the $\overline{v} \times B$, and the electric field for a given channel, where $\overline{U}$ is the gas velocity in the axial direction and $\overline{v}$ is the charge drift velocity. A voltage profile curve from Proof Test 2 (Figure 76 f, Reference 1) was used to test this relationship. A W proprietary computer program (Reference 6) was employed to solve LaPlace's equations with experimentally determined potentials substituted as boundary conditions in a configuration scaled to match the channel cross-section. Figure 55

TABLE 12. PLASMA CONDUCTIVITY AND ASSOCIATED DATA TAKEN AT END OF RUN 39

Time Hours, Minutes	Electrode Potential (Volts) E.P. (2 & 3)	Electrode Potential (Volts) E.P. (10 & 11)	Mode of Operation	Currents (Amperes) I_2	Currents (Amperes) I_1	E v/cm Plasma	T mhos/m Plasma	Anode "Fall" Volts	Cathode "Fall" Volts
13 17	G	8.8	Cathode Ground	.66	.27	.48	4.3	1.6	3.9
13 18	G	30.1	" "	2.28	.68	1.5	3.6	6.8	13.4
13 18	G	49.3	" "	3.64	.87	2.2	3.1	12.1	22.3
13 19	G	75.2	" "	6.55	1.16	4.2	2.1	17.4	29.1
13 20	7.9	G	" "	.38	.17	.14	9.8	5.8	1.1
13 21	30.3	G	" "	1.24	.51	.47	8.4	24.2	2.7
13 22	50.7	G	" "	1.83	.80	.88	7.0	40.4	4.3
13 22	76.8	G	" "	3.35	1.45	1.75	6.4	56.9	8.0
13 23	96.2	G	" "	8.17	2.89	3.5	6.4	60.4	11.5
13 25	G	- 8.8	Anode Ground	.07	.62	0.4	1.4	2.7	3.3
13 25	G	-30.1	" "	.44	2.36	1.5	2.3	10.7	9.4
13 26	G	-51.7	" "	.69	4.02	2.7	2.0	20.1	13.6
13 27	G	-81.8	" "	1.34	8.26	2.9	3.5	36.6	21.4
13 28	-30.1	G	" "	,32	2.15	1.1	2.2	3.6	38.9
Avg.							4.5		

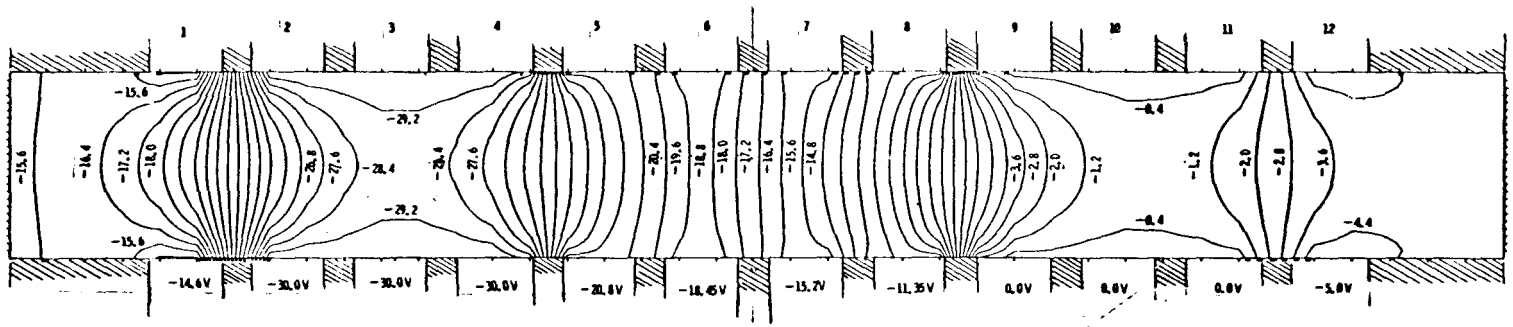

DIGIT CONTOUR

1	-.30000+02	21	-.14000+02
2	-.29200+02	22	-.13200+02
3	-.28400+02	23	-.12400+02
4	-.27600+02	24	-.11600+02
5	-.26800+02	25	-.10800+02
6	-.26000+02	26	-.10000+02
7	-.25200+02	27	-.92000+01
8	-.24400+02	28	-.84000+01
9	-.23600+02	29	-.76000+01
10	-.22800+02	30	-.68000+01
11	-.22000+02	31	-.60000+01
12	-.21200+02	32	-.52000+01
13	-.20400+02	33	-.44000+01
14	-.19600+02	34	-.36000+01
15	-.18800+02	35	-.28000+01
16	-.18000+02	36	-.20000+01
17	-.17200+02	37	-.12000+01
18	-.16400+02	38	-.40000+00
19	-.15600+02	39	.40000+00
20	-.14800+02	40	.12000+01

Figure 55. Equipotential Lines Associated with Typical Plasma Conductivity Measurement. I_2 = 5.82 Amperes, I_1 = 5.28 amperes.

gives the equipotentials, divided into 0.8 volt steps, associated with a conductivity measurement made during Proof Test 2. The grid in the y direction, across the channel corresponds to a 1 mm spacing. The grid in the x axial direction corresponds to a 5 mm spacing. Because of the rather coarse mesh used in the initial plot the equipotential mapping was evidently not perfect. For example, all of the equipotentials except the one matching the determined electrode potentials should bend and terminate at right angles to the insulator member, which is the cross-hatched item on Figure 55. Greater accuracy could have been achieved by going to a finer mesh. However, the plot is accurate enough to enable some interpretation of the physical phenomena associated with conductivity measurements.

In the conductivity measurement being discussed, the field was determined essentially by measurement of the potentials of the intermediate electrode pairs 6, 7 and 8 and correcting for the electrode pitch. From Figure 54, it is evident that this procedure should provide a reasonable approximation to the magnitude of the plasma electric field.

In the example of Figure 55 electrons leave the cathode (electrode-pairs 2, 3, and 4) and travel in trajectories which are perpendicular to the equipotentials they are traversing. It is evident that the higher fields at the anode and cathode are related to the required change in trajectories of the electrons as they leave the cathode and as they bend back to the anodes.

From the equipotential plot, it is clear that electrons which are thermionically emitted from electrode 2 and the upstream half of electrode 3 will travel upstream towards some distant electrically grounded region. From the higher field in the upstream direction, it is surmised that the plasma current upstream is actually higher than the plasma current downstream which contributes to the plasma conductivity measurement. According to the measurement, I = 5.28 amperes and I_2 = 1.82 amperes. The total leakage from the cathode electrod (consisting of electrode-pairs 2, 3 and 4) is equal to 5.28 - 1.82 = 3.46 amperes. The plasma current is assumed to be 1.82 amperes. Apparently a

significant fraction of the 3.46 amperes leakage current consists of current through the plasma to the grounded flanges between the channel and the combustor and possibly to the combustor proper.

Examination of the equipotentials at the other grounded end of the channel indicates that there is no possibility of leakage current down the channel since a retarding field is present.

One of the reasons the equipotentials were plotted was to try to explain how it was possible for electrode pair 12 to assume a negative potential, since these electrodes are on the other side of the grounded electrode configuration. The indications are that electrons going down the center of the channel have enough diffusion energy to charge the electrons of electrode-pair 12 to a negative 5 volts.

The computer program employed permits introducing different zones of plasma conductivities. Using this program, it is thus possible to take into account the cooler region of the plasma adjacent to the electrodes. A resistive slag layer can also be included. Our present plans are to apply the equipotential plotting technique to determine the electrical fields associated with simulated life test procedures. The charge trajectories associated with applying combination transverse and axial fields under combined axial and transverse fields can thus be investigated. We have come to the conclusion that it is necessary to apply axial fields in the simulated channel tests in order to evaluate the quality of the insulation under conditions which approximate the Hall fields set up during normal operations of conventional MHD generator.

Performance of Materials (Proof Tests 1 through 3)

The post-test analysis of all materials was conducted at Battelle Pacific Northwest Laboratories and at the National Bureau of Standards. Electrodes and insulators were examined using SEM/EDX and X-ray diffraction methods. Low magnification (< 500x) optical viewgraphs were used for orientation purposes

and for detecting gross features such as bond detachments. The following summarizes the state of materials after a 20 hour proof test. The performance of materials is largely based on the amount of degradation (or change in structure, chemistry, properties) during the test. A summary of the eleven electrode materials and five insulator materials are shown in Table 13.

$La_{.95}Mg_{.05}CrO_3$ Electrodes ($MgAl_2O_4$ Insulators)

All three $La_{.95}Mg_{.05}CrO_3$ anodes, after visual inspection, appeared to have withstood the proof test well (See Figure 56a). All were intact and showed little erosion, reaction or fracturing. Each anode did possess a dark band (~1 mm thick) at the surface exposed to the hot plasma. SEM/EDX examination showed that this region was denser than the material below it and that it contained Si. It appears that the Si (as SiO_2) contributed to the densification of this 1 mm thick layer on the exposed surface of the anode.

Examination of the entire width and length of the anode reavealed a Mg-Cr phase, and to a lesser extent a Mg-Cr-Si phase. As one moves from the bottom of the anode to the top or from the edge to the anode toward the center, the occurrence of these secondary phases decreases. Assuming that the insulators provide some cooling to the anode, the occurrence of these phases appears to decrease with increasing operating temperature. There is also some indication that accompanying the decrease in the occurrence of secondary phases there is an increase in porosity.

The insulator on each side of the anode showed very little degradation. Some K and Zr were found along the interface of the insulator and anode. However, little penetration of the K into the insulator was observed.

Optical examination of the cathodes revealed more cracking and reaction products than on the anode side. Figure 56b shows a cathode which was subsequently examined by SEM/EDAX techniques. This examination indicated that the cathode surface region near the plasma surface and insulator contain a complicated phase, containing Mg, Al, Si, Cl, K, La, Cr, and Ni, that has reacted with the $LaCrO_3$. Also, it was difficult to locate and identify any second Mg-Cr spinel phase in the cathodes.

TABLE 13

PHASE III U-02 PROOF TEST MATERIALS

Electrodes	Total Porosity (%)	Open Porosity (%)	Interelectrode Insulator	Proof Test #
3 $MgAl_2O_4$-1 Fe_3O_4 (PS)	10	4	$MgAl_2O_4$(S)	1
4 $MgAl_2O_4$-1 Fe_3O_4 (S)	~5	<1	$MgAl_2O_4$(S)	1
3 $MgAl_2O_4$-1 Fe_3O_4 (PS)	10	4	$MgAl_2O_4$(PS)	3
$La_{.95}Mg_{.05}CrO_3$ (S)	4	0	$MgAl_2O_4$(S)	2
$La_{.95}Mg_{.05}CrO_3$(S)-GE	10-15	?	$MgAl_2O_4$(S)	3
$La_{.95}Mg_{.05}CrO_3$/88 ZrO_2-12 Y_2O_3 composite (HP)	7	2	$MgAl_2O_4$(S)	2
$La_{.95}Mg_{.05}Cr_{.9}Al_{.1}O_3$ graded to 85 ZrO_2- 12 CeO_2-3 Y_2O_3 (HP)	4	<1	MgO (S)	2
$La_{.95}Mg_{.05}CrO_3$ graded to 85 ZrO_2-12 CeO_2-3 Y_2O_3 (PS)	10-20	5-10	$MgAl_2O_4$(PS)	2
$La_{.95}Mg_{.05}Cr_{.85}Al_{.15}O_3$ graded to $La_{.95}Mg_{.05}Cr_{.68}Al_{.32}O_3$ (HP)	5	<1	MgO (HP)	3
50 $LaCrO_3$-50 $SrZrO_3$ (S)	11	8	$MgAl_2O_4$(S)	3
HfO_2-CeO_2-(Y_2O_3) (HP)-ANL	?	?	$MgAl_2O_4$ (PS)	1
Insulators				
MgO (S)	2	0.5	--	2
MgO (HP)	16	12	--	3
$MgAl_2O_4$ (S)	2	0.5	--	1,2,3
$MgAl_2O_4$ (PS)	5-10	3-5	--	2,3
$MgAl_2O_4$ (S) - GE	?	?	--	1,3

P - Arc plasma sprayed, S - Sintered, HP - Hot Pressed

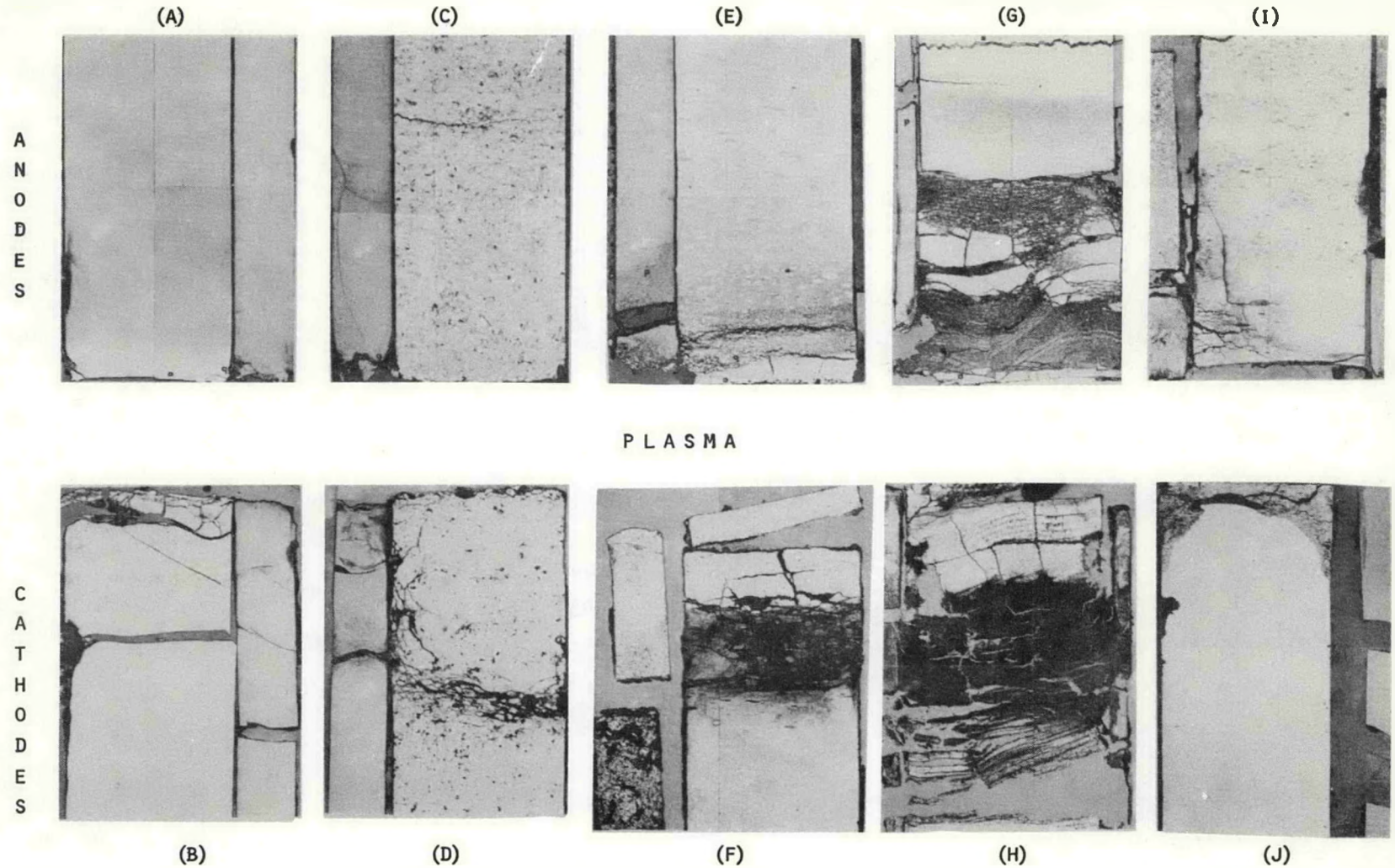

Figure 56. Cross-Sections of Several $LaCrO_3$-Based Electrodes After 20 Hour Proof Test; (A,B) $La_{.95}Mg_{.05}CrO_3$, (C, D) $La_{.95}Mg_{.05}CrO_3/Y_2O_3$ Stabilized ZrO_2 Composite, (E, F) Hot Pressed ZrO_2-CeO_2-Y_2O_3 'Capped' $La_{.95}Mg_{.05}Cr(Al)O_3$, (G, H) Arc Plasma Sprayed ZrO_2 'Capped' $LaCrO_3$, (I, J) Graded $La_{.95}Mg_{.05}Cr_{1-x}Al_xO_3$. (X2.5)

Cracks in the cathode insulators were high in K-Mg-Al phases. Either these cracks provide easy diffusion paths for the formation of these new phases, or the cracks were the result of weakening by some phase reaction.

Hot Pressed $La_{.95}Mg_{.05}CrO_3/ZrO_2$ Electrodes ($MgAl_2O_4$ Insulators)

These electrodes were generally in good condition after the proof test with the anode ceramics in better condition than the cathode ceramics (see Figures 56c,d and 57.) About the only signs of degradation in the anodes occurred in the top 2 mm, where increased porosity and development of voids at zirconia grain boundaries (Figure 57) were noted. Grains of zirconia protruding into the plasma had compositions identical with those further inside the electrode. A thin crust of (La, Cr) oxide at the plasma interface showed significant Cr-depletion and Si-enrichment.

Closer examination of the outer most part of the anode revealed a zone ~200 μm wide within which the lanthanum is distributed in more than one phase. In this region, at least three La-rich phases appear to be present: a La, Zr-rich phase with equant outlines, a La, Cr phase (some Si) and a La, Si phase (depleted Cr).

A closer look at the area of high porosity and grain boundary enlargement is given in Figure 57. These regions contain no detectable K. The remaining non-porous areas with tight grain boundaries away from the plasma surface are characterized by the presence of (Mg, Cr) oxide in the $LaCrO_3$ matrix.

As is visible in Figure 56c, the top of all anode insulators is characterized by recession on the sides, adjacent to the electrodes, leaving an "island" of insulator protruding from the surface at the center. The very surface of the "island" is an area of densely recrystallized $MgAl_2O_4$ with few other elements. Further inward a zone of high porosity is evident. Throughout a zone extending across the spinel slab below the "island" are patches of spinel intergrown with (Zr, Ca, La) oxide. Potassium is conspicuously lacking in nearly all anode insulator spectra taken.

In $LaCrO_3/ZrO_2$ composite cathodes (see Figure 56d) certain features suggestive of degradation are apparent: (1) a reworked surface zone at the plasma interface

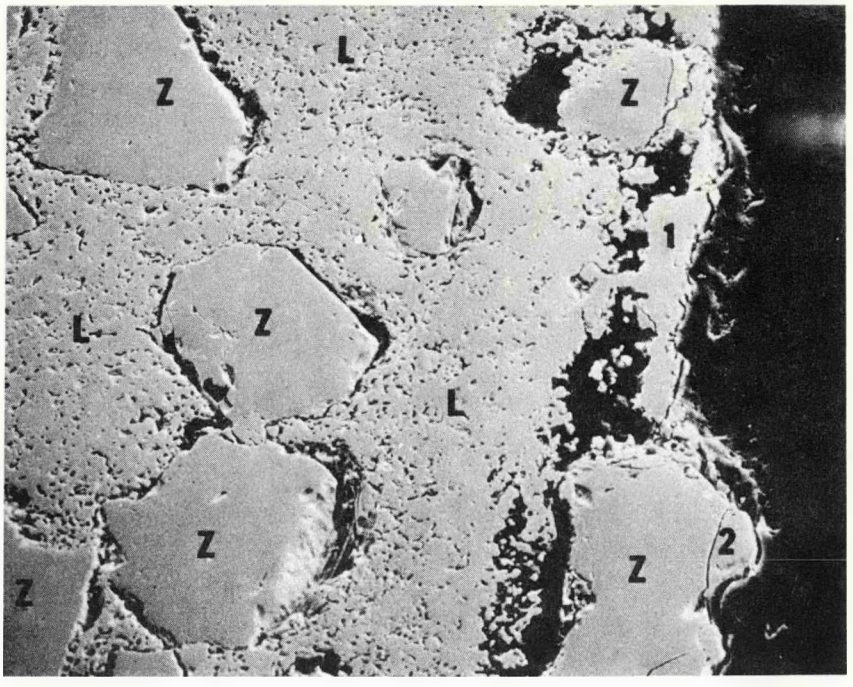

Figure 57. Microstructure of $LaCrO_3/ZrO_2$ Composite Near Plasma Surface. Area 1 is $LaCrO_3$ Deficient in Cr while Area 2 is a ZrO_2 Grain that had been Exposed to Plasma Showing no Preferential Loss of Y_2O_3. (X75)

~0.5 mm thick with voids suggestive of zirconia destruction; (2) an outer zone 1-2 mm thick in which the $LaCrO_3$ matrix is relatively porous and voids occur around the edges of the zirconia grains; (3) a weakened area along a curved series of cracks extending inward from the insulator downward and into the center of the electrode.

The reworked outer surface layer contains significant amounts of K. The outermost part of this reworked zone consists of a 50 μm thick crust of dense, nearly pure $LaCrO_3$ (with a slight surface depletion of Cr).

In the second zone, characterized by higher porosity and voids about the ZrO_2, K is found in the voids only. Adjacent to the ZrO_2 in some instances are segregations of a Cr-rich phase. Similar porous areas also occur locally further in toward the interior of the electrode. Dense areas contain numerous inclusions of (Mg, Cr) oxide, by contrast with porous areas, which contain few. Other than the large voids occurring around the zirconia grains in the outer zone, the porous areas contain little potassium.

The weakened areas near the center of the electrode 6-10 mm from the surface are associated with a series of cracks which curve upward to merge with the cracked altered zone in the insulator~4-6 mm from the surface (see Figure 56d). This feature probably coincides with isothermal surfaces below the seed concentration isotherm. The weakened areas are characterized by low mechanical strength, resulting in poor polishing properties, abundant K and high porosity in the $LaCrO_3$ matrix. It is apparent for the smaller grain size in this area that the $LaCrO_3$ grains have partially dissolved into the seed.

The ceramic just above the lead-out has less locally developed porosity, and in general is relatively dense. It contains (Mg, Cr) oxide inclusions, as well as significant K, presumably associated with the local development of the porous structure.

Single cracks extending completely across the $MgAl_2O_4$ spinel occur both in the upper third of the insulators and in the lower third adjacent to the copper.

Adjacent to the cracks, alteration appears to be significant only about those which occur 4-6 mm from the top edge. Such alteration is characterized primarily by an increased potassium content associated with the high porosity. Most of the potassium appears to be present as K_2CO_3. Similar alteration occurs in the necked-in zones near the top of the insulator slab, where more detailed examination reveals the presence of potassium in the form of intergranular potassium aluminate.

At the outer surface of the insulator a zone of densely recrystallized spinel extends inward a distance of ~150 μm. The recrystallization has been associated with formation of an intergranular potassium aluminosilicate phase. Inward from the recrystallized outer layer, potassium is present but largely as a K-rich phase, presumably K_2CO_3. The amount of potassium decreases steadily inward, falling off to nearly zero at a distance of 1 mm (except locally near the fracture zone a third of the way down).

Hot Pressed ZrO_2 Capped $LaCrO_3$ Electrodes (MgO Insulators)

The chemistry of the hot-pressed ZrO_2 capped electrodes is more complex than the electrodes described above. These electrodes, as fabricated, consisted of the following four layers: (1) 1 + mm 'cap' of 85 m/o ZrO_2-12 m/o CeO_2-3 m/o Y_2O_3, (2) 1 mm layer of 66 v/o ZrO_2 'cap' composition--34 v/o $LaCrO_3$, 'body' composition, (3) 1 mm of 34 v/o ZrO_2 'cap' composition - 66 v/o $LaCrO_3$ 'body' composition, and (4) the remaining thickness of $La_{.95}Mg_{.05}Cr_{.9}Al_{.1}O_3$. Secondly, the vendor found it necessary, in order to achieve high densities and to match thermal expansion coefficients, to use a $LaCrO_3$ 'body' composition which consisted of a mechanical mixture of two $LaCrO_3$-based powders. As seen in Figure 58, these powders were poorly mixed, resulting in a $LaCrO_3$ 'body' that consists of dense $La_{.95}Mg_{.05}Cr_{.5}Al_{.5}O_3$ domains within a more porous $La_{.95}Mg_{.05}CrO_3$ matrix. Within the dense domains, fine intergrowths rich in Mg and Al were also identified. Powder X-ray diffraction analysis indicated the presence of a spinel-type phase having a cubic cell dimension between pure $MgAl_2O_4$ and $MgCr_2O_4$. The microstructure and microchemistry of the two zones consisting of mixtures of $LaCrO_3$ and ZrO_2 were also extremely variable (but consistent), indicating a lack of adequate processing control in fabrication. Microcracks were present in the upper three layers of the as-fabricated electrode blocks. After the proof test the number and size of these cracks had increased.

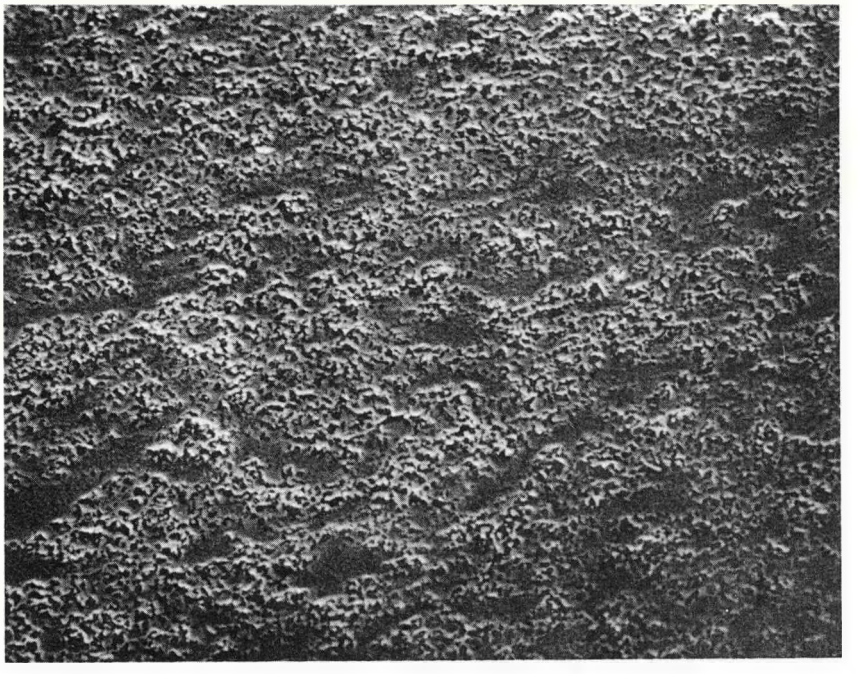

Figure 58. Microstructure of $LaCrO_3$ Base of ZrO_2 'Capped' Electrode Showing Dense Al-Rich Domains in Porous Al-Deficient Matrix (X620)

These electrodes were the first set of electrodes in the test section and experienced surface temperatures of 1850 $\pm$ 50°C and severe contamination by upstream components. Major contaminants include Zr, Ca, Mg, Si and Ni. In fact, the anodes had an adherent 'replenished' CaO (MgO) stabilized ZrO_2 'cap'. Potassium in the upper three zones was usually associated with these contaminants and with the secondary phases found in the as-fabricated samples. Extensive corrosion of anodes and anode insulators by potassium was, in general, not evident; the exception is the presence of potassium with the above mentioned phases. Cracking of MgO insulators is the primary mode of degradation on the anode wall. Also, the diffusion of Cr into MgO and deposition of droplets from upstream components with subsequent melting are secondary, though not serious sources of degradation.

The MgO insulators on the cathode wall, on the other hand, are intruded by seed in the liquid seed temperature region. The swelling of the lower portion of the MgO insulator in Figure 56f is due to seed intrusion and subsequent hydration. The dissolution of magnesia grains by liquid seed is evident under the SEM.

These ZrO_2 capped cathodes are characterized by extensive reactions with seed. The zirconia cap itself shows little evidence for any extensive reactions. The middle two zones show two dominant chemical reactions: (1) reaction of K with available impurity phases and the Mg-Al-Cr rich phase possibly to form fluid phases which enhance corrosion and/or porosity, and (2) reaction of K to form stable compounds with the zirconia phase containing ceria. Powder X-ray diffraction reveals the formation of the perovskite, $KCeZr_2O_6$. This phase was also found in the post-test analysis of Zr-$_2$-CeO_2 cathodes from the Phase I U-02 modules (Reference 7). Corrosion by liquid seed is most severe in the dark, fissured region consisting of the upper few mm of the '$LaCrO_3$' body. Rounded $LaCrO_3$ particles of reduced size are surrounded by a dark 'sea' of extremely K-rich material containing La, Cr plus lesser amounts of Mg, Al and Si. $LaCrO_3$ is undergoing extensive solution by seed. Below the large horizontal crack at the bottom of this dark zone (see Figure 56f) the $LaCrO_3$ ceramic is unaltered although uncombined seed oozes from the pores making SEM/EDX analysis most difficult.

Arc Plasma Sprayed ZrO_2 Capped $LaCrO_3$ ($MgAl_2O_4$ Insulation)

Test data indicated these electrodes performed well during the 20-hour proof test. Only the inter-electrode insulation was inferior to other electrode systems. Their appearance upon initial post-test inspection looked good despite the loss of most of the ZrO_2 'caps'. However, after the inadvertent exposure to water both anodes and cathodes swelled badly. In fact, swelling continued even after casting in epoxy. These electrodes suffered from two features which caused this gross damage. First, these electrodes could only be produced with densities 80-90 percent of theoretical density with 5 to 10 open porosity. Thus the material is very susceptible to seed penetration with subsequent hydration and swelling. Secondly, the as-sprayed material shows considerable variation in La/Cr ratio, often being La rich and Cr deficient. $La(OH)_3$ was identified by X-ray diffraction. The swelling of the anodes is due to the hydration of La_2O_3. Because a control sample was not available it remains unclear how much lanthana was in the original sample and how much resulted from other potential reactions during testing (vaporization of Cr, fluxing by seed, etc.).

$LaCrO_3$-$LaAlO_3$ Electrodes (MgO Insulators)

From the post-test visual examination, these electrodes appeared in good condition. Examination of cross-sections (Figures 56i, j) generally confirmed this evaluation. The upper 5.0 mm of these electrodes consisted of a mixture of two powders, $La_{.95}Mg_{.05}Cr_{.85}Al_{.15}O_3$ and $La_{.95}Mg_{.05}Cr_{.5}Al_{.5}O_3$, which are not well mixed. As with the hot-pressed ZrO_2 capped $LaCrO_3$ electrodes, domains of each composition exist as well as non-homogenetics in the $LaCrO_3$ 'base', (which consisted of $La_{.95}Mg_{.05}Cr_{.85}Al_{.15}O_3$. Also, a second phase of Mg and Al with some Cr is found in the high Al domains. In the cathodes, potassium has preferentially reacted near the plasma surface (see Figure 56j) with both the low Al $LaCrO_3$ domains and with the Mg, Al second phase in the high Al $LaCrO_3$ domains. Fine porosity and potassium are found throughout this zone. The remainder of this cathode is virtually unreacted. In fact, the cooler portions of the anodes contain more K than the cathodes; usually in regions rich in Cr_2O_3. The porous (15% porosity) MgO which was used in Phase I and Phase II U-02 tests, showed extensive reactions with seed (see Figure 56j).

$SrZrO_3$ - $LaCrO_3$ Electrodes

These electrodes reacted badly, particularily the anodes. Reactions were too numerous to mention in detail, however, most were related to the poor homogenity and poor densification of the original material. Due most likely to relatively high initial porosity, anodes and cathodes suffered from corrosion by seed; anodes also appeared to run much hotter than cathodes, further intensifying reactions. K-related reactions were more severe on cathodes. The chrome-oxide component of cathode ceramics was leached/vaporized selectively to yield phase assemblages composed of refractory La_2O_3 ($La(OH)_3$, after cool-down), $La_2Zr_2O_7$, and $SrZrO_3$-rich materials which are considerably more resistive electrically.

MAFF Electrodes

Two of the three MAFF electrode sets were tested in the first proof test. In this test thermal conditions were more severe than the following two tests. Surface temperatures on MAFF electrodes were approximately 100°C over the predicted 1700°C. The combination of high temperatures and high level of carryover (Ca, Mg, La, Cr, Si) from upstream materials produced a zone (see Figure 59) near the surface with numerous reaction products and high porosity. Much of this region was probably liquid at test conditions. This zone also was depleted (80-90%) of Fe. The cooler regions on the sintered MAFF anodes were in fair shape (Figure 59a) with the presence of several cracks the major source of degradation. MAFF cathodes (Figure 59b) were subject to considerable attack by potassium. Dissolution by seed of MAFF grains could be seen at high magnification. Seed attack appears to proceed along grain boundaries with subsequent dissolution of surrounded grains. In the hotter portion of these electrodes, a recrystallized spinel containing K is observed. Evidence of a K, Fe-rich intergranular phase is also seen in the anodes. There was also severe potassium attack of spinel insulators. X-ray data provide evidence for breakdown of $MgAl_2O_4$ in the presence of iron and seed to produce MgO plus a (K, Fe, Al) phase--presumably an aluminate.

Finally, the cooler regions of the more porous plasma-sprayed cathodes displayed extensive zones having a reddish discoloration. X-ray diffraction shows the primary two phases in this region to be spinel (with lower Fe content than the original)

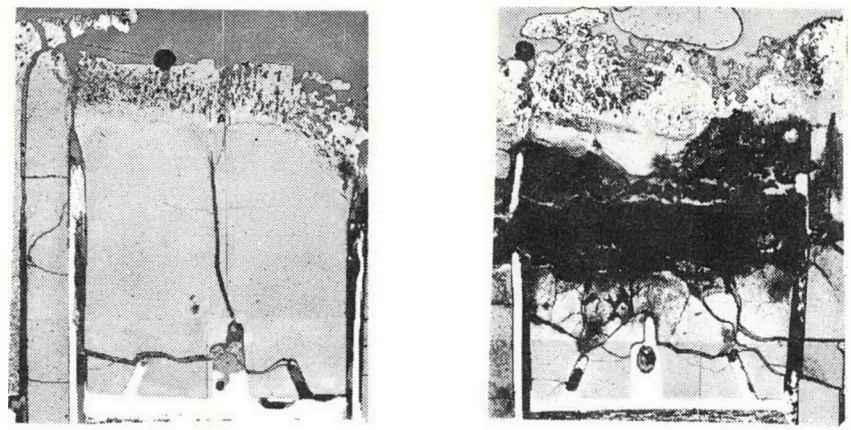

(A) (B)

Figure 59. Cross-Section of Sintered 4 $MgAl_2O_4$ · 1 Fe_3O_4 Electrodes After 20-Hour Proof Test; (A) Anode, (B) Cathode. (X2.5)

and Fe_2O_3. The presence of open porosity has allowed oxygen to react with the original spinel, oxidizing divalent iron to trivalent iron and forming Fe_2O_3. The chemical/electro-chemical phenomena associated with this reaction is discussed elsewhere (Reference 8).

HfO_2-Metal Electrodes (Argonne National Laboratories)

The microstructure, microchemistry and macro-scale phase distribution particularly for the HfO_2-Y_2O_3-CeO_2 materials varies considerably. This was done either intentionally or unintentionally during fabrication. Alumina is a significant contaminant for all of these materials. It, generally, resides within a groundmass containing other elements of the ceramic bulk composition. Within this matrix is coarser-grained ceramic. This contaminant may compromise the very refractory nature of HfO_2-based materials, contribute to a lowering of the electrical conductivity and provide reaction paths for seed. "Bloating" of these materials during electrical measurements above 1600°C could, in part, reflect formation of a fluid phase initiated by the presence of Al_2O_3. Original ceramic powders may include this contaminant or it might have been introduced during a "ball-milling" procedure prior to final fabrication.

HfO_2-based materials retain substantial anionic conductivity. Electrochemical reduction of the cathodic ceramic near and above the mesh was demonstrated. This does not appear to cause severe mechanical degradation in the short duration test. The melting temperature of the metal leadout and pertinent oxidation products, are particularly important for anode metal meshes combined with anion conductors. Oxidation of the metal is accelerated due to directed oxygen-electron transfer. Anodic oxidation/dissolution of metal could lead to formation of a resistive phase assemblage around the wires and loss of thermal/electrical contact. These ultimately would result in destruction of the anode. Evidence for these events, including melting, is suggested.

Summary - Recommendations

The material analysis of the nine electrode materials showed that three general modes of degradation can be identified: (1) the reworking or recrystallization

of a narrow (<2 mm) zone near the plasma surface, (2) reaction of molten seed in the temperature range, 900-1300°C, with the base electrode material--this includes active dissolution of grains by seed, and (3) in regions intermediate between (1) and (2) where potassium preferentially reacts with second phases or impurities (either present in the original material or picked up from upstream contamination). The reworking or recrystallization near the plasma surface is not necessarily a feature that could limit the durability of an electrode. The important fact may be that the microstructure, composition and properties of this zone may be quite different from the rest of the electrode. The other two modes of degradation are more likely to limit electrode life and performance. Both reactions are accelerated by the presence of impurities, second phases, porosity and cracks.

It appears that seed attack of $LaCrO_3$ based compositions more strongly correlated to the presence of open porosity (Table 13) and second phases than to variation in composition. For example, it can be argued that the $La_{.95}MgCrO_3$ cathodes were most resistant to seed attack because this material had the lowest porosity, was crack free and contained a minimum of second phases. As the complexity of the electrode chemistry and structures increased so did the occurrence of impurity phases, cracks, etc. So while more sophisticated electrode chemistries and structure may provide improved refractory properties, attention to microstructure, microchemistry and ceramic processing becomes more critical toward insuring adequate resistance to seed attack of cathodes. This is less true of anodes where seed concentrations are lower.

The selection of electrode materials for the Phase III U-02 test was made almost solely on a judgement of material durability--which had been defined as resistance to the three degradation modes discussed previously. On this basis, the $La_{.95}Mg_{.05}CrO_3/ZrO_2$ composite and the $LaCrO_3$-$LaAlO_3$ materials were judged as most resistant to the U-02 MHD environment. The electrical and thermal performance of electrodes constructed of these materials was acceptable. In preparation of the electrode blocks for the U-02 electrode walls, emphasis has been placed on further improvements in microchemistry and microstructure. Porosity levels were further reduced by hot pressing at higher temperatures, pressures and times. The porosity of the

$LaCrO_3/ZrO_2$ composite electrodes, for example, was reduced from 7% to 2%. Careful checks were made for micro-cracks.

One set of MgO doped lanthanum chromite electrodes was prepared from a stoichiometric (Mg+Cr/La = 1) powder with only 2% MgO. The conductivity of this composition is close to that of the 5% MgO, Cr_2O_3 rich (Mg+Cr/La = .9) $LaCrO_3$ used in the proof tests. The 2% MgO stoichiometric composition should minimize the occurrence of the $MgCr_2O_4$ second phase and Cr_2O_3 rich areas that appear to be susceptible to preferential seed attack. In a similar manner, the composition of the $LaCrO_3LaAlO_3$ electrodes was modified to a stoichiometric (Mg+Cr+Al/La) cation ratio and to contain only 2% MgO. This should minimize the formation of the Mg-Al(Cr) spinel second phase which was preferentially attacked by seed. In addition, the graded layers in this electrode will be each produced from a single homogeneous powder.

In addition, one set of $LaCrO_3/ZrO_2$ composite electrodes (cathodes only) will have low resistance platinum pins inserted high up in the cathode so that current can be drawn off above 1300°C. This reduces the voltage gradient in the 900-1300°C region where potassium compounds will condense and minimizes the effects of both the electrochemical reduction process as well as the accelerated diffusion of potassium ions and the damage caused thereby.

Again on the basis of material durability, both sintered dense MgO and $MgAl_2O_4$ were selected as interelectrode insulators for the U-02 test modules. The MgO is more refractory and subject to less reaction with electrodes near the plasma; as well as having better interelectrode insulation. The $MgAl_2O_4$, on the other hand, is less subject to thermal stress fracturing and has less serious reactions with liquid seed, i.e., formation of a potassium aluminate reaction product versus the active dissolution by seed.

5.2.3 U-02 Phase III Module

The U.S.-U.S.S.R. Cooperative Program on MHD provides the opportunity to evaluate the materials of construction and designs of refractory electrode systems through testing in the U-02 Facility under clean firing conditions. The third of these tests, U-02 Phase III, will be conducted in the U.S.S.R. U-02 Facility in May, 1978. Results of the prior Phase I and Phase II tests have been reported previously (References 10 and 11).

The objective of the U-02 Phase III Test is to evaluate the performance of refractory electrode systems during long term operation under MHD conditions. For this test emphasis is placed not only on electrode/insulator materials, but on current lead-out materials and attachments.

Desired operating conditons for the U-02 test are an electrode surface temperature $\geq 1700^{o}C$ and electrode heat fluxes of 16 to 20 W/cm^2. In contrast with the prior U-02 tests, the Phase III effort included a series of three proof tests conducted in the Westinghouse Electrode System Test Facility (WESTF). These tests, conducted over the period October 10, 1977 through January 6, 1978, provided the basis for the selection and design of materials for the Phase III module and were discussed in Section 5.2.2.

Each of the proof test channels contained 12 electrode pairs, compressively loaded in groups of 3, while the UO-2 Phase III channel will contain 36 electrode pairs, compressively loaded in groups of 6. With the exception of extensions in the copper cooling blocks for the U-02 module, electrode dimensions in the direction of plasma flow and perpendicular to the direction of plasma flow are essentially identical.

The electrode modules will be of the same overall physical size as those from previous U-02 tests, but there is a marked difference in design from the modules tested in Phase I and Phase II. The Phase I electrode walls were composed of 20 electrodes on 5 sub-modules and the Phase II electrode walls were composed of 30 electrodes on 6 sub-modules. Each sub-module had its own water-cooled copper

heat sink. For Phase III, each of the 36 electrodes on each wall be mounted on individually water-cooled copper heat sinks.

The following significant activities for the UO-2 Phase III module were completed during this quarter.

- Electrode materials selection
- Electrode thermal/structural design
- Detailed drawings preparation
- Electrode materials processing
- Module components and electrode sub-assemblies fabrication

Materials selection was discussed in Section 5.2.2.2 and materials processing development in Section 5.2.1.1. Design and fabrication activities will be described in the following sections.

5.2.3.1 U-02 Phase III Module Design

General System Design

The design of the U-02 Phase III Module started with a determination of the properties of the plasma in the Soviet U-02 facility. The fuel is natural gas containing by volume 97% methane, 2% ethane and 1% nitrogen. The oxidant is air with 1% moisture by weight and .318 moles of raw oxygen added per mole of air. A 50% by weight water-potassium carbonate solution is added until 1% by weight potassium exists in the combustion products.

Using the Westinghouse proprietary MHD-2502 computer program, the Mollier diagram for these combustion products is generated for a stoichiometric ratio $\Phi = 0.95$ and given in Figure 60. A general observation on the operation of the U-02 facility can be made from this diagram when the generator inlet operating conditions are given ($2600^{o}K$ plasma temperature, 0.8 atmosphere pressure and 0.75 kg/sec mass flow). The zero point on the enthalpy scale of Figure 60 represents the specific energy of combustion of room temperature reactants. The

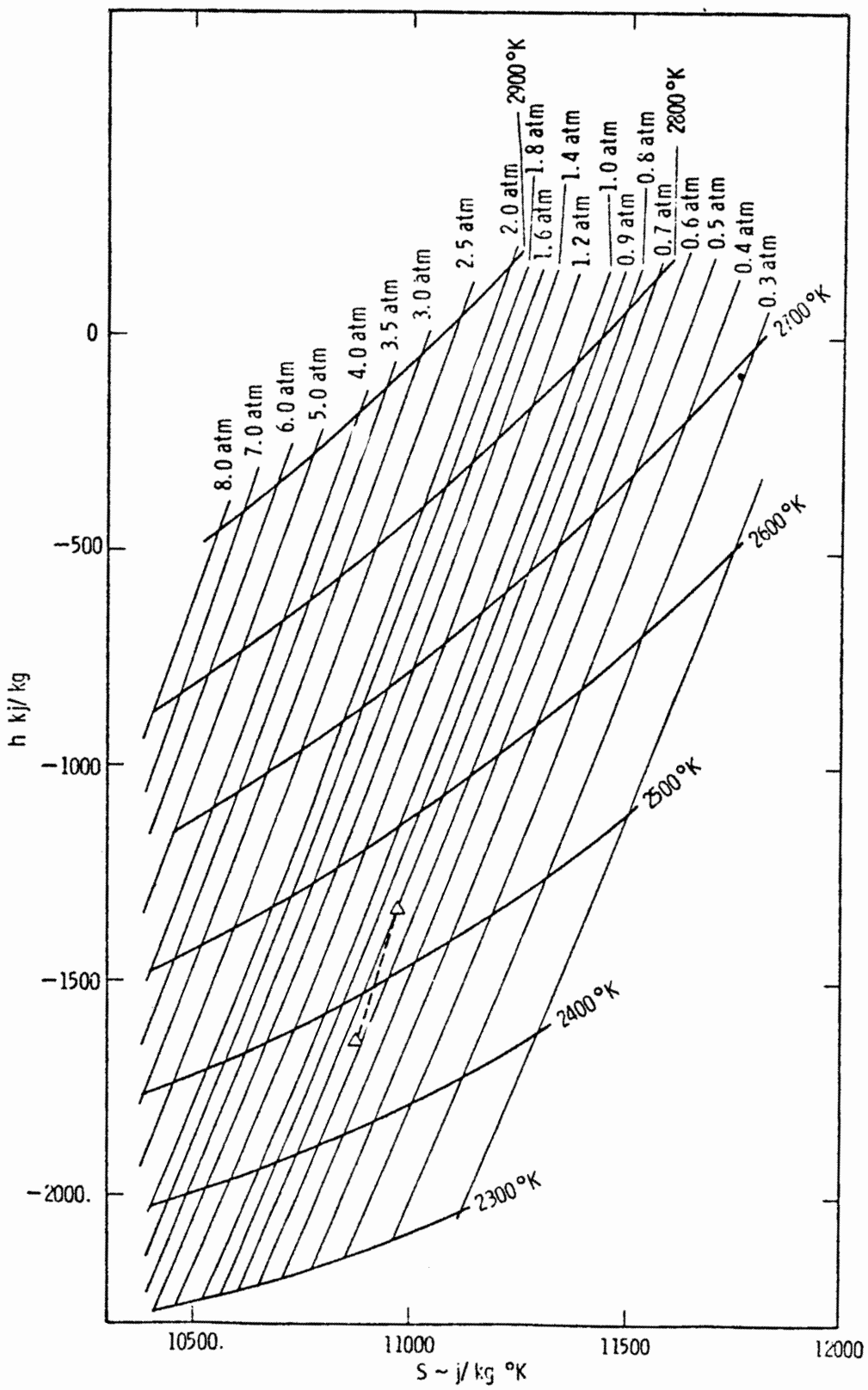

Figure 60. Mollier Diagram of Combustion Products of Natural Gas - Air and 0.318 Moles Raw Oxygen (Ø = 0.95) Showing Process Line for U-02 Generator

250°C air preheat adds about 150 kj/kg to these combustion products. The combustor and generator entrance heat loss is then about 1200 kj/kg or 900 kwatts but this has not been verified.

A constant velocity, Faraday generator duct is then designed by one-dimensional analysis at a loading parameter of 0.5, where all gas properties are interpolated from tables generated by the MHD-2502 computer program. Figure 61 shows the relationship between the various quantities affecting heat transfer in the duct where the wall temperature is specified to be 1850°C at the entrance and 1650°C at the exit. The total temperature of the plasma at the generator entrance is about 2535°K and drops about 23°K in the 0.5 meter long generator. A line reversal static temperature measurement at a location 18 cm upstream of the generator would indicate 2510°K. The predicted heat fluxes are in the 18-20 watt/cm^2 range. Theoretical values of heat transfer coefficient and heat flux for the six groups of electrodes in U-02 Phase III are shown in Figure 61. The process line for the entire 1.5m long test section is shown by the dashed line on the Mollier diagram of Figure 60, where a pressure drop of about 1.0 psia is predicted.

The theoretical electrical performance quantities of the generator are shown for an assumed load factor of 0.5 in Figure 62. A magnetic field of 1.75 tesla, axial velocity of 450 m/sec, and 26 cm distance across the channel predict an open circuit voltage of 200 volts. But, when the generator is loaded at the theoretically maximum power output load factor of 0.5, the cross channel voltage drops to 100 volts, the combustor floats to 260 volts above ground and 9.4 kw of electrical power is generated. Current densities of .26 - .29 amp/cm^2 are indicated.

The 1.0 cm wide electrode collects the current from the 1.36 cm pitch between electrodes giving an electrode current density of .35 - .39 amp/cm^2. Short circuit currents, can be estimated as twice the above values for a .70 - .78 amp/cm^2 maximum theoretical electrode current density, but this could never be achieved because structural and boundary layer loads prevent the short circuiting of the plasma.

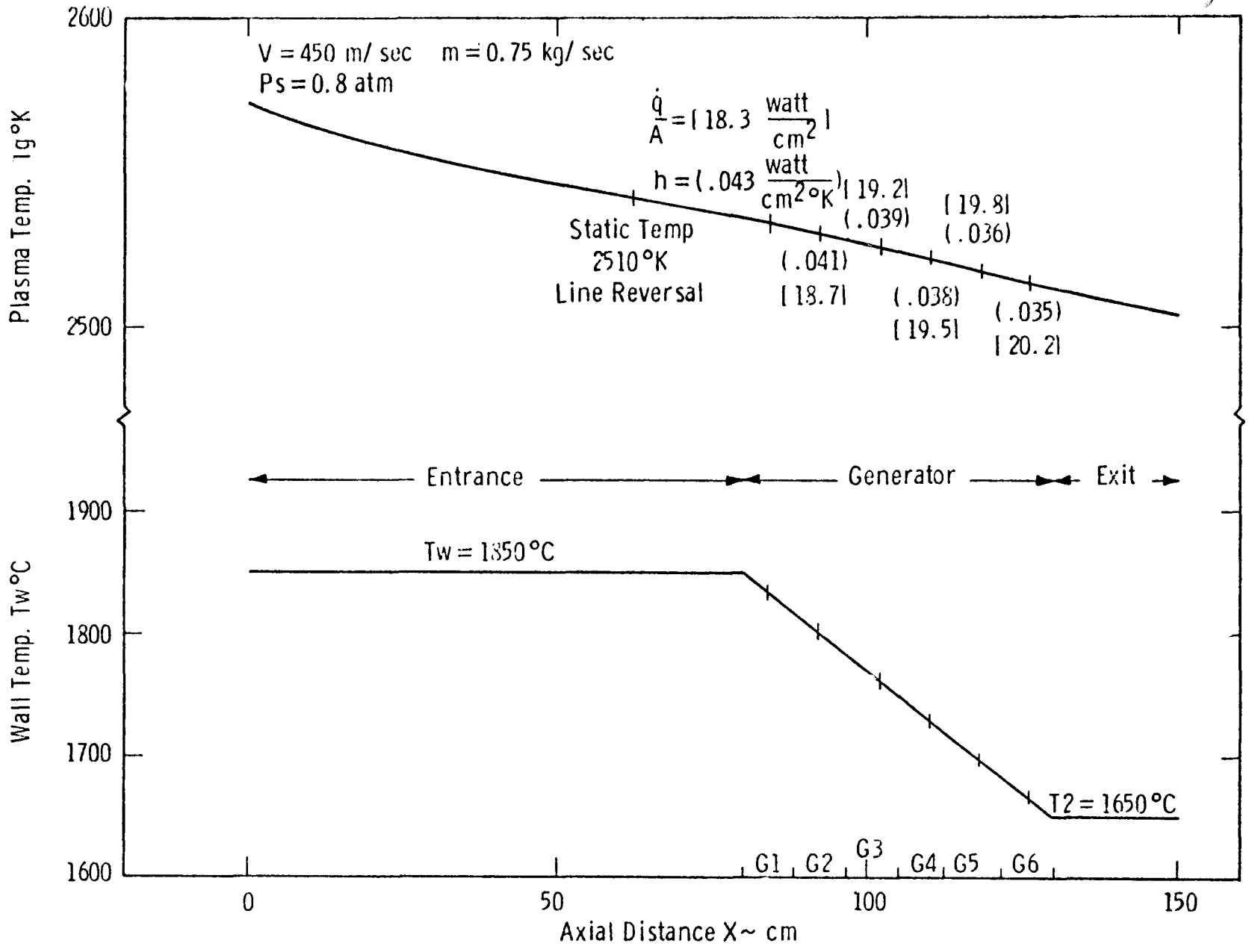

Figure 61. Theoretical Match Between the Various Quantities Affecting Heat Transfer in the U-02 Phase III Module

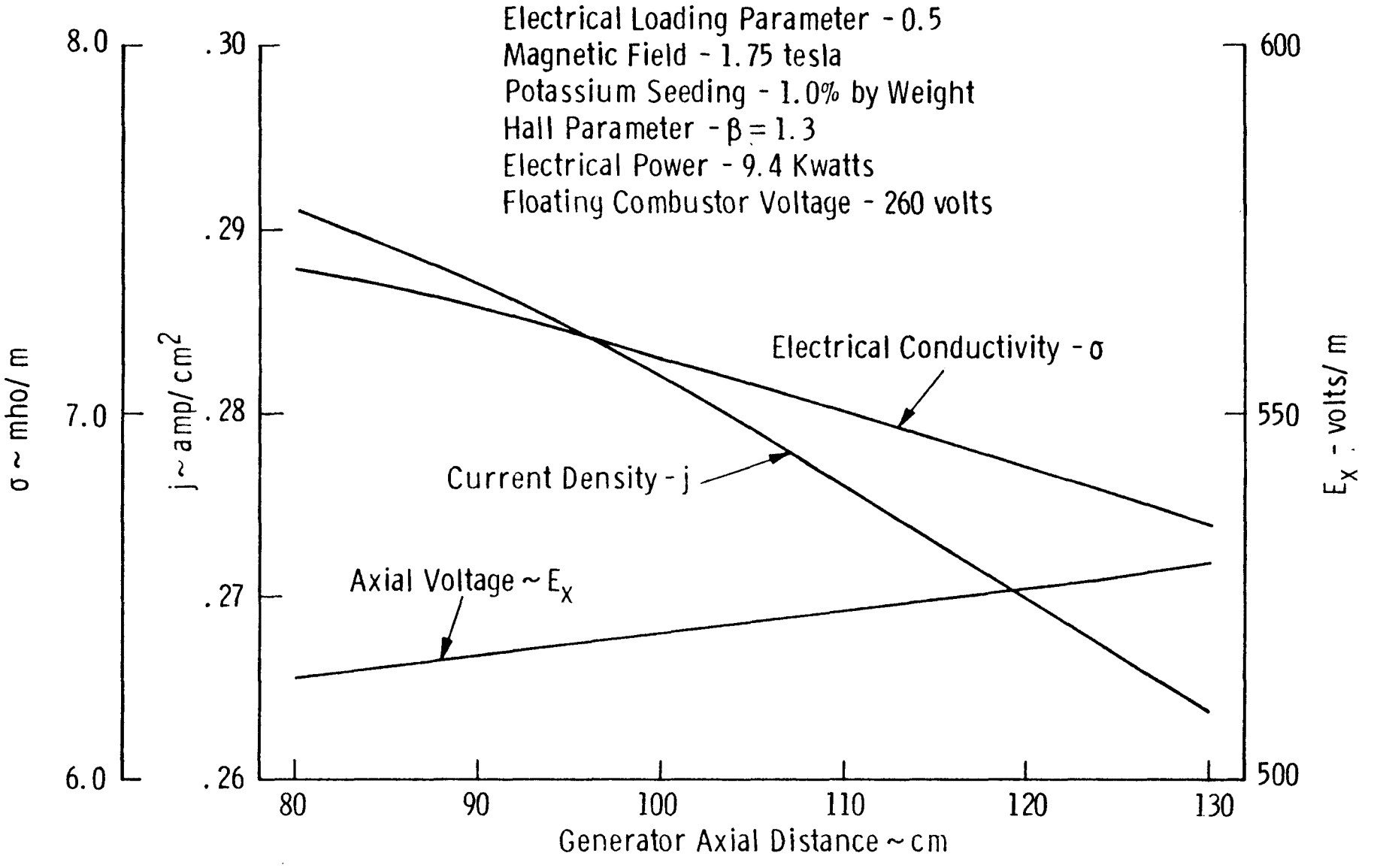

Figure 62. Theoretical Electrical Performance of U-02 Generator by One Dimensional Analysis

Electrode System Thermal Design

Thermal design analyses were completed to size the electrodes selected for the U-02 (Phase III) test facility such that specific surface temperature ranges and thermal gradients would be realized for each module group during nominal operation. These U-02 electrode design analyses also included the effect of Joule or resistive heating based upon a design current density of 1.25 A/cm^2 for fully "loaded" electrodes. These analyses, in general, are a continuation of the analyses reported in prior quarterly reports (References 1, 9).

Six electrode material groups will be assembled into the electrode walls as shown in Figure 63. These groups are also described in detail below.

1 - Ceramic electrode consisting of a uniform composition of 70% Lanthanum Chromite ($La_{0.95}\ Mg_{0.05}\ CrO_3$) with 30% Zirconia [(88) ZrO_2 - (12) Y_2O_3], a 0.2 in. thick nickel mesh compliant layer brazed to the ceramic electrode and to a copper heat sink with TiCuSil (68.8% Ag - 26.7% Cu - 4.5% Ti) and Nicrobraz 200 brazing filler metal, respectively, and a magnesium oxide (MgO) insulator.

2 - A graded ceramic electrode consisting of two equal length layers of Lanthanum Chromite with alumina, (graded from $La_{0.95}\ Mg_{0.05}\ Cr_{0.73}\ Al_{0.23}\ O_3$ to $La_{0.95}\ Mg_{0.05}\ Cr_{0.83}\ Al_{0.13}\ O_3$), a 0.2 inch thick nickel mesh compliant layer brazed to the ceramic electrodes and to a copper heat sink, and a magnesium oxide (MgO) insulator.

3 - A graded ceramic electrode consisting of four equal length layers of a uniform composition of 70% Lanthanum Chromite ($La_{0.95}\ Mg_{0.05}\ CrO_3$) with 30%, 20%, 10% and 0% Zirconia [(88) ZrO_2 - (12) Y_2O_3], a 0.1 inch thick nickel mesh compliant layer brazed to the ceramic electrode and to a copper heat sink, and a magnesium oxide (MgO) insulator.

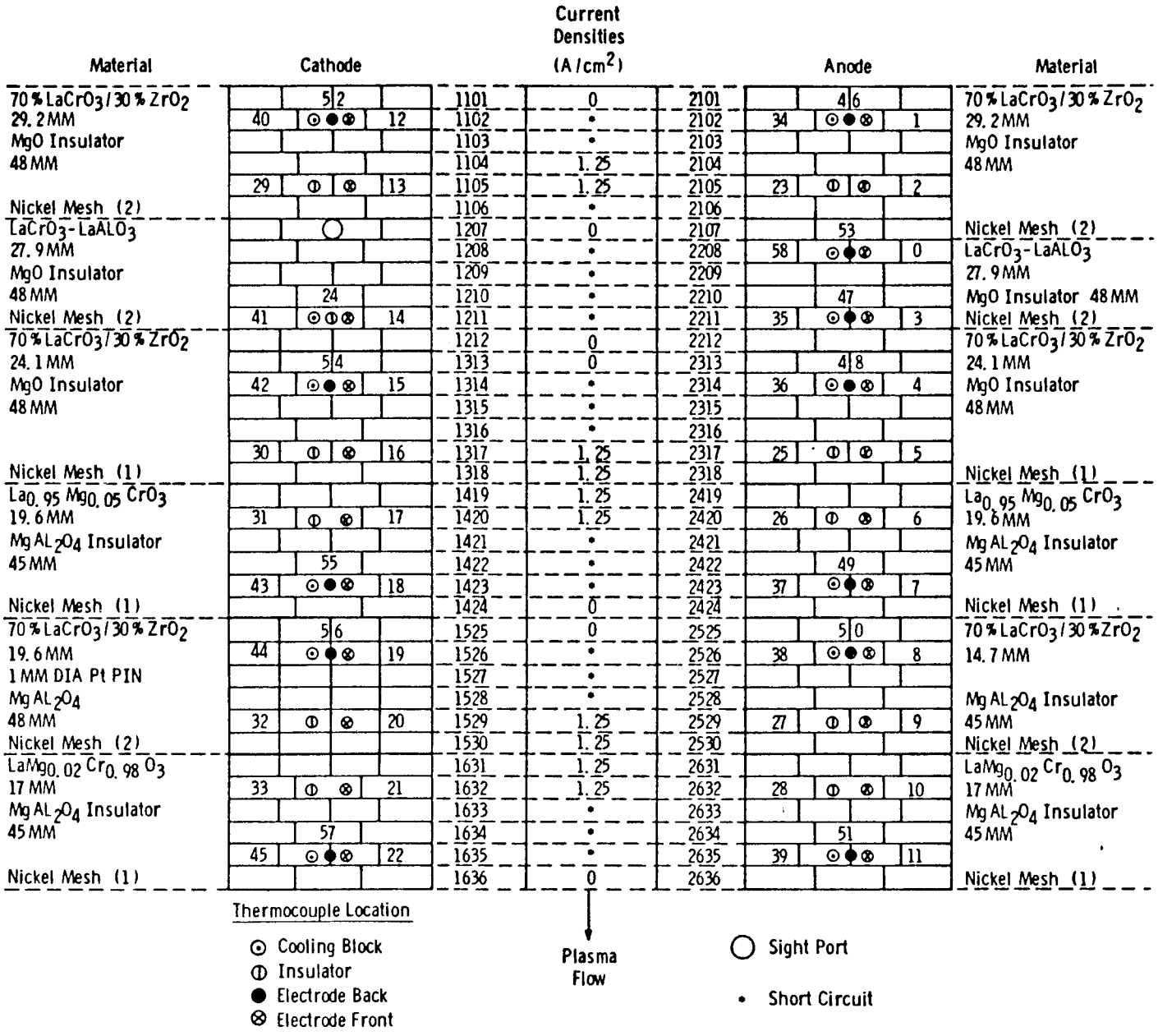

Figure 63. Phase III Electrode Wall Schematic

4 - A ceramic electrode of homogeneous Lanthanum Chromite containing 5 mole % magnesium, ($La_{0.95}Mg_{0.05}CrO_3$), a 0.1 inch thick nickel mesh compliant layer brazed to the ceramic electrode and to a copper heat sink, and a Spinel ($MgAl_2O_4$) insulator.

5a.- A ceramic electrode (anode) consisting of a uniform composition of 70% Lanthanum Chromite ($La_{0.95}\ Mg_{0.05}\ CrO_3$) with 30% Zirconia [(88) ZrO_2 - (12) Y_2O_3], a 0.2 inch thick nickel mesh compliant layer brazed to the ceramic electrode and to a copper heat sink, and a Spinel ($MgAl_2O_4$) insulator.

5b.- A ceramic electrode (cathode) consisting of a uniform composition of 70% Lanthanum Chromite ($La_{0.95}\ Mg_{0.05}\ CrO_3$) with 30% Zirconia [(88) ZrO_2 - (12) Y_2O_3], four thin Platinum pins (one inserted into each electrode segment), a 0.2 inch thick nickel mesh compliant layer brazed to the ceramic electrode and to a copper heat sink, and a Spinel ($MgAl_2O_4$) insulator.

6 - A ceramic electrode of homogeneous Lanthanum Chromite containing 2 mole % magnesium, ($La_{0.98}Mg_{0.02}CrO_3$), a 0.1 inch thick nickel mesh compliant layer brazed to the ceramic electrode and to a copper heat sink, and a Spinel ($MgAl_2O_4$) insulator.

The design electrode lengths and operating characteristics in order to ensure the thermal design requirements for all (as modeled) configurations in the U-02 Phase III are summarized in Table 14.

Additional Thermal Design Considerations

Plasma temperature (T_p) and film coefficient (h) profiles across the electrode (hot) face as summarized in Table 14 were based upon a heat balance model of the U-02 test facility. Consideration was given to temperatures (plasma) required to ensure sufficient conductivity to guarantee operation of nominally loaded electrodes at a current density of 1.25 A/cm^2. Additional design consideration for experimental film coefficients was based upon an analysis of

TABLE 14

MATERIAL/DESIGN CHARACTERISTICS FOR THE U-02 PHASE III MODULE[1]

ELECTRODE GROUP:	1	2	3	4	5a	5c	6
MATERIAL:	$LaCrO_3/ZrO_2$	$LaCrO_3/Al_2O_3$	$LaCrO_3/ZrO_2$	$LaCrO_3$	$LaCrO_3/ZrO_2$	$LaCrO_3/ZrO_2/Pt$	$LaCrO_3$
Insulator Material	MgO	MgO	MgO	$MgAl_2O_4$	$MgAl_2O_4$	$MgAl_2O_4$	$MgAl_2O_4$
Electrode Length (in.)	1.150	1.100	0.950	0.770	0.580	0.770	0.680
Insulator Length (in.)	1.364	2.314	2.057	1.877	1.744	1.984	1.777
Ni-Mesh Length (in.)	0.214	0.214	0.107	0.107	0.214	0.214	0.214
Cu Heat Sink Length (in.)	1.670	1.670	1.670	1.670	1.670	1.670	1.670
Electrode Width (in.)	0.393	0.393	0.393	0.393	0.393	0.393	0.393
Insulator Width (in.)	0.118	0.118	0.118	0.118	0.118	0.118	0.118
(At Design Point - Full Current)							
Electrode Surface Temp (°C)	1799	1790	1713	1685	1639	1711	1594
Insulator Surface Temp (°C)	1609	1711	1482	1500	1474	1555	1417
Electrode Surface Flux (W/cm^2)	17.3	17.0	19.3	18.0	18.7	16.8	19.3
Insulator Surface Flux (W/cm^2)	23.8	19.6	27.1	23.6	23.5	21.1	24.3
Interface Temp Ceramic-Mesh (°C)	251	393	254	288	500	449	302
Interface Temp Mesh-Copper (°C)	66	82	83	82	84	83	83
Steady-State Heat Flux (W/cm^2) (leaving Cu)	28.4	28.7	29.6	25.9	27.8	25.0	27.3
(At Design Point - No Current)							
Electrode Surface Temp (°C)	1757	1715	1689	1676	1614	1678	1586
Insulator Surface Temp (°C)	1530	1588	1444	1491	1451	1522	1409
Joule Heating Effect							
Electrode (°C)	42	75	25	10	25	~33	8
Insulator (°C)	78	21	38	8	24	33	8
Film Coefficient(BTU/HR - Ft^2 °F)							
Electrode Centerline	63.1	61.7	61.7	55.6	54.0	54.0	52.2
Electrode Top Edge	57.2	56.5	56.5	50.2	48.8	48.8	47.3
Plasma Temp (°C)							
Electrode Centerline	2343	2331	2326	2323	2318	2318	2314
Flectrode Top Edge	2268	2262	2256	2248	2244	2244	2240

[1]Data given for "as modeled," uninstrumented electrode/insulator materials.

Phase II data. The design film coefficient correlations used were selected to ensure that the general resistance of all electrode systems to high temperature conditions could be successfully achieved and evaluated.

Influence coefficients for plasma temperature (T_p), film coefficient (h), copper water temperature (T_w), attachment layer interface temperatures [electrode-nickel mesh (T_{e-nm}), nickel mesh-copper (T_{nm-cu})] thermal conductivity data (k) and their effect upon electrode surface temperature and electrode length were determined based upon sensitivity analyses using the three-dimensional computer code and compared to an independent determination based upon a one-dimension axial resistance model. There was found to be general agreement between the two methods in all regards.

Copper temperatures were based upon flow analyses considering a number of tube configurations, inserts, flow rates, and range of operating supply water temperatures and pressures. Several heat transfer correlations were examined in order to predict the maximum and minimum temperature gradient expected across drawn copper tubing as functions of the other parameters.

In order to achieve lower than predicted insulator surface temperatures at the electrode design point and still ensure compatible dimensions for module assembly two additional factors were considered. These were the influence of insulator length and the application of a thermal (silcone) grease to the interface between: 1) the insulator and the attachment material, 2) the insulator and the copper heat sink, and 3) both interfaces. It was found that the combination of thermal grease applied to both interfaces and a short insulator length would result in acceptably lower insulator surface temperatures at the design point. The applications of thermal (silicone) grease to any interface or combination thereof would not by itself contribute significantly to lowering of either the electrode surface or insulator surface temperature at design conditions (temperature), with or without current. Table 14 reflects the configurations chosen for electrode insulators in material groups 1-3, the groups for which this study was a consideration.

The optimum design characteristics selected for the platinum pin electrode (group 5 - cathode) in addition to those shown in Table 14 are given below. A number of parametric studies were conducted in order to establish the listed dimensions. Among these were:

1. Platinum pin surface temperature and electrode surface temperature versus pin length (in addition to hot surface locus) in an electrode ceramic of constant length.

2. Platinum pin surface temperature and electrode surface temperature versus effective contact length (platinum paste, zirconia cement versus counterbore for thermal expansion, etc.) in an electrode of constant length.

3. Platinum pin surface temperature and electrode surface temperature (constant length pin, constant surface locus, constant contact length) in an electrode ceramic of varying length.

4. Platinum pin surface temperature and electrode surface temperature (constant length pin, constant surface locus, constant contact length with ceramic) versus addition of thermal (silicone) grease surrounding the base of the pin in the attachment material and/or the copper heat sink.

5. Electrode ceramic surface temperatures immediately above platinum pin surfaces and associated temperature differences with neighboring ceramic in all above cases.

The design analyzed consisted of one plantinum pin centered in each of four 0.77" electrode segments. The pin was 0.040" in diameter, surrounded by 0.060" counterbore, 1.888" long and located 0.09625" below the electrode surface with an effective contact length of 0.09625". The values obtained gave nominal surface temperatures of 1711^{o}C, a temperature of the pin surface of 1300^{o}C for the middle two blocks and of 1287^{o}C for the end blocks. The surface temperature of the electrode immediately above the pin was depressed to 1627^{o}C for the middle two blocks and to 1597^{o}C for the end blocks.

Taper ratios for interelectrode gaps and for insulator-electrode gaps were determined for each group based upon best available and calculated thermal expansion coefficient data. Maximum taper ratios were established based upon general drawing tolerances and vendor material (machining tolerances) and upon expected service temperature ranges for each material group during the 100 hour test.

5.2.3.2 Electrode Sub-Assemblies Fabrication

An exploded view of the machined components of an electrode sub-assembly is shown in Figure 64. Although this sub-assembly consists of the 70% $La(Mg)CrO_3$/ 30%ZrO_2 electrode material in the upstream position, it is typical of the other sub-assemblies. For all groups, the maximum dimension from the base of the cooling block to the top surface of the ceramic is 2.564 inches.

The iniital step in the fabrication of the subassemblies consists of brazing the copper tubes and plug and the nickel mesh to a pre-numbered copper block. This is done in a single vacuum furnace brazing operation at about 1010°C (visual observation of melting of the braze alloy is employed) using 35 Au - 65 Cu braze alloy (solidus, 990°C, liquidus, 1010°C) for joining the tubes and plug to the block and Nicrobraz 200 (solidus, 975°C; liquidus, 1040°C) for joining the nickel mesh to copper. Following the brazing operation, the water passage is checked to ensure that it is vacuum tight. Then, the insulator pocket is machined in the block and the stress relieving slots are machined through the mesh and slightly into the copper block to line up with the spaces between the 3 or 4 ceramic electrode segments that will be brazed to each particular cooling block. After this, each block is subjected to a flow test and a hydrostatic pressure test where it must hold 160 psig for 5 minutes. Thereafter, any assembly found to exceed a .009 inch maximum overhang of the mesh on the edge opposite the insulator pocket is reworked to bring it into compliance, and then complete dimensional measurements are recorded for each block.

Fully machined and measured ceramic electrode blocks are matched to the copper/ mesh assemblies (note: ceramic blocks from Groups 1 and 6 are first sputtered

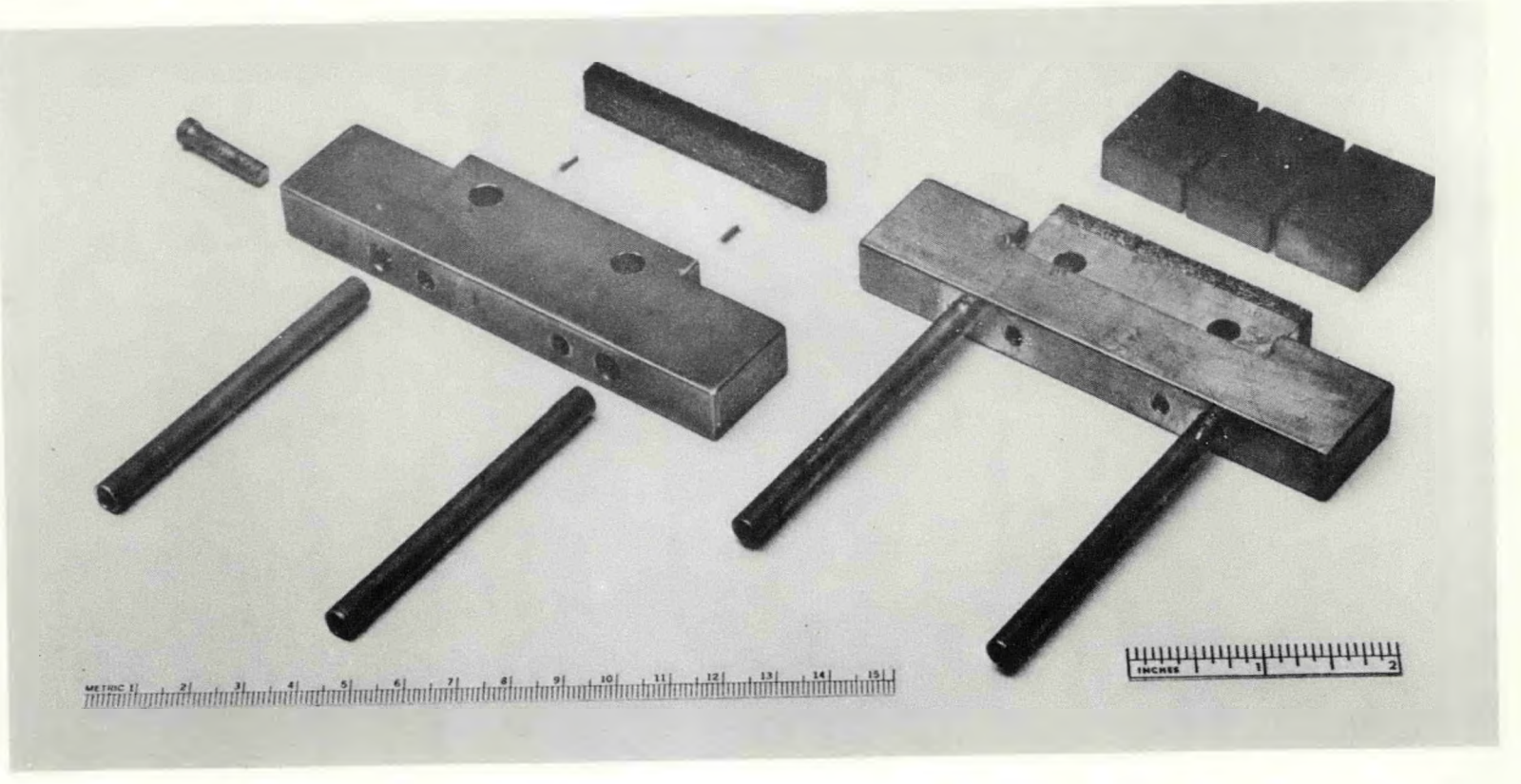

Figure 64. Exploded View of Typical U-02 Phase III Electrode Assembly

with a 500-1000 Angstrom gold film). These matched sets are then packaged and shipped to Brunswick Corporation, Technetics Division, DeLend, Florida where the brazing of the ceramic to the nickel mesh is accomplished using TiCuSil brazing foil (solidus, 830°C; liquidus, 850°C). The components are restrained in specially designed steel fixtures to maintain the required positioning of the ceramic segments with respect to each other and to the envelope dimensions of the copper base. Up to 20 assemblies are brazed at a time in a large vacuum brazing furnace under a pressure of 2000 microns of dry flowing argon. The furnace is heated until three strategically located thermocouples all read 820-840°C and held there until visual observation through a sight port verifies that the braze alloy has melted. After the parts are cool, they are removed, visually inspected, packed and returned to Westinghouse.

Upon receipt of the brazed electrode assemblies they are inspected by Quality Control and dimensional measurements are recorded. The side insulation, 10 mil thick G-10 laminate with 1 mil thick "Densil" transfer adhesive, is applied to most of the copper surfaces. Exceptions are the base that will be in contact with the G-10 supporting wall, the upper sides that will be covered by alumina plates, and the surfaces with thermocouple slots or counterbores that will receive the side insulation during final assembly onto the supporting wall. The ceramic interelectrode insulators will also be included during final assembly.

In addition to the normal set of electrodes, an alternate set of cathodes for Group 5 was prepared by drilling and counterboring the ceramic pieces to accept a .040 inch diameter platinum wire that terminates about .080 inch beneath the top surface of the electrode. The wire is joined to the ceramic over a length of about 1/4 inch with platinum paste fired at 1100°C. The wire passes through the long counterbore and extends beyond the base of the ceramic to fit into holes drilled through the mesh and into the copper block. Holes were drilled from the insulator pocket side to inersect with the holes drilled in the copper from the top. Silcoro 60 braze alloy (solidus, 835°C; liquidus, 845°C) was placed in the hole to join the platinum wire to the copper block during the TiCuSil brazing of the ceramic to the mesh. To ensure attachment, the

holes were also packed with a conductive epoxy before completing the assembly of this alternate electrode group.

As a part of the preparations for the final assembly of the electrode groups on the supporting wall, Type B and Type K thermocouples assemblies were prepared. First, the thermocouples were radiographed to locate the bead within the protective sheath. Then, ceramic and vinyl sleeving were placed over the sheath and, after applying an identifying number to the thermocouple connector, the thermocouple was bent near the tip to a pre-determined dimension. The bent thermocouple was then radiographed and the bead location referenced to the tip of the sheath and to the unbent sheath was measured and recorded. These measurements along with the Quality Control measurements of the distance of the thermocouple hole from the top surface of the electrode are required for thermal performance predictions.

6.0 WBS 1.6 - PROJECT MANAGEMENT AND DOCUMENTATION

The following project required documentation was issued during the reporting period.

- Express Report - Proof Test 3
- Monthly Project Management Summary Report - December
- Monthly Project Management Summary Report - January
- Monthly Project Management Summary Report - February
- Quarterly Report for the Period July 1 - September 30, 1977
- Quarterly Report for the Period October 1 - December 31, 1977
- U-02 Test Plan (Preliminary) Submitted to U.S.S.R.

In addition, the following papers were presented at the 17th Symposium on the Engineering Aspects of Magnetohydrodynamics, Stanford, California, March 1978.

- "Electrochemical Corrosion of MHD Electrodes in Slags," L. H. Cadoff, B. R. Rossing, and H. D. Smith, Westinghouse Research Laboratories, Pittsburgh, Pennsylvania.

- "Design and Operation of the Westinghouse Electrode Systems Test Facility (WESTF)," J. A. Dilmore, J. Lempert, S. J. Schneider, and E. W. Frantti, Westinghouse Research Laboratories, Pittsburgh, Pennsylvania.

- "Evaluation of Phase III U-02 Proof Test Materials," B. R. Rossing, L. H. Cadoff and J. A. Kuszyk, Westinghouse Electric Corporation, Pittsburgh, Pennsylvania; D. Marchant, and J. L.Bates, Battelle Northwest Laboratories, Richland, Washington; T. Negas, L. P. Cook, E. N. Farabaugh, W. Hosler, National Bureau of Standards, Washington, D. C.

- Design, Test and Evaluation of Refractory MHD Electrodes," J. W. Sadler, R. Calvo, G. E.Driesen, A.Eggers, E. L. Kochka, Westinghouse Advanced Energy Systems Division, Pittsburgh, Pennsylvania; and B. R. Rossing, Westinghouse Research Laboratories, Pittsburgh, Pennsylvania.

7.0 REFERENCES

1. FE-2248-18, "Development, Testing and Evaluation of MHD Materials and Component Designs, Quarterly Report, October - December, 1977," DOE Contract #EX-76-C-01-2248, Westinghouse Electric Corporation, March, 1978.

2. Koester, J. K., and R. M. Nelson, "Electrical Behavior of Slag Coatings in Coal-Fired MHD Generators," Proceedings of 16th Symposium on Engineering Aspects of MHD, Pittsburgh, PA, March, 1977.

3. FE-2248-15, "Development, Testing and Evaluation of MHD Materials and Component Designs, Quarterly Report, April - June, 1977," DOE Contract #EX-76-C-01-2248, Westinghouse Electric Corporation, July, 1977.

4. Heywood, J. B., and G. J. Womack, "Open Cycle MHD Power Generation," Pergamon Press, 1969, pp. 503-4.

5. Hara, T., and M. Uchida, Japanese Journal of Applied Physics, 7(2), February, 1968.

6. McWhirter, J. H., Applied Systems, Westinghouse R&D Center, private communication.

7. Jackson, W. D., et al., "Joint Test of a U. S. Electrode System in the USSR U-02 Test Facility," Proceedings of 15th Symposium on Engineering Aspects of MHD, Philadelphia, PA, May, 1976.

8. "Development, Testing and Evaluation of MHD Materials," Quarterly Report (to ERDA), National Bureau of Standards, March, 1977.

9. FE-2248-17, "Development, Testing and Evaluation of MHD Materials and Component Designs, Quarterly Report, July - September, 1977," DOE Contract #EX-76-C-01-2248, Westinghouse Electric Corporation, February, 1978.

10. Hosler, W., Ed., "Joint US-USSR Test of U. S. MHD Electrode Systems in USSR U-02 MHD Facility (Phase I)," Final Report, ERDA-76/154.

11. Rudins, G., et al., "The Second Joint Test of a U.S. Electrode System in the USSR U-02 Facility," Proceedings 16th Symposium on Engineering Aspects of MHD, University of Pittsburgh, May, 1977.

V. CONCLUSIONS

Further work on the electrochemical corrosion reactions of potential MHD materials in liquid slag has shown that iron in the slag strongly influences the corrosion mechanism of tested materials. Continued efforts to understand electrochemical corrosion mechanisms are essential to the selection of MHD electrodes operating under semi-hot wall slagging conditions.

A program is underway to assess the damage caused by arc erosion of cold wall anodes. A better understanding of the electrochemical/thermal phenomena associated with anode erosion will provide a basis for developing improved anodes for cold wall MHD application.

Completion of a series of three clean-fired, hot wall channel tests in WESTF and the evaluation of tested materials lead to the selection of hot-pressed $LaCrO_3$-based electrodes for the U-02 Phase III module to be tested in the Soviet Union in May, 1978. The selected attachment method employs an intermediate Ni-mesh compliant layer.

Additional development activities completed after the U-02 proof tests showed that reducing the voltage gradient across the cathode (by incorporating a low-resistance platinum pin in the electrode structure) slows the kinetics of potassium ion diffusion and minimizes the damage caused by electrochemical reduction processes at the cathode. One cathode group for the U-02 Phase III module was modified to include platinum pins within the electrode structure.

☆U.S. GOVERNMENT PRINTING OFFICE: 1979-640-092/441